

---

This item was submitted to [Loughborough's Research Repository](#) by the author.  
Items in Figshare are protected by copyright, with all rights reserved, unless otherwise indicated.

## Measurement and modelling of the influence of hysteresis on the internal temperature rise of rubber components

PLEASE CITE THE PUBLISHED VERSION

PUBLISHER

© Pongdhorn Sae-Oui

PUBLISHER STATEMENT

This work is made available according to the conditions of the Creative Commons Attribution-NonCommercial-NoDerivatives 2.5 Generic (CC BY-NC-ND 2.5) licence. Full details of this licence are available at:  
<http://creativecommons.org/licenses/by-nc-nd/2.5/>

LICENCE

CC BY-NC-ND 2.5

REPOSITORY RECORD

Sae-Oui, Pongdhorn. 2017. "Measurement and Modelling of the Influence of Hysteresis on the Internal Temperature Rise of Rubber Components". figshare. <https://hdl.handle.net/2134/27205>.

This item was submitted to Loughborough University as a PhD thesis by the author and is made available in the Institutional Repository (<https://dspace.lboro.ac.uk/>) under the following Creative Commons Licence conditions.



For the full text of this licence, please go to:  
<http://creativecommons.org/licenses/by-nc-nd/2.5/>

0401660516



BADMINTON PRESS  
UNIT 1 BROOK ST  
SYSTON  
LEICESTER, LE7 1GD  
ENGLAND  
TEL: 0116 260 2917  
FAX: 0116 269 6639





**MEASUREMENT AND MODELLING OF THE INFLUENCE OF  
HYSTERESIS ON THE INTERNAL TEMPERATURE RISE  
OF RUBBER COMPONENTS**

**by**


**PONGDHORN SAE-OUI**

**A doctoral thesis submitted in partial fulfilment of  
the requirements for the award of the degree of  
Doctor of Philosophy  
of Loughborough University**

**December 1997**

**Supervisor: Philip K. Freakley, Ph.D., FIM**

**Institute of Polymer Technology and  
Materials Engineering**

 <b>Loughborough University</b> Reference Library
Date <b>Sept 98</b>
Class
Acc No. <b>040186051</b>

K0631752

## ACKNOWLEDGEMENTS

This project could not have been completed without the help of many people. Foremost, I would like to express my profound gratitude to my supervisor, Dr. P.K. Freakley, and my advisor, Dr. P.S. Oubridge, for their extremely valuable suggestions throughout the duration of my work.

I would like to take this opportunity to thank Dunlop Metalastik Ltd. (Leicester, U.K) for supplying materials, rubber components and dynamic testing facilities necessary for the practical work. I am also grateful to J. Hallett, D. Newman and S. Crewe for their extremely useful assistance during my practical work.

I am especially thankful to the Thai Government for the financial support provided in order to pursue the work in this thesis.

Special thanks are also due to all RuPEC members, particularly Dr. D.W. Southwart, Dr. J. Clarke and B. Clarke, as well as my colleagues who have given me support and encouragement throughout my practical work. In addition, I also wish to thank Ahmad Yusof for his useful advice throughout the writing up period.

Finally, I am most appreciative of the encouragement and support of my parents, to whom this work is sincerely dedicated.

## ABSTRACT

Finite element analysis (FEA) is a numerical analysis method which is used widely to obtain approximate solutions in many fields of engineering. With sophisticated computer hardware and software, FEA has recently become an effective tool in the design of rubber components.

In this thesis, a study of the influence of hysteresis on the internal temperature rise of rubber components is presented. A method has been created in such a way that, by applying FEA, the internal temperature rise due to hysteretic effect can be predicted. In addition a study has been made to determine the effects of dynamic test conditions, such as strain amplitude and frequency, on the internal temperature rise of two types of rubber component: cylindrical anti-vibration mountings and a Chevron spring. An experimental design technique has been introduced to determine a mathematical relationship between the maximum temperature rise and the two test variables. Finally, an experimental evaluation of FE results has been made to check their accuracy.

Results have shown that FEA, combining stress and thermal analyses, is able to predict the internal temperature rise of the rubber components which are subjected to dynamic deformation under various test conditions. For both cylindrical anti-vibration mountings and a Chevron spring, it is found that the relationship between the maximum temperature rise ( $T_{max.}$ ) and the test variables (e.g., strain amplitude ( $\epsilon$ ) and frequency ( $f$ )) can be expressed mathematically by a single equation as given below.

$$T_{max.} = a_0 + a_1 \epsilon + a_2 f + a_3 \epsilon.f + a_4 \epsilon^2$$

where  $a_0$ ,  $a_1$ ,  $a_2$ ,  $a_3$  and  $a_4$  are equation coefficients. It is evident that the maximum temperature rise increases nonlinearly with the strain amplitude but increases linearly with frequency. Comparisons between the experimental and the computed results reveal that a good prediction of the internal temperature rise can be obtained from FEA, provided that both material data and the boundary conditions are specified accurately.

# CONTENTS

	Page No.
ACKNOWLEDGEMENTS. . . . .	i
CERTIFICATE OF ORIGINALITY . . . . .	ii
ABSTRACT. . . . .	iii
CONTENTS. . . . .	iv
LIST OF FIGURES. . . . .	viii
LIST OF TABLES . . . . .	xii
 <b>CHAPTER 1 : Introduction and Objectives . . . . .</b>	 <b>1</b>
1.1 Introduction . . . . .	1
1.2 Objectives . . . . .	2
<b>CHAPTER 2 : Literature review . . . . .</b>	<b>4</b>
2.1 Introduction to the Finite Element Analysis (FEA). . . . .	4
2.1.1 A brief history. . . . .	4
2.1.2 Basic concept of FEA . . . . .	5
2.1.3 Practical aspects of FEA . . . . .	5
2.1.3.1 Computer involvement in FEA . . . . .	6
2.1.3.2 Mesh development . . . . .	7
2.1.3.3 Element configurations . . . . .	8
2.1.3.4 Interpolation functions . . . . .	12
2.1.4 Solution Procedure of the FEA . . . . .	14
2.1.5 Errors in FEA . . . . .	16
2.2 Application of FEA in elastomer design . . . . .	17
2.2.1 Introduction to closed-form solution and FEA . . . . .	18
2.2.2 Characterisation of rubber elasticity. . . . .	20
2.2.3 Commercial software in elastomer design . . . . .	29
2.2.4 Experimental determination of elastic behaviour of rubber compounds. . . . .	30

2.2.5	A survey of published work in the application of FEA to rubber. . . . .	36
2.3	Dynamic properties of rubber . . . . .	40
2.3.1	Terminology of dynamic properties . . . . .	40
2.3.2	Factors controlling the dynamic properties . . . . .	43
2.3.3	Hysteresis and heat generation . . . . .	52
2.3.3.1	Molecular aspects of hysteresis . . . . .	52
2.3.3.2	Mathematical aspects of hysteresis . . . . .	54
2.3.3.3	Practical aspects of hysteresis and energy loss. . . . .	56
2.3.3.4	The effects of hysteresis and heat generation on elastomers. . . . .	59
2.3.3.5	Basic principles to minimise heat generation. . . . .	62
2.4	Thermal properties of rubber compounds . . . . .	63
2.4.1	Basic principle of heat transfer . . . . .	63
2.4.1.1	Conduction heat transfer . . . . .	64
2.4.1.2	Convection heat transfer . . . . .	65
2.4.1.3	Radiation heat transfer . . . . .	65
2.4.2	Thermal properties of rubber compounds. . . . .	66
2.4.2.1	Thermal conductivity . . . . .	66
2.4.2.2	Thermal diffusivity . . . . .	69
2.4.2.3	Heat transfer coefficient . . . . .	69
2.4.2.4	Emissivity. . . . .	71
<b>CHAPTER 3</b>	<b>: Project structure and Methodology . . . . .</b>	<b>72</b>
3.1	Introduction . . . . .	72
3.2	Project layout. . . . .	72
3.3	NISA II . . . . .	75
3.3.1	Introduction . . . . .	75
3.3.2	Pre- and post-processors . . . . .	76
3.3.3	Analysis types . . . . .	78
3.3.4	Material models . . . . .	80

3.3.5	Solution techniques for nonlinear analysis. . . . .	82
3.4	Characterisation of material constants via the theory of “constant true Young’s modulus with varying Poisson’s ratio”. .	85
3.4.1	General concept of the approach . . . . .	86
3.4.2	Conversion of true Young’s modulus into Rivlin material constants. . . . .	88
<b>CHAPTER 4</b>	<b>: Preliminary determinations of material data. . . . .</b>	<b>90</b>
4.1	Introduction . . . . .	90
4.2	Materials . . . . .	90
4.3	Curing test . . . . .	91
4.4	Determination of Rivlin Constants . . . . .	91
4.4.1	Introduction . . . . .	91
4.4.2	Methodology. . . . .	91
4.4.3	Results and discussion . . . . .	93
4.4.4	Conclusions . . . . .	97
4.5	Determination of hysteresis factor . . . . .	98
4.5.1	Introduction . . . . .	98
4.5.2	Methodology. . . . .	98
4.5.3	Results and discussion . . . . .	99
4.5.4	Conclusions . . . . .	102
4.6	Heat transfer coefficient analysis. . . . .	103
4.6.1	Introduction . . . . .	103
4.6.2	Methodology. . . . .	103
4.6.3	Results and discussion . . . . .	105
4.6.4	Conclusions . . . . .	111
<b>CHAPTER 5</b>	<b>: Modelling work. . . . .</b>	<b>112</b>
5.1	Introduction . . . . .	112
5.2	FEA of approximately cylindrical anti-vibration mountings. . . .	112
5.2.1	Mounting geometry . . . . .	112
5.2.2	Rubber compound . . . . .	113

5.2.3	Problem description and experimental design. . . . .	113
5.2.4	The FEA procedures . . . . .	114
5.2.4.1	Dynamic axial deformation . . . . .	115
5.2.4.2	Dynamic shear deformation. . . . .	121
5.2.5	Results and discussion . . . . .	127
5.2.5.1	Dynamic axial deformation . . . . .	127
5.2.5.2	Dynamic shear deformation. . . . .	142
5.2.6	Conclusions . . . . .	154
5.3	FEA of the Chevron spring . . . . .	155
5.3.1	Chevron geometry . . . . .	155
5.3.2	Rubber compound . . . . .	155
5.3.3	Problem description and experimental design. . . . .	155
5.3.4	The FEA procedures . . . . .	158
5.3.5	Results and discussion . . . . .	163
5.3.6	Conclusions . . . . .	167
<b>CHAPTER 6</b>	<b>: Evaluation of FEA results . . . . .</b>	<b>168</b>
6.1	Introduction . . . . .	168
6.2	Methodology . . . . .	168
6.3	Results and discussion . . . . .	172
6.3.1	Anti-vibration mountings . . . . .	172
6.3.2	Chevron spring . . . . .	180
6.4	Conclusions . . . . .	180
<b>CHAPTER 7</b>	<b>: Overall conclusion and further work . . . . .</b>	<b>182</b>
7.1	Overall conclusion. . . . .	182
7.2	Recommendations for further work . . . . .	183
<b>APPENDIX I</b>	<b>: Conversion of strain energy into heat generation rate . . .</b>	<b>185</b>
<b>REFERENCES</b>	<b>. . . . .</b>	<b>189</b>



## LIST OF FIGURES

	Page
Figure 2.1 Three stages in finite element software . . . . .	6
Figure 2.2 One-dimensional element . . . . .	9
Figure 2.3 Two-dimensional elements . . . . .	10
Figure 2.4 Some of the three-dimensional elements . . . . .	11
Figure 2.5 Pure homogeneous deformation diagram . . . . .	23
Figure 2.6 Mooney-Rivlin plot . . . . .	31
Figure 2.7 Sinusoidal stress-strain cycles . . . . .	41
Figure 2.8 Graphical relation between in-phase, out-of-phase and complex moduli . . . . .	42
Figure 2.9 Dynamic properties of unvulcanised NR over a wide frequency range at 25°C . . . . .	44
Figure 2.10 Comparisons of dynamic properties between unvulcanised, soft vulcanisate without filler and CB-filled vulcanisate. . . . .	45
Figure 2.11 Strain amplitude dependence of $G'$ for CB-filled IIR . . . . .	47
Figure 2.12 Strain amplitude dependence of phase angle of CB-filled butyl vulcanisates . . . . .	50
Figure 2.13 Strain amplitude dependence of loss modulus of CB-filled butyl vulcanisates . . . . .	51
Figure 2.14 Hysteresis loop in dynamic stress-strain cycles . . . . .	54
Figure 2.15 Temperature dependence of fatigue life of SBR and NR compounds . . . . .	60
Figure 2.16 Temperature dependence of critical tearing energy of filled NR and SBR vulcanisates . . . . .	61
Figure 2.17 Thermal conductivity of NR and SBR filled with various amount of CB . . . . .	68
Figure 3.1 Work plan for preliminary determinations of material data. . . . .	73
Figure 3.2 Schematic diagram of the entire FEA procedure . . . . .	74

Figure 3.3	Work plan for evaluation of FEA results . . . . .	75
Figure 3.4	Newton-Raphson methods. . . . .	84
Figure 3.5	Step-iteration or mixed method. . . . .	85
Figure 4.1	The test piece dimensions for the equilibrium stress-strain measurement. . . . .	92
Figure 4.2	Engineering stress against strain for “Metalastik 19055” . . . .	93
Figure 4.3	Engineering stress against strain for “Metalastik 32053” . . . .	94
Figure 4.4	True stress against strain for “Metalastik 19055” . . . . .	94
Figure 4.5	True stress against strain for “Metalastik 32053” . . . . .	95
Figure 4.6	The effect of temperature on true Young’s modulus . . . . .	95
Figure 4.7	The cross section view of the Dartec test specimen . . . . .	99
Figure 4.8	Hysteresis factor against strain amplitude of “Metalastik 19055”....	100
Figure 4.9	Hysteresis factor against strain amplitude of “Metalastik 32053”....	100
Figure 4.10	Hysteresis factor against temperature of the two Metalastik compounds . . . . .	101
Figure 4.11	Typical hysteresis curve of CB-filled rubber vulcanisate. . . . .	102
Figure 4.12	Geometry and FE model of a cylinder specimen for transient heat transfer analysis. . . . .	104
Figure 4.13	Temperature reduction traces of “Metalastik 19055” at position (5,10) . . . . .	106
Figure 4.14	Temperature reduction traces of “Metalastik 32053” at position (8,10.5). . . . .	106
Figure 4.15	Temperature reduction traces of steel at position (8,5) . . . . .	107
Figure 4.16	Temperature reduction traces of aluminium at position (9,15) . . . . .	107
Figure 4.17	Temperature reduction traces of “Metalastik 19055” at positions (0,2) and (6,0) . . . . .	108
Figure 4.18	Temperature reduction traces of “Metalastik 32053” at positions (1,12.5) and (5,6.5) . . . . .	109
Figure 4.19	Temperature reduction traces of steel at positions (0,3) and (6,10) . . . . .	109

Figure 4.20	Temperature reduction traces of aluminium at positions (0,11) and (6,5) . . . . .	110
Figure 5.1	Geometries of the anti-vibration mountings . . . . .	112
Figure 5.2	The experimental design for 2 factors . . . . .	114
Figure 5.3	2-D axisymmetric modelling of rubber mountings . . . . .	115
Figure 5.4	2-D FE meshes for stress analysis of rubber mountings . . . . .	116
Figure 5.5	2-D FE meshes for thermal analysis of rubber mountings . . . . .	118
Figure 5.6	3-D FE meshes for stress analysis of rubber mountings . . . . .	123
Figure 5.7	3-D FE meshes for thermal analysis of rubber mountings . . . . .	124
Figure 5.8	Equilibrium temperature distribution for the mountings subjected to dynamic axial deformation without precompression . . . . .	128
Figure 5.9	Equilibrium temperature distribution for the mountings subjected to dynamic axial deformation with 10% precompression . . . . .	129
Figure 5.10	The plots of the maximum temperature rise against the ratio of volume to surface area . . . . .	138
Figure 5.11	The effects of strain amplitude and frequency on the maximum temperature rise for the mountings subjected to dynamic axial deformation without precompression . . . . .	139
Figure 5.12	The effects of strain amplitude and frequency on the maximum temperature rise for the mountings subjected to dynamic axial deformation with 10% precompression . . . . .	140
Figure 5.13	Equilibrium temperature distribution for the mountings subjected to dynamic shear deformation without precompression . . . . .	143
Figure 5.14	Equilibrium temperature distribution for the mountings subjected to dynamic shear deformation with 10% precompression . . . . .	144
Figure 5.15	The plots of the maximum temperature rise against the ratio of volume to surface area. . . . .	150
Figure 5.16	The effects of strain amplitude and frequency on the maximum temperature rise for the mountings subjected to dynamic shear deformation without precompression . . . . .	151

Figure 5.17	The effects of strain amplitude and frequency on the maximum temperature rise for the mountings subjected to dynamic shear deformation with 10% precompression . . . . .	152
Figure 5.18	Chevron spring geometry . . . . .	156
Figure 5.19	Vee-shaped fitting of Chevron spring in axle-box . . . . .	157
Figure 5.20	Deformation characteristic of Chevron springs under vertical load.	157
Figure 5.21	Bottom view of Chevron spring with symmetry plane . . . . .	159
Figure 5.22	FE mesh of the Chevron spring for stress analysis . . . . .	160
Figure 5.23	FE mesh of the Chevron spring for thermal analysis . . . . .	162
Figure 5.24	Contour plot of equilibrium temperature distribution for the Chevron spring . . . . .	164
Figure 5.25	The effects of vertical deflection and frequency on the maximum temperature rise for the Chevron spring. . . . .	166
Figure 6.1	Cross section of the mountings representing the locations of thermocouple wire. . . . .	169
Figure 6.2	Testing machine for the anti-vibration mountings . . . . .	169
Figure 6.3	Testing machine for the Chevron spring. . . . .	170
Figure 6.4	Heat dissipation processes of rubber body placed firmly between two huge metal bars . . . . .	177

## LIST OF TABLES

	<b>Page</b>
Table 2.1    Some examples of interpolation function . . . . .	13
Table 2.2    Thermal conductivities of gum vulcanisates . . . . .	68
Table 2.3    Specific heat and density of rubbers and some mixing ingredients .	70
Table 2.4    Heat transfer coefficient for air flow parallel to flat surface. . . .	71
Table 4.1    The Mooney-Rivlin elastic constants . . . . .	96
Table 4.2    Material properties for thermal analysis . . . . .	105
Table 4.3    Heat transfer coefficients of materials. . . . .	108
Table 5.1    The experimental design set for mountings subjected to dynamic axial deformation without precompression. . . . .	120
Table 5.2    The experimental design set for mountings subjected to dynamic axial deformation with 10% precompression . . . . .	121
Table 5.3    The experimental design set for mountings subjected to dynamic shear deformation without precompression . . . . .	125
Table 5.4    The experimental design set for mountings subjected to dynamic shear deformation with 10% precompression. . . . .	126
Table 5.5    The maximum temperature rise and the maximum element strain energy density for mountings subjected to dynamic axial deformation. . . . .	133
Table 5.6    The estimated response equations for the mountings subjected to dynamic axial deformation. . . . .	134
Table 5.7    Approximate values of the geometric difference constant for dynamic axial deformation. . . . .	136
Table 5.8    Volume and surface area of the mountings. . . . .	137
Table 5.9    The maximum temperature rise and the maximum element strain energy density for the mountings subjected to dynamic shear deformation . . . . .	147
Table 5.10   The estimated response equations for the mountings subjected to dynamic shear deformation . . . . .	148

Table 5.11	Approximate values of the geometric difference constant for dynamic shear deformation. . . . .	149
Table 5.12	Test conditions for the Chevron spring . . . . .	158
Table 5.13	The maximum temperature rise for the Chevron spring subjected to 35 mm pre-vertical deflection. . . . .	165
Table 6.1	Test conditions and rubber compounds of the mountings . . . .	171
Table 6.2	Temperature results for the mountings subjected to dynamic axial deformation with 10% precompression . . . . .	172
Table 6.3	Temperature results for the mountings subjected to dynamic axial deformation without precompression. . . . .	173
Table 6.4	Temperature results for the mountings analysed with the modified values of heat transfer coefficient . . . . .	175
Table 6.5	The ratios of heat transfer rate per unit area by three different processes: conduction, free convection and radiation. . . . .	178
Table 6.6	The effect of variation in the value of thermal conductivity on the maximum temperature rise . . . . .	179

# CHAPTER 1

## INTRODUCTION AND OBJECTIVES

### 1.1 Introduction

Finite element analysis, or FEA for short, has become an effective tool in the design of engineering components. It is of great interest to many designers, particularly to rubber technologists, because it provides advantages over the cut-and-try process or the closed-form solutions. The use of FEA, coupled with sophisticated computer hardware and software, can reduce the time required to develop rubber parts by reducing the number of iterations. In addition, FEA now can handle the nonlinear behaviour of elastomers, thus giving more accurate results. As a consequence, FEA is becoming widely used for the design of rubber components for a variety of engineering applications, including components ranging from fluid seals and automobile engine mounts to multilayer elastomeric bearings for earthquake protection.

The mechanical behaviour of elastomers is characterised by using the constitutive theories (alternatively called material models) based on a strain energy density function. Numerous material models have been developed by many workers in order to account for both nonlinear behaviour and incompressibility of elastomers. The validity and efficiency of the newly developed models have been studied by comparing computed predictions with experimental data. Published work indicates that some of these models are valid only for infinitesimal strains, while some models can give good predictions over a wide range of deformations.

Recently, many FE software packages, such as ABAQUS, NISA II, and PATRAN, have provided a number of hyperelasticity models to predict the behaviour of practical rubber components. Since all such models are in terms of strain energy density function, which is purely concerned with elasticity, design of rubber components by FEA is therefore confined to only elastic behaviour. Unfortunately, it is well known that rubber

vulcanisates are viscoelastic in nature, so that the influences of creep, stress relaxation and hysteresis play an important role in component performance. However, FEA based on the strain energy density function is still an essential tool in rubber design, provided that great care is exercised.

For most applications, rubber components are subjected to dynamic stresses or deformations. It is widely known that one of the most important factors controlling the performance and the service life of the components is temperature. Basically, the practical concern of the temperature effect is that increasing temperature greatly accelerates the rate of oxidative reaction of rubber molecules, giving rise to higher crack growth rate and changes in rubber properties. Therefore, the performance and service life of rubber components are immensely dependent on the temperature. Since rubbers are not fully elastic, hysteresis generally has a great influence on the performance of rubber component because it brings about an internal temperature rise. This phenomenon is quite obvious and of particular importance in a rapid dynamic deformation as the temperature rise can be considerable and, of course, disastrous effect on the rubber component is inevitable. For this reason, it is a primary concern of this project to apply FEA to the prediction of internal temperature rise, due to the hysteretic effect, in rubber components (antivibration mountings and a Chevron spring) which are subjected to various service conditions. Specifically, the project is intended to provide guidance for engineers to determine suitable regions of service conditions if the temperature tolerance of the rubber compound is known.

## **1.2 Objectives**

- ◆ To determine some essential parameters governing the temperature rise of rubber compounds.



- ◆ To devise and evaluate a new method by which the internal temperature rise can be predicted.
- ◆ To study the effects of service conditions such as strain amplitude and frequency on internal temperature rise of two types of engineering component: antivibration mountings and a Chevron spring.
- ◆ To investigate the effects of both geometric factor and deformation mode on the internal temperature rise of antivibration mountings.

## **CHAPTER 2**

### **LITERATURE REVIEW**

#### **2.1 Introduction to Finite Element Analysis (FEA)**

##### **2.1.1 A brief history of Finite Element Theory**

Finite element analysis (FEA) is a numerical analysis technique for obtaining approximate solutions to a wide variety of engineering applications. It was originally developed for structural analysis. Although the label “finite element method” was first introduced in 1960, the idea of finite element analysis was created more than two thousand years ago by Greek mathematicians. It was started when many mathematicians were interested in determining the perimeter and area of a circle. Even though precise solutions had to wait for the advent of the calculus, in the meantime amazingly accurate results were found by using finite elements. A polygon was used to replace the circle in order to compute the perimeter. The straight line then becomes the finite element. This concept is considered as one dimensional line element modelling. In addition, triangles originating from the centre of the circle to the vertices of the polygon were used to calculate the area of the circle. This is actually a form of two-dimensional triangular element modelling. It is obvious that the use of finite element is feasible to approximate both circumference and area of the circle, hence, to estimate the value of  $\pi$ .

In antiquity, progress in the development of theory and the analytical techniques subsidiary to finite element analysis was very slow. In the early 1950's, the digital computer was first introduced as an aid to finite element analysis. Subsequently, the finite element method has developed simultaneously with the increasing availability of high-speed electronic digital computers, and a lot of computer specialists commenced to develop software for the method. Unquestionably, FEA is now a well-established technique and is widely used in a variety of fields of engineering.

### **2.1.2 The basic concept of FEA**

The basic principle of FEA is that a complicated problem can be divided into simpler subproblems, for which solutions can be achieved much more easily. Then the subproblem solutions are assembled to construct the ultimate solution of the original problem.

In general, a complex body is divided into simpler subdivisions, called “finite elements”, by using a discretization technique. These elements are interconnected at joints which are usually called “nodes” or “nodal points”. Simple functions are then chosen to approximate the field variable for each finite element. Such assumed functions are called “interpolation or basis functions” and are usually polynomials. Since the interpolation functions are expressed in terms of the values of the field variables at nodes, the problem now becomes how to evaluate the field values at nodes. However, in some cases, internal element points known as Gauss points are used in the solution process. The stresses are then extrapolated to the nodes, where they are averaged. Additionally, two important considerations should be taken into account.<sup>(1)</sup> Firstly, these interpolation functions must satisfy some continuity conditions across element boundaries. Secondly, certain boundary conditions must also be satisfied. There are several factors that affect the final solution, for instance: the types; the number and size of elements; the element distribution and grading; as well as the chosen interpolation function.

### **2.1.3 Practical aspects of FEA**

In the past, a high level of effort was required for the application of FEA. The method was considered as the tool for specialists, especially in solid and structural mechanics. Furthermore, the high cost of computers and their limited power, together with the limited capabilities of finite element programmes, were also the main shortcomings of FEA. In recent years, the developments of computer hardware and software have advanced rapidly, offering users a lot of auxiliary systems, such as graphics, windows,

macros, etc. Consequently, FEA has currently become the most powerful technique for structural engineering applications.

#### 2.1.3.1 Computer involvement in FEA

Engineering software has been progressing very rapidly, particularly in the use of graphic utilities. This progress is of great importance for the microcomputer environment. It is a fact that the finite element software is now much easier to learn and to use efficiently, compared to the past.

The primary principle of finite element software was reviewed by Nicholson and Nelson<sup>(2)</sup> as having three stages shown in Figure 2.1.

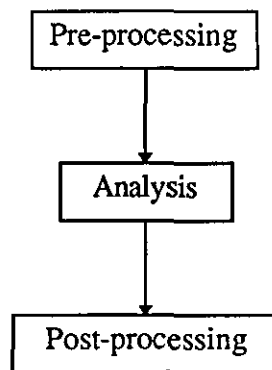


*Figure 2.1* Three stages in finite element software

At the pre-processing stage, the input file is developed, consisting of several sections as follows:

1. Control information (type of analysis, etc.);
2. Mesh :- element types, nodal co-ordinates and connectivities;
3. Material properties such as elastic modulus, etc.;
4. Applied loads, e.g., force or heat flux data;
5. Supports and constraints, e.g., prescribed displacements, etc.

Once the input data have been assembled with the assistance of the pre-processor, the analysis processor is then activated to solve the problem, resulting in a generation of raw

output data. Typically, the post-processor module consists of graphical utilities, offering the analyst a choice of output display, for example, colour contour plots, deformed shapes, graphs, etc. At this stage, two considerations should be taken into account: validation and interpretation. To validate the output, experimental data may be compared with the output data. If the output response is inconsistent with the experimental data, the input file and the mesh configuration should be modified.. With consistency, the analyst can be confident in the mesh and the proceeding step will be carried out. The problem of interpretation is frequently encountered when the output is massive. However, current graphical display systems are able to make interpretation much easier and more reliable. In addition, regions of high interest can be “zoomed in” by the application of the current post-processors.

#### 2.1.3.2. Mesh development

Generally, the basic philosophy of FEA is known as going from part to whole. Therefore, the subdivision or discretization process is essentially the first step in the solution process. After the discretization is complete, the domain body will be in the form of a network of finite elements. This network or collection of elements is called the finite element mesh. As already stated, there are two important factors that affect the solution obtained from FEA. One is the choice of finite elements and another one is the choice of interpolation functions. The selection of these factors is strongly dependent not only on the engineering judgement, but also on the required accuracy and the availability of a high performance computer and, hence, the cost.

In the past, manual mesh generation required considerable labour for complicated applications. Fortunately, automatic mesh generation has now been introduced and is used in conjunction with graphical displays.

As the accuracy of FEA is greatly dependent upon selection of the number and location of finite element nodes and element types, several practical rules should be considered.<sup>(2)</sup>

1. Nodes should be located where concentrated loads or heat fluxes are applied.
2. Nodes should be located where displacements and temperatures are constrained or prescribed.
3. Nodes should be located along lines and surface patches over which pressures, shear stresses, distributed heat fluxes, and surface convection are present.
4. Nodes should be located at boundary points where the applied tractions and heat fluxes experience discontinuities.
5. Nodes should be located along lines of symmetry.
6. Nodes should be located along interfaces between different materials or components.
7. Element aspect ratios (defined as ratio of largest to smallest element dimensions) should not be greater than five.
8. Symmetric configurations should have symmetric meshes.
9. The density of elements should be greater in domains with high stress or temperature gradients.
10. Element density variations should be gradual rather than abrupt.
11. Meshes should be uniform in domains with low gradients.
12. Element orientations should be staggered to prevent bias.

#### 2.1.3.3 Element configurations

In the discretization process, the number, shape, size and configuration of the elements must be particularly modelled in such a way that the actual structure is simulated as closely as possible. This process is based on individual engineering judgement. It should be realised that the original structure must be subdivided into sufficiently small elements so that the adequately accurate solution can be obtained. However, it should also be borne in mind that a finer subdivision will require more computational effort.

As the computed solution depends heavily on the geometry of the element, the number and location of nodes and the node types, the configuration (or shape) of the basic element to be used are important issues in the application of FEA. Generally, a finite

element comprises a simple one-, two-, or three-dimensional configuration. Detailed information of these element configurations is given below.

#### ◆ One-dimensional elements

In general cases, line elements are used as the representation of one-dimensional elements as shown in Figure 2.2. From the figure, it can be seen that the straight line ends at nodal points numbered 1 and 2 which are called external nodes because they represent interconnecting points to neighbouring elements. The additional nodal points may be required (e.g., nodes 3, 4, ...) in some applications. Since these nodes are intermediate and not connected to any other elements, they are called internal nodes. The location of nodes is on the line segments. The number and type of nodes can be selected to suit the interpolation functions. The one-dimensional element is generally used for simple structures that can be modelled by line drawing, such as trusses and frames.

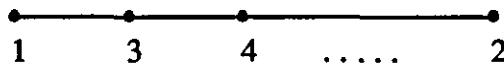
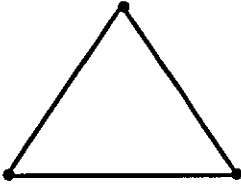


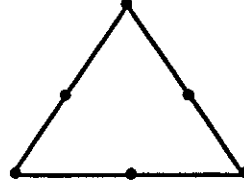
*Figure 2.2* One-dimensional element

#### ◆ Two-dimensional elements

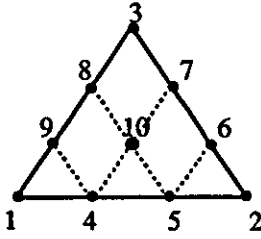
Linear triangle elements are basically used as the representation of two-dimensional problems. The 3-node linear triangle is the simplest element for this case. More complicated and advanced triangles are also applicable, for instance, the quadratic triangles, the cubic and quartic triangles. Other common types of two-dimensional elements are the rectangular and quadrilateral shapes. The former can also be considered as the specific type of the latter. Although, practically, any two-dimensional problem can be represented by an assemblage of triangular elements, there are certain problems in which quadrilateral elements are advantageous.



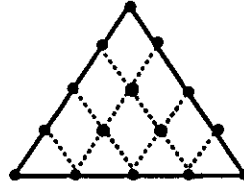
(a) 3-node linear triangle



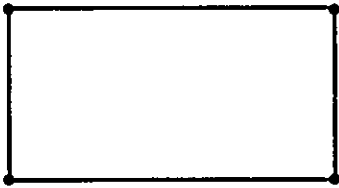
(b) 6-node quadratic triangle



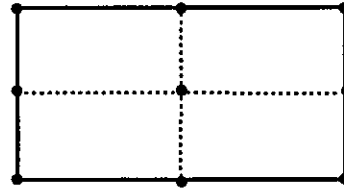
(c) 10-node cubic triangle



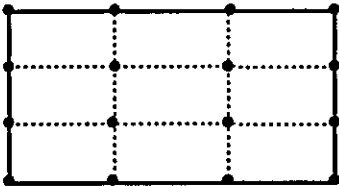
(d) 15-node quartic triangle



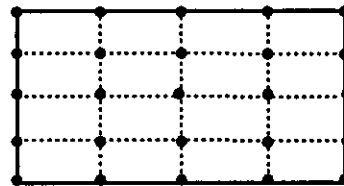
(e) 4-node linear rectangle



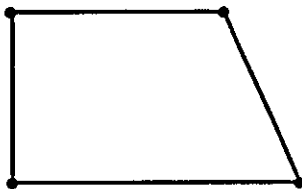
(f) 9-node quadratic rectangle



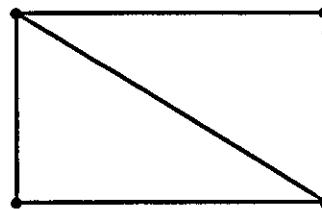
(g) 16-node cubic rectangle



(h) 25-node quartic rectangle



(i) Quadrilateral element



(j) Quadrilateral formed by 2 triangles

**Figure 2.3** Two-dimensional elements



In some cases, instead of using quadrilateral elements directly, it is possible to subdivide the domain into triangular elements without any difficulty, as a lot of modern pre-processors are advanced enough to do so.

All the two-dimensional elements previously mentioned are shown in Figure 2.3. As can be seen, unlike one-dimensional elements, there are two possible types of external nodes for two-dimensional elements. For example, the corner nodes indicated by 1, 2 and 3 in Figure 2.3(c) are called primary external nodes. When additional nodes appear on the element faces, like nodes 4, 5, 6, etc., they are referred as secondary external nodes. The internal nodes such as node 10 is also applicable in two-dimensional elements.

◆ Three-dimensional elements

Corresponding to the triangles, tetrahedron elements are frequently used in the three-dimensional problems. A tetrahedron contains four primary external nodes. Other forms of three-dimensional elements are also possible, i.e., a general hexahedron or a rectangular prism, which is classified as special case of the hexahedron.

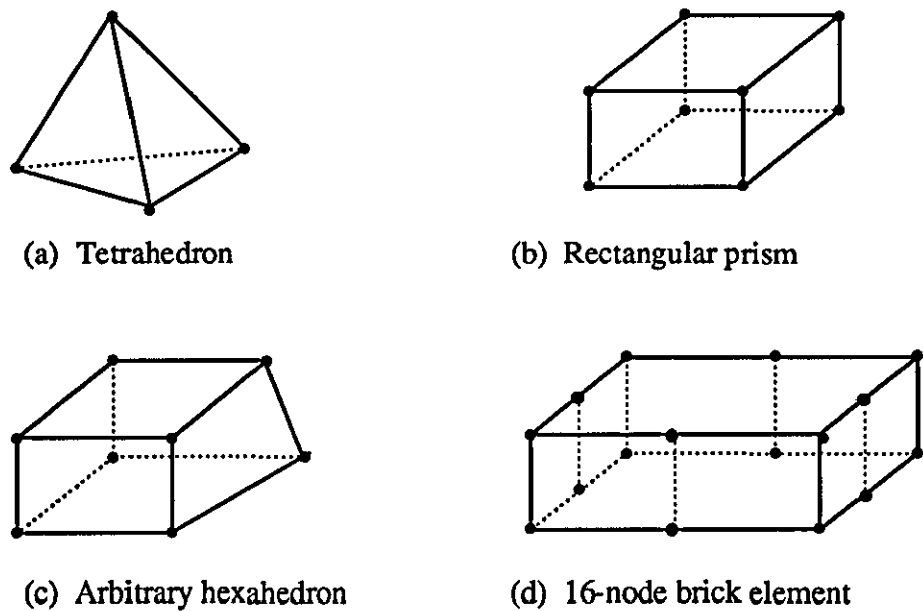


Figure 2.4 Some of the three-dimensional elements

Similar to the two-dimensional elements, secondary external nodes or internal nodes can be introduced for each of these elements. It should be noted that a hexahedron can be constructed from several tetrahedra. Some of the three-dimensional elements are shown in Figure 2.4.

In the case of problems which cannot be represented by an accumulation of only one element type, two or more types of elements are necessary for such problems. These are generally known as “mixed assemblages”.<sup>(3)</sup>

#### 2.1.3.4 Interpolation functions

A solution of complicated problems can be approximated by subdividing the region of interest into finite elements and representing the solution within each element by a relatively simple function, namely an interpolation function. As a consequence, the selection of interpolation functions is fairly important in FEA. This function expresses the field variable, which is defined as the principal unknown of a problem such as displacement, temperature, etc., within the chosen element in terms of their values at nodes. The interpolation function is the assumed function which approximates the distribution of the field variable over a finite element and it can be conveniently represented by a polynomial expression. Other functions, for instance, trigonometric, etc., are less frequently used. There are several reasons why the polynomials are used so extensively. Firstly, the use of polynomial provides the possibility to differentiate and integrate with relative ease. Secondly, it is easy to handle the mathematics of polynomials in formulating the appropriate equations for a variety of elements and in performing digital computation. Finally, it is easy to control the required accuracy by increasing its degree (or its order). A polynomial of arbitrary order gives a final solution closely to the true solution. It is also obvious that a polynomial of infinite order corresponds to an exact solution. However, practically, it is always limited to one of finite order. The higher the order of polynomial used in the approximation, the more closely the exact solution is represented.

The general terms of the  $n^{\text{th}}$  order polynomial for one-, two- and three-dimension can be expressed as shown in the Equations (2.1), (2.2) and (2.3) respectively. Examples of interpolation function derived from these equations are represented in Table 2.1. The coefficients of the polynomial, the  $a$ 's, are known as generalised co-ordinates. All the equations are normally converted into the element matrix forms which are convenient for computational process.

$$P_n(x) = \sum_{i=0}^n a_i x^i \text{----- (2.1)}$$

$$P_n(x,y) = \sum_{k=1}^m a_k x^i y^j, \text{ } i+j \leq n \text{ and } m = \frac{(n+1)(n+2)}{2} \text{----- (2.2)}$$

$$P_n(x,y,z) = \sum_{l=1}^m a_l x^i y^j z^k, \text{ } i+j+k \leq n \text{ and } m = \frac{(n+1)(n+2)(n+3)}{6} \text{----- (2.3)}$$

Table 2.1 Some examples of interpolation function

Dimension	Expression	Behaviour
One-	$P_0(x) = a_0$	constant
	$P_1(x) = a_0 + a_1x$	linear
	$P_2(x) = a_0 + a_1x + a_2x^2$	quadratic
Two-	$P_0(x,y) = a_1$	constant
	$P_1(x,y) = a_1 + a_2x + a_3y$	linear
	$P_2(x,y) = a_1 + a_2x + a_3y + a_4xy + a_5x^2 + a_6y^2$	quadratic
Three-	$P_0(x,y,z) = a_1$	constant
	$P_1(x,y,z) = a_1 + a_2x + a_3y + a_4z$	linear
	$P_2(x,y,z) = a_1 + a_2x + a_3y + a_4z + a_5xy + a_6xz + a_7yz + a_8x^2 + a_9y^2 + a_{10}z^2$	quadratic

Of particular importance are isoparametric elements, in which the geometry and the field variable are represented by the same interpolation function.

### **2.1.4 Solution procedures of FEA**

A primary strategy of the finite element solution can be briefly summarised step-by-step as follows.

#### **1. Discretization of the continuum.**

The first step is to divide the continuum or the main body into suitable finite elements, whose nodes must be specified. A variety of element types may be used. Indeed, the number and the type of elements in a given problem are essentially based on engineering judgement.

#### **2. Selection of the interpolation functions.**

After the elements and nodes have been specified, the next step is to choose the interpolation function to represent the variation of the field variable over the element. Usually, polynomials are selected as interpolation functions for the field variable. With isoparametric elements, the degree of the polynomial chosen depends upon the number of nodes assigned to the element, the number of unknowns at each node and certain continuity requirements imposed at the nodes and along the element boundaries.

#### **3. Derivation of the element properties.**

Once the elements and their interpolation functions have been chosen, the matrix equations expressing the properties of the individual elements must be determined by using one of the following approaches.

3.1. The direct approach which is generally used in relatively simple problems. It is derived from the direct stiffness method of structural analysis.

3.2. The variational approach which can be used for both simple and more complicated problems. This approach relies on the calculus of variations and involves extremizing a functional. For problems in solid mechanics, the functional variable turns out to be the potential energy and, therefore, this approach is then based on the principle of minimum potential energy. The variational approach is now applicable to a wide variety of engineering problems.

3.3. The weighted residuals approach which is more versatile and advantageous because it is possible to extend the finite element method to problems where no functional variable is available. The weighted residuals approach begins with the governing equations of the problem and proceeds without relying on a variational statement. This approach is used extensively to determine the element properties for nonstructural applications such as heat transfer and fluid mechanics.

4. Assembly of the element properties to obtain the system equations.

This process includes the assembly of all element properties to estimate the properties of the overall system. In other words, matrix equations expressing the behaviour of the elements must be combined to form the matrix equations expressing the behaviour of the entire system. In general, the basis for the assembly method is that the value of the field variable at a node where elements are interconnected must be the same for all elements sharing that node.

5. Application of boundary conditions.

Before the system equations can be solved, they must be modified to account for the boundary conditions of the problems. The boundary conditions imposed on nodes or elements are the known values of the dependent variables such as displacements or nodal loads, etc.

## **6. Solutions of the system equations.**

After the assembly process, the assembled system equations are solved to obtain the unknown nodal values of the field variable of the problem. In linear equilibrium problems, the solution techniques for solving these equations are straight forward. However, for nonlinear problems, the different solution techniques are applied in such a way that the desired solutions are obtained by a sequence of steps. More detailed description of the solution techniques for nonlinear problems is given later in Section 3.3.5.

## **7. Additional computations.**

Sometimes, after the solutions of the system equations are obtained, additional computation is required to calculate other important parameters such as stresses, strains, element strain energies, etc. Finally, some post-processing functions are performed to display or plot the results.

Since the aim of this thesis is to illustrate the applications of FEA in the rubber field, the mathematical procedures are beyond the scope of this project. However, there are many references which give more detailed information if required.<sup>(3-8)</sup>

### **2.1.5 Errors in FEA**

In spite of providing a highly accurate solution, there are two main classes of errors arising in FEA. These are:

### **1) Modelling error.**

This source of error results from insufficiently accurate input data such as the material properties and boundary conditions. Moreover, there often are compromises in the mesh, for example, modelling sharp corners as rounded.

### **2) Numerical error.**

This source of error arises from not only the subdivision of the main body into discrete parts, but also the round off of the computer computation. The finite element represents a continuous system with a discrete system, at some loss of accuracy. Practically, the significance of discrete error is often assessed by comparing solutions from two meshes, the second of which is a refinement of the first. Round off errors ensue from the limitations in arithmetic operation of computer and may play an important role in a very large system (with a large number of nodes).

## **2.2 Application of finite element analysis in elastomer design**

The application of finite element analysis is of great interest to many rubber technologists. The rapid progress and greater availability of related computer hardware and software, particularly computer-aided design (CAD) systems, has resulted in FEA becoming more and more important in the design of rubber components. The use of FEA provides the potential of designing and analysing problems much more efficiently and rapidly than trial-and-error processes.

Generally, the major finite element application to rubber design is to determine the rubber component geometry to give required force-deformation behaviour. If the designed components do not meet the defined requirements, for instance, if the development of excessive stress is found, the product can be redesigned and reanalysed.

Nevertheless, several difficulties arise with the application of FEA to rubber components. These are as follows:<sup>(2)</sup>

- rubber is nearly incompressible, developing high stresses in regions of confinement;
- rubber undergoes large strains so that geometric nonlinearity becomes important and must be taken into account during the analysis;
- rubber is normally bonded to much stiffer component such as metal plates;
- rubber components are often small and thin;
- failures normally take place at interfaces between rubber and stiffer components;
- rubber material properties, represented in the form of a strain energy density function, are difficult to characterised experimentally.

Because of such difficulties, great care is needed to achieve good analytical results. In recent years, a number of sophisticated software programmes have been developed with enhanced capabilities of designing and analysing rubber components, for example, ABAQUS, PATRAN and NISA II.

### **2.2.1 Introduction to closed-form solution and FEA**

Finite element analysis has obviously become an important tool in the design of elastomeric components because it now can handle the nonlinear characteristics of elastomers together with complex geometries of the components, thus increasing the design accuracy, while cutting the design time.

In the past, design of elastomeric components depended largely on a cut-and-try process. Most designers were reluctant to use the finite element analysis due to two main misapprehensions.<sup>(9,10)</sup> The first one is that FEA is a time consuming process and requires excessive computational effort, particularly when applied to the nonlinear elastomers. The second one is that the application of simple closed-form handbook formulae to the design of complicated components is more cost effective than FEA. From the second



misapprehension, it is considered that FEA is not a means for developing conceptual design, but preferable to refine a concept if the cost can be justified.

As a consequence of these misapprehensions, closed-form analytical solutions and handbook equations have been used extensively to reduce some of the cut-and-try iterations which are inherent to the design of simple elastic components. These techniques, however, are of limited use in designing the complex geometries frequently found in real design problems. To derive the equations, one important assumption is usually made, that is the rubber stress-strain response is linear. This assumption, however, does not exist in most situations because nonlinearity is found in many cases when the rubber component is strained beyond 10%. In addition, most models neglect other important properties such as the effects of material hysteresis and time dependent behaviour (creep and stress relaxation). Closed-form solutions are sometimes based on an intelligent guess. In many cases, therefore, a “fudge factor” based on experience must be added to the equation in order to take care of any unknown deviation between actual response and predictions. Some published work<sup>(9,10)</sup> concluded that the accuracy of closed-form solutions is limited to simple component geometries and relatively small deformations. When real-life complexity is introduced, their accuracy, and hence usefulness, collapses.

Fortunately, an alternative technique, which is more powerful than the closed-form solutions, has been introduced and used extensively in the design of elastic components, namely finite element analysis. The basic philosophy behind the finite element analysis is previously described in Section 2.1. In addition to providing acceptable accuracy, FEA provides superior benefits, compared to the closed-form solutions, as illustrated belows.<sup>(9,10)</sup>

- FEA can be used to analyse the dynamic behaviour of rubber components through the use of hysteresis data.

- FEA can reduce the time required to develop rubber parts by cutting the number of iterations required to achieve the final product.
- FEA can handle the nonlinear behaviour of rubber while the closed-form solutions cannot.
- FEA can be used to estimate normal strain distributions along the interface between rubber and rigid components, which is not available with most closed-form solutions.

### **2.2.2 Characterisation of rubber mechanical behaviour**

The most remarkable behaviour of rubber is that it exhibits elastic response up to large strains. This kind of behaviour is generally known as “hyperelasticity” and can be described in terms of the “elastic potential function” or a “strain energy density” which is defined as the strain energy stored in the material per unit of volume in the initial configuration as a function of strain at that point in the material. The hyperelastic constitutive relations based on the strain energy density have been widely used to represent the rubber-like materials, especially in the field of rubber engineering. However, it should be borne in mind that the hyperelastic behaviour represents the elastic characteristics of complete reversibility of the deformation as well as the assumption that the response is independent of the deformation history.

Numerous mathematical constitutive theories based on strain energy density functions have been developed for nonlinear, large elastic deformation of rubber materials. These theories, associated with the finite element analysis and computer-aided design, are very effective in design and analysis of elastic components operating in highly deformed states.

A number of theories can now accommodate nonlinear elastic behaviour. These theories can be roughly classified into two main categories.<sup>(11)</sup> The first category assumes that the strain energy density function ( $W$ ) is a polynomial function of the principal strain

invariants (I). The Rivlin model, for incompressible material, is the simplest example of this. If only the first order terms are used, the model is commonly known as the Mooney-Rivlin material model. The second category assumes that the strain energy density can be expressed by separated functions of the three principal extension ratios ( $\lambda$ ). Ogden<sup>(12)</sup>, Peng<sup>(13)</sup> and Peng-Landel<sup>(14)</sup> material models are all in this category.

It should be noted again at this point that the mechanical properties of rubber possess both elastic (reversible) and hysteresis (irreversible) effects but the strain energy density function is confined to only elastic effects and cannot involve hysteresis effect.<sup>(15)</sup> Unfortunately, some compounding ingredients such as carbon black, etc., are usually added to elastomers to modify their properties to suit an engineering application. The incorporation of these ingredients tends to increase the hysteresis effects (energy loss or heat generation) during deformation. However, this does not make the application of the strain energy density function useless, but it requires extra effort and great care in collection of experimental data and in the use and interpretation of FEA predictions.

In this section, the basic principles of the widely known nonlinear elastic constitutive theories, which are used directly with the finite element analysis, are reviewed briefly. Nevertheless, it should be realised that the constitutive functions described here are just samples of those used to represent the elastic strain energy density of various elastomers. Practically, the choice is usually governed by their availability in an FE programme, coupled with the relevance to the material and application.

- Neo-Hookean and Mooney-Rivlin material models

According to Rivlin's theory<sup>(16)</sup>, the elastic properties of a rubber can be represented in terms of a strain energy density function with particular regard to the strain invariants  $I_1$ ,  $I_2$  and  $I_3$ . The mathematical correlation can be approximated by the power series;

$$W = \sum_{i+j+k=1}^{\infty} C_{ijk} (I_1 - 3)^i (I_2 - 3)^j (I_3 - 1)^k \quad \text{----- (2.4)}$$

where  $W$  is the strain energy density, the stored strain energy per unit volume. Subscripted  $C$ 's are the material constants.  $I_1$ ,  $I_2$  and  $I_3$  are the three strain invariants, given in terms of the principal extension ratio  $\lambda_1$ ,  $\lambda_2$  and  $\lambda_3$  by

$$I_1 = \lambda_1^2 + \lambda_2^2 + \lambda_3^2 \quad \text{----- (2.5)}$$

$$I_2 = \lambda_1^2 \lambda_2^2 + \lambda_2^2 \lambda_3^2 + \lambda_3^2 \lambda_1^2 \quad \text{----- (2.6)}$$

$$I_3 = \lambda_1^2 \lambda_2^2 \lambda_3^2 \quad \text{----- (2.7)}$$

An extension ratio ( $\lambda$ ) is comparable to a strain but is defined as the ratio of a deformed dimension to the original (undeformed) dimension.

By considering the pure homogeneous deformation of a unit cube of rubber (Figure 2.5), correlations between the true stresses (the ratio of force to the deformed cross-sectional area) and the strain energy density have been proposed as:

$$t_1 = \frac{2}{\lambda_1 \lambda_2 \lambda_3} \left\{ \lambda_1^2 \frac{\partial W}{\partial I_1} + \lambda_1^2 (\lambda_2^2 + \lambda_3^2) \frac{\partial W}{\partial I_2} + \lambda_1^2 \lambda_2^2 \lambda_3^2 \frac{\partial W}{\partial I_3} \right\} \quad \text{----- (2.8)}$$

$$t_2 = \frac{2}{\lambda_1 \lambda_2 \lambda_3} \left\{ \lambda_2^2 \frac{\partial W}{\partial I_1} + \lambda_2^2 (\lambda_3^2 + \lambda_1^2) \frac{\partial W}{\partial I_2} + \lambda_1^2 \lambda_2^2 \lambda_3^2 \frac{\partial W}{\partial I_3} \right\} \quad \text{----- (2.9)}$$

$$t_3 = \frac{2}{\lambda_1 \lambda_2 \lambda_3} \left\{ \lambda_3^2 \frac{\partial W}{\partial I_1} + \lambda_3^2 (\lambda_1^2 + \lambda_2^2) \frac{\partial W}{\partial I_2} + \lambda_1^2 \lambda_2^2 \lambda_3^2 \frac{\partial W}{\partial I_3} \right\} \quad \text{----- (2.10)}$$

where  $t_1$ ,  $t_2$  and  $t_3$  are the true stresses in three principal directions.

For incompressible material,  $I_3 = 1$  and Equation (2.4) reduces to

$$W = \sum_{i+j=1}^{\infty} C_{ij} (I_1 - 3)^i (I_2 - 3)^j \quad \text{----- (2.11)}$$

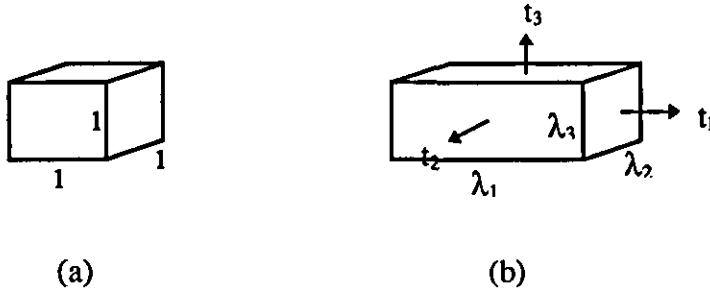


Figure 2.5 Pure homogeneous deformation diagram: (a) undeformed state and (b) deformed state

The power series in Equation (2.4) is usually truncated by expressing only the leading terms, yielding the simplest constitutive equation for strain energy density function, the so called Neo-Hookean or Gaussian law. This can be expressed as;

$$W = C_{10} (I_1 - 3) \quad \text{----- (2.12)}$$

where  $C_{10}$  is the material constant and  $I_1$  is the principle invariant. However, this model has a limited accuracy and is not reliable for general structure problems. So, terms containing  $I_1$  and  $I_2$  have to be added by taking the first two terms of Equation (2.4), namely the Mooney-Rivlin material model. The strain energy density function based on the Mooney-Rivlin model is the most extensively used in stress analysis of elastomeric components. It was proposed by Mooney<sup>(17)</sup> based on a linear correlation between stress and strain in simple shear.

For incompressible materials, the strain energy density function depends only on  $I_1$  and  $I_2$  (where  $I_3 = 1$ ) and it can be mathematically expressed as;

$$W = C_{10} (I_1 - 3) + C_{01} (I_2 - 3) \quad \text{----- (2.13)}$$

where  $I_1$  and  $I_2$  are the principal invariants of the strain and  $C_{10}$  and  $C_{01}$  are the Mooney-Rivlin material constants. For a uniaxial extension where  $\lambda_2 = \lambda_3$ , the stress-strain equation for an incompressible Mooney-Rivlin material can be expressed as;

$$\sigma = 2 (\lambda_1 - \lambda_1^{-2}) (C_{10} + C_{01} \lambda_1^{-1}) \quad \text{----- (2.14)}$$

where  $\sigma$  is an engineering stress (ratio of force to undeformed cross-sectional area) and the extension ratios are defined by

$$\lambda_2 = \lambda_3 = \frac{1}{\lambda_1^2} \quad \text{----- (2.15)}$$

$$\text{Then, } I_1 = \lambda_1^2 + \frac{2}{\lambda_1} \quad \text{----- (2.16)}$$

$$I_2 = 2\lambda_1 + \frac{1}{\lambda_1^2} \quad \text{----- (2.17)}$$

In both cases of incompressible and compressible forms, the initial shear modulus ( $G$ ) is associated with the material constants by the following equation;

$$G = 2 (C_{10} + C_{01}) \quad \text{----- (2.18)}$$

For incompressible material, the initial Young's modulus ( $E$ ) can be represented by

$$E = 3G = 6 (C_{10} + C_{01}) \quad \text{----- (2.19)}$$

but for compressible material,  $E$  is represented as;

$$E = \frac{9KG}{(3K + G)} \quad \text{----- (2.20)}$$

where  $K$  is the initial bulk modulus.

In general, both  $C_{10}$  and  $C_{01}$  can be approximately checked when the initial value of  $G$  is known. Nevertheless, Medri<sup>(18)</sup> pointed out that this model is usually not accurate over large ranges of strains and should be used only for qualitative analyses. Furthermore, Tschogel<sup>(19)</sup> proposed that the shortcomings of the Mooney-Rivlin equation to characterise the behaviour of real rubbers arise from not taking enough terms in truncating Equation (2.4).

- Morman and Pan material model

Similar to the Mooney-Rivlin material model, a five parameter model has been introduced by Morman and Pan<sup>(10)</sup> for incompressible hyperelastic materials. This model

overcomes the disadvantage of the Mooney-Rivlin material model by containing higher order terms, widely known as third-order deformation approximations. The expression of this model is

$$W = C_{10} (I_1 - 3) + C_{01} (I_2 - 3) + C_{11} (I_1 - 3) (I_2 - 3) + C_{20} (I_1 - 3)^2 + C_{30} (I_1 - 3)^3 \quad \text{----- (2.21)}$$

where all the five constants ( $C_{10}$ ,  $C_{01}$ ,  $C_{11}$ ,  $C_{20}$  and  $C_{30}$ ) are characteristic parameters of the material which can be numerically determined from uniaxial and multiaxial stress relaxation data.<sup>(20)</sup>

- Gent and Thomas material model

This model has been proposed by Gent and Thomas.<sup>(21)</sup> According to this model, the strain energy density function is expressed in the form;

$$W = C_1 (I_1 - 3) + C_2 \ln (I_2/3) \quad \text{----- (2.22)}$$

$$\text{where } I_1 = \lambda_1^2 + \lambda_2^2 + (\lambda_1 \lambda_2)^2 \quad \text{----- (2.23)}$$

$$I_2 = \lambda_1^{-2} + \lambda_2^{-2} + (\lambda_1 \lambda_2)^2 \quad \text{----- (2.24)}$$

They also pointed out that this form has significant advantage over the two term Mooney-Rivlin form, particularly in representing uniaxial compression behaviour (equivalent to equibiaxial tension).

- Cubic strain energy density function model

A newly developed form of the strain energy density has been proposed by Yeoh.<sup>(22,23)</sup>

This model presumes that  $\frac{\partial W}{\partial I_2}$  is extremely small compared to  $\frac{\partial W}{\partial I_1}$ , so that it can be

neglected without any serious error. By equating  $\frac{\partial W}{\partial I_2}$  to zero, the leading terms of

Rivlin's strain energy density function then become;

$$W = C_{10} (I_1 - 3) + C_{20} (I_1 - 3)^2 + C_{30} (I_1 - 3)^3 \quad \text{----- (2.25)}$$

As can be seen, the strain energy density is now a cubic function of  $(I_1 - 3)$ . A comparison with experimental data showed that this model is capable of predicting multiaxial data with high accuracy.

- Ogden material model

Ogden<sup>(12,24)</sup> proposed a separability of the dependence of the strain energy function on the principal extension ratios ( $\lambda_1$ ,  $\lambda_2$  and  $\lambda_3$ ) with particular reference to the Valanis-Landel hypothesis<sup>(25)</sup>, as expressed in the form;

$$W = W(\lambda_1) + W(\lambda_2) + W(\lambda_3) \quad \text{----- (2.26)}$$

For incompressible materials, the strain energy density function can be expressed as;

$$W = \sum_{i=1}^3 \sum_{j=1}^m \frac{c_j}{b_j} (\lambda_i^{b_j} - 1) \quad \text{----- (2.27)}$$

where  $c_j$  and  $b_j$  are the material coefficients and  $\lambda_i$  are the three principal extension ratios in a certain direction ( $i = 1,2,3$ ). Other forms of strain energy density function proposed by Ogden are available in Reference (24) for further study.

This material model can be used to determine the mechanical response of hyperelastic materials with high accuracy for large ranges of deformation, if the coefficients  $c_j$  and  $b_j$  are chosen precisely. The assessment of such coefficients can be performed in several ways depending on the degree of accuracy required. These coefficients can be estimated from the Ogden formulations which are dependent on the deformation modes as follows;

i) for simple uniaxial tension

$$\sigma = \sum_j c_j [\lambda^{b_j-1} - \lambda^{-(1+0.5b_j)}] \quad \text{----- (2.28)}$$

where  $\sigma$  is the engineering stress and  $\lambda$  is the uniaxial extension ratio.



ii) for pure shear

$$\sigma = \sum_j c_j [\lambda^{b_j-1} - \lambda^{-(1+b_j)}] \quad \text{----- (2.29)}$$

iii) for equibiaxial deformation

$$\sigma = \sum_j c_j [\lambda^{b_j-1} - \lambda^{-(1+2b_j)}] \quad \text{----- (2.30)}$$

In this model, the initial shear modulus (G) is expressed as half of the sum of the product of coefficients  $c_j$  and  $b_j$ , i.e., for three sets of coefficients,

$$G = 0.5 (c_1 b_1 + c_2 b_2 + c_3 b_3) \quad \text{----- (2.31)}$$

It is also observed that, for incompressible materials, a two term Ogden model will be equivalent to a Mooney-Rivlin model, if the model is set as follows:  $b_1 = 2$ ,  $b_2 = -2$ , while,  $(c_1)_{\text{Ogden}} = 2 (C_{10})_{\text{Mooney}}$  and  $(c_2)_{\text{Ogden}} = -2(C_{01})_{\text{Mooney}}$ .

- Other material models

In addition to the above mentioned models, a large number of other material models have also been proposed. These include the Peng material model and the Peng-Landel material model. The latter is not only the simplest model, but also gives excellent results for a material with a linear stress-strain curve obtained by a uniaxial tensile test. Like Ogden material model, both Peng and Peng-Landel models are based on the assumption that the strain energy density is a separable function of the principal extension ratios and are available commercially only in the TEXPAC finite element programme. More detailed information of these two models can be found in References(13) and (14).

In the case of incompressible materials, Oden<sup>(26)</sup> proposed a Lagrange multiplier method which can be mathematically expressed as;

$$W = W(I_1, I_2) + \frac{P}{2} (I_3 - 1) \quad \text{----- (2.32)}$$

where  $P$  is the Lagrange multiplier of the constraints, represented by hydrostatic pressure.

While all the models presume isothermal conditions, Nicholson and Nelson<sup>(2)</sup> attempted to account for the temperature effects. They proposed a strain energy density function based on a simple extension of the Mooney-Rivlin model as;

$$W(T) = C_1 (I_1 - 3) + C_2 (I_2 - 3) + \rho T_0 C_3 (T/T_0) \ln (T/T_0) + 2 C_4 (T - T_0) (I_1 - 3) \quad \text{----- (2.33)}$$

Some material models have also been developed particularly for nearly incompressible materials. In this case, the initial bulk modulus must be included. A three parameter model developed by Fried and Johnson<sup>(27)</sup> for compressible materials can be expressed as;

$$W = C_1 (I_1 - 3I_3^{1/3}) + C_2 (I_2 - 3I_3^{2/3}) + \frac{1}{2} C_3 (\ln I_3)^2 \quad \text{----- (2.34)}$$

where  $C_1$  and  $C_2$  are essentially the Mooney-Rivlin coefficients, while  $C_3$  is a bulk modulus, the change in hydrostatic pressure required to affect a unit change in volume.

For the hyperelastic material model proposed by George, Haduch and Jordan<sup>(28)</sup>, the Mooney-Rivlin model can be expressed as follow;

$$W = C_1 (I_1 - 3) + C_2 (I_2 - 3) + C_3 (I_3^2 - 1) + C_4 (I_3 - 1)^2 \quad \text{----- (2.35)}$$

$$\text{where } C_3 = \frac{1}{2} C_1 + C_2 \quad \text{----- (2.36)}$$

$$C_4 = \frac{1}{2} [ C_1 (5\nu - 2) + C_2 (11\nu - 5) ] / (1 - 2\nu) \quad \text{----- (2.37)}$$

Again,  $C_1$  and  $C_2$  are the Mooney-Rivlin coefficients and  $\nu$  is the Poisson's ratio, ranging from 0.499 to 0.49999. In accordance with this range of Poisson's ratio, Finney<sup>(29)</sup> carried out the tests to determine shear modulus for elastomers and revealed that

Poisson's ratio of these materials is actually between 0.499 and 0.4999. In this published work, an advanced FE programme was introduced to overcome the compressible problem by incorporating the so-called Herrmann's modified variational principle. However, this is beyond the scope of this project, so it is not described herein.

### 2.2.3 Commercial software for FEA in elastomer design

FEA is a numerical technique for which the use of computer hardware and software is inevitably required. In general, the selection of suitable software package must be taken into consideration by the designer. There is no general purpose software that can be used for all kind of problems. Therefore, it is useful to give here some commercially marketed finite element software (or sometimes called finite element codes) that can be used to analyse elastomeric components.<sup>(9)</sup>

- ♦ ABAQUS by Hibbitt, Karlsson, and Sorensen, Providence, RI.
- ♦ ADINA by Adina Engineering, Watertown, MA.
- ♦ MARC By Marc Analysis Research Corporation, Palo Alto, CA.
- ♦ NISA by Engineering Mechanics Research Corporation.
- ♦ ANSYS by ANSYS, Inc., Houston, PA.

Material data, covering the ranges of stress and strain anticipated in the subsequent analyses, is usually needed for most FE programmes. The efficiency of such programmes is related directly to the accuracy of this input material data. In general, when the test data input is specified, the programme starts performing some type of curve fitting routine, normally a regression based on the least squares technique, to estimate the material model coefficient values. The material model and its previously obtained coefficients are then used by the FE programme to interpolate and extrapolate stress-strain values for other deformation modes throughout the solution. Nevertheless, some FE programmes permit the use of relevant coefficients as direct input data if these

coefficients have been determined by independent means, as illustrated in the following section.

## 2.2.4 Experimental determination of elastic behaviour of rubber compounds

As previously mentioned, to use FEA, the elastic material constants must be determined. In this section, a review of experimental procedures for characterisation of the material constants for the most two important models: Mooney-Rivlin and Ogden models is presented. In addition, a general approach for determination of strain energy density functions is also given.

### 2.2.4.1 For Mooney-Rivlin material model

For isotropic and incompressible material, the Mooney-Rivlin strain energy density function of can be expressed as;

$$W = C_{10} (I_1 - 3) + C_{01} (I_2 - 3) \quad \text{----- (2.38)}$$

For a special case of uniaxial tension or compression, the stress-strain relation is given by;

$$\frac{\sigma}{(\lambda - \lambda^{-2})} = 2 \left( \frac{\partial W}{\partial I_1} + \frac{1}{\lambda} \frac{\partial W}{\partial I_2} \right) \quad \text{----- (2.39)}$$

where  $\sigma$  is the Cauchy or engineering stress.

For simple shear, the stress-strain relation becomes

$$\frac{\tau}{\gamma} = 2 \left( \frac{\partial W}{\partial I_1} + \frac{\partial W}{\partial I_2} \right) \quad \text{----- (2.40)}$$

where  $\tau$  is the shear stress and  $\gamma$  is the shear strain which is given in the form of the invariant  $I_1$  by  $\gamma^2 = (I_1 - 3)$ .

For a Mooney-Rivlin material, the partial derivatives  $\frac{\partial W}{\partial I_1}$  and  $\frac{\partial W}{\partial I_2}$  represent  $C_{10}$  and  $C_{01}$ , respectively, so that the Equations (2.39) and (2.40) become

$$\frac{\sigma}{2(\lambda - \lambda^{-2})} = \left( C_{10} + \frac{1}{\lambda} C_{01} \right) \quad \text{----- (2.41)}$$

$$\text{and } \frac{\tau}{\gamma} = 2 (C_{10} + C_{01}) \quad \text{----- (2.42)}$$

In the case of simple tension, if  $\left( \frac{\sigma}{2} \right) (\lambda_1 - \lambda_1^{-2})^{-1}$  is plotted against  $\lambda_1^{-1}$ , the resulting plot will yield a straight line with the slope of  $C_{01}$  and the interception of the vertical axis at  $\lambda_1^{-1} = 1$  is  $(C_{10} + C_{01})$ . A typical Mooney-Rivlin material plot for a simple tension is given as an example in Figure 2.6.

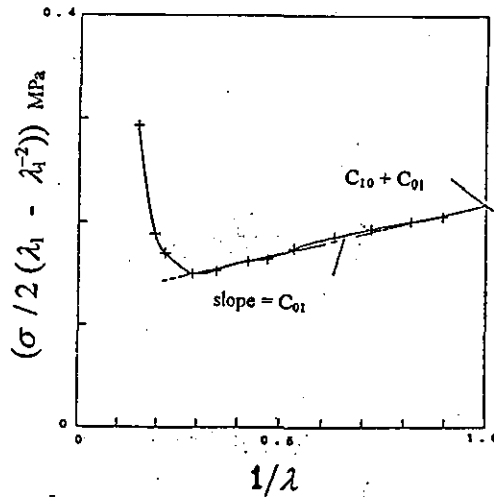


Figure 2.6 Mooney-Rivlin plot<sup>(11)</sup>

Figure 2.6 shows a good agreement between experimental data and Equation (2.41), apart from the marked upturn at large strain which is associated with the finite extensibility of the macromolecular network<sup>(30)</sup> and crystallisation.<sup>(31)</sup>

Since the Mooney-Rivlin form is derived from the linear relation between stress and strain, this form remains valid only from small to moderate deformation (say, less than

100% strain). Rivlin and Saunders<sup>(31)</sup> pointed out that the Mooney-Rivlin material constants obtained by fitting a line to tensile data are not appropriate for predicting behaviour of rubber in other deformation modes. In spite of the foregoing disadvantages, the Mooney-Rivlin model is still favoured by many workers because it is simple and easily adaptable to routine use, even though some precision may be sacrificed.

#### 2.2.4.2 Ogden material model

The Ogden material model represents the separability of the dependence of the strain energy density function on  $\lambda_1$ ,  $\lambda_2$  and  $\lambda_3$ . For incompressible materials, the strain energy density function can be expressed as;

$$W = \sum_{i=1}^3 \sum_{j=1}^m \frac{c_j}{b_j} (\lambda_i^{b_j} - 1) \quad \text{----- (2.43)}$$

where  $c_j$  and  $b_j$  are the material coefficients and  $\lambda_i$  are the three principal extension ratios ( $i = 1, 2, 3$ ). The coefficients required for FE programme can be developed from either one or combination of these methods; a simple tension, pure shear and an equibiaxial tension. The Ogden formulations are given in the Equations (2.44), (2.45) and (2.46) for a simple tension, pure shear and equibiaxial tension modes, respectively.

$$\sigma = \sum_j c_j [\lambda^{b_j-1} - \lambda^{-(1+0.5b_j)}] \quad \text{----- (2.44)}$$

$$\sigma = \sum_j c_j [\lambda^{b_j-1} - \lambda^{-(1+b_j)}] \quad \text{----- (2.45)}$$

$$\sigma = \sum_j c_j [\lambda^{b_j-1} - \lambda^{-(1+2b_j)}] \quad \text{----- (2.46)}$$

where  $\sigma$  is the engineering stress and  $\lambda$  is the principal extension ratio.

The number of coefficients required to fit the curve depends on the amount of accuracy desired. In general applications, three sets of coefficients are found to be sufficient to fit the data for most highly elastic rubber vulcanisates. Finney and Kumar<sup>(11)</sup> presented a concept and methodology to develop three sets of Ogden coefficients as follows.

Generally, the problem seems to demand a nonlinear regression analysis, however, with careful selection of the initial values of the three sets of coefficients, a simple least squares technique together with linear iterations on  $b_j$  can be applied to characterise the values of Ogden coefficients.

By considering three sets of coefficients, the above three equations can be written in the following form;

$$\sigma = c_1 K_1 + c_2 K_2 + c_3 K_3 \quad \text{----- (2.47)}$$

where  $K_1$ ,  $K_2$  and  $K_3$  are the quantities shown in parentheses in Equations (2.44) to (2.46). If  $N$  data points (i.e.,  $\sigma_i$ ,  $\lambda_i$ ,  $i = 1, N$ ) are collected from experiment, the above equation can be written in the matrix form as;

$$\begin{matrix} \{\sigma\} \\ N \times 1 \end{matrix} = \begin{matrix} [K] \\ N \times 3 \end{matrix} \begin{matrix} \{c\} \\ 3 \times 1 \end{matrix} \quad \text{----- (2.48)}$$

The error  $\{e\}$  in the calculated and the experimental values of  $\{\sigma\}$  can be expressed as;

$$\{e\} = \{\sigma\} - [K] \{c\} \quad \text{----- (2.49)}$$

From the above equation, the least squares technique can be derived by minimising the error or  $[(\sigma_i - K_i c)^2]$  with respect to  $(c_j, j = 1, 3)$ , or in matrix notation, by minimising  $(\{\sigma\} - [K]\{c\})^T (\{\sigma\} - [K]\{c\})$  with respect to  $\{c\}$ . By using calculus,

$$\frac{d}{dc} \left( \{\sigma\} - [K]\{c\} \right)^T \left( \{\sigma\} - [K]\{c\} \right) = 0$$

$$\text{or} \quad [K]^T [K] \{c\} = [K]^T \{\sigma\}$$

$$\text{or} \quad \{c\} = ([K]^T [K])^{-1} [K]^T \{\sigma\} \quad \text{----- (2.50)}$$

From Equation (2.50), the coefficients  $c_1$ ,  $c_2$  and  $c_3$  can be calculated from particular values of  $b_1$ ,  $b_2$  and  $b_3$ .

The procedure to calculate the Ogden coefficients based on the tensile stress-strain data is summarised as follows.

1. Run a uniaxial tension test and plot a curve for  $\sigma$  and  $\lambda$ .
2. Extract N sets of  $\sigma$  and  $\lambda$  from the curve (N should be sufficiently large enough to represent the whole curve). Preferably select  $(\sigma, \lambda)$  set at an interval of  $\lambda = 0.1$ .
3. Assuming that the data fit Equation (2.44), then,

$$\sigma_{\text{anal}} = c_1 [\lambda^{b_1-1} - \lambda^{-(1+0.5b_1)}] + c_2 [\lambda^{b_2-1} - \lambda^{-(1+0.5b_2)}] + c_3 [\lambda^{b_3-1} - \lambda^{-(1+0.5b_3)}] \quad \text{----- (2.51)}$$

4. Let  $K_1$ ,  $K_2$  and  $K_3$  be the quantities in the square parentheses, respectively. Select the initial values of  $b_1$ ,  $b_2$  and  $b_3$  as 0.1, 1.0 and -0.1, respectively and calculate  $K_1$ ,  $K_2$  and  $K_3$  for all the N number of points, giving matrix  $[K]$  of size  $N \times 3$ .
5. Calculate  $c_1$ ,  $c_2$  and  $c_3$  by using the following equation;

$$\{c\} = ([K]^T [K])^{-1} [K]^T \{\sigma_{\text{exp}}\} \quad \text{----- (2.52)}$$

6. Based on Equation (2.51), the values of  $c_1$ ,  $c_2$  and  $c_3$  can be used to calculate  $\sigma_{\text{anal}}$  for all N data points. Then calculate the sum of the square of the error  $(\sigma_{\text{anal}} - \sigma_{\text{exp}})$ , designated by SSE and compare it with the SSE calculated in the previous iteration. Store new SSE and the corresponding values of  $b_1$ ,  $b_2$ ,  $b_3$ ,  $c_1$ ,  $c_2$  and  $c_3$ , if the new SSE is found smaller than the previous one.
7. Vary  $b_1$ ,  $b_2$  and  $b_3$  at 0.1, 1.0 and -0.1 interval respectively and repeat steps 3 to 6 above; the coefficients  $b_1$ ,  $b_2$ ,  $b_3$ ,  $c_1$ ,  $c_2$  and  $c_3$  corresponding to the least SSE over 20 iterations would give sufficiently close results to the experimental data.

#### 2.2.4.3 General approach for determination of strain energy density function

Apart from the Mooney-Rivlin and Ogden models, attempts to characterise elastic behaviour of rubber have been successfully conducted by many workers. For example, Finney and Kumar<sup>(11)</sup> again proposed a practical procedure to develop both Peng and Peng-Landel material constants by using the results from a simple tension test, combined with either strip biaxial or an equibiaxial test.



Obata *et al.*<sup>(32)</sup> introduced a new approach to evaluate the strain energy density function empirically by using a specially designed apparatus for strip biaxial testing. For homogeneous biaxial deformation, the engineering stress  $\sigma_1$  and  $\sigma_2$  can be expressed in terms of;

$$\sigma_1 = \frac{2}{\lambda_1} \left( \lambda_1^2 - \frac{1}{\lambda_1^2 \lambda_2^2} \right) \left( \frac{\partial W}{\partial I_1} + \lambda_2^2 \frac{\partial W}{\partial I_2} \right) \quad \text{----- (2.53)}$$

$$\sigma_2 = \frac{2}{\lambda_2} \left( \lambda_2^2 - \frac{1}{\lambda_1^2 \lambda_2^2} \right) \left( \frac{\partial W}{\partial I_1} + \lambda_1^2 \frac{\partial W}{\partial I_2} \right) \quad \text{----- (2.54)}$$

Then  $\frac{\partial W}{\partial I_1}$  and  $\frac{\partial W}{\partial I_2}$  can be calculated by substituting the data sets of  $\sigma_1$ ,  $\sigma_2$ ,  $\lambda_1$  and  $\lambda_2$

obtained through biaxial experiments into the above equations. Based on this approach,

Seki *et al.*<sup>(33)</sup> found that  $\frac{\partial W}{\partial I_1}$  and  $\frac{\partial W}{\partial I_2}$  are not constant but vary with strain invariants,

particularly in the small strain region. Consequently, a least squares method was used to

find the relation between  $\frac{\partial W}{\partial I_i}$  and  $I_i$ , as shown in the following equation;

$$\frac{\partial W}{\partial I_i} = a_i + b_i (I_i - 3) + c_i (I_i - 3)^2 + d_i \exp [e_i (I_i - 3)] \quad \text{----- (2.55)}$$

A different approach was also introduced by Gregory.<sup>(34)</sup> Based on experimental data, he

found that  $\frac{\partial W}{\partial I_1}$  is much larger than  $\frac{\partial W}{\partial I_2}$ , and therefore, the latter can be neglected

without significant error for engineering applications, especially for filled rubbers.

According to this approach, Yeoh<sup>(23)</sup> proposed a strain energy density function expressed

solely in terms of strain invariant  $I_1$ , known as the cubic strain energy density function

(See Equation (2.25)). With reference to this form of energy density function, the stress-

strain relation for uniaxial tension (or compression) is given by;

$$\frac{\sigma}{(\lambda - \lambda^{-2})} = 2 C_{10} + 4 C_{20} (I_1 - 3) + 6 C_{30} (I_1 - 3)^2 \quad \text{----- (2.56)}$$

while the stress-strain relation in simple shear is

$$\frac{\tau}{\gamma} = 2 C_{10} + 4 C_{20} (I_1 - 3) + 6 C_{30} (I_1 - 3)^2 \quad \text{----- (2.57)}$$

This approach was also supported by Davies *et al.*<sup>(35)</sup> They characterised the behaviour of filled rubber and demonstrated that the strain energy density function can be determined from stress-strain data in any simple deformation mode, i.e., shear or tension, without the necessity of relatively difficult biaxial measurement and this function should then be applicable to other deformation modes.

## 2.2.5 A survey of published work in the application of FEA to rubber

As already mentioned, FEA has become the most powerful technique in the design of engineering components. In recent years, it has been used widely in many fields, i.e., Engineering, Physics and Applied Mathematics. Many analysts have adopted FEA to use as a tool in the design of elastomeric components. As a consequence of material and geometric (in large deformation) nonlinearities as well as incompressible behaviour of rubbers, the application of FEA to rubber design requires more effort, in comparison with other fields of applications. The validity and efficiency of the FE technique have been determined and published by many authors. Meanwhile, several FE programmes have been particularly developed in order to get the best prediction. It is impossible to exhibit all the applications of FEA in the rubber analysis and, therefore, a partial list of published work is given below, many of which involve comparison with experimental data.

- Fukahori and Seki<sup>(36,37)</sup> analysed stress and strain distribution around spherical holes and around rigid spherical particles by using FEA for small to very large deformation. The strain energy function was measured through strip biaxial (pure shear) testing. The numerical predictions were compared to the classical elasticity solutions. The results clearly showed that, in both cases, the computed stress and strain distributions agreed well with the classical theoretical ones at small strain. At

large strain, however, deviations between the numerical prediction and classical theoretical results were found. These tendencies are more pronounced in carbon black filled elastomers than the unfilled ones. They concluded that the deviations were attributed to geometric and material nonlinearities. In addition, the reinforcement of elastomers with rigid spherical particles was also analysed.<sup>(37)</sup> A three dimensional simulation was used as a model because it allowed for better natural boundary conditions, despite the difficulty to obtain the fine meshes. The computed results based on the strain energy density function of the unfilled rubber vulcanisates provided a good agreement with the Guth and Mooney equations at low filler volume fraction. In contrast, for carbon black filled elastomers, the computations yielded a good correlation with the experiments when a 20% increase in effective diameter of the filler was used (considering the effect of bound rubber).

- Morman and Pan<sup>(9,10)</sup> used the ABAQUS programme to analyse and compare the predicted results with the closed-form solutions. Both simple and complicated components, for instance, bonded cylinder, idealised cylindrical rubber bushing, tearing energy specimen, silenbloc bushing and shear-compression engine mount, were analysed. Comparisons revealed that closed-form solutions were valid only for simple components and within infinitesimal strains. They are ineffective for complicated components or for a large range of deformation, for which the use of FEA is effective in this case.
- Chang and Sun<sup>(38)</sup> presented a nonlinear elastic analysis of the hardness test by using both nonlinear finite element analysis theories and closed-form solutions (the Hertz contact solution). The results showed that the elastic Hertz contact solution agreed well with FEA, therefore, they concluded that the linearly elastic Hertz contact solution is a reasonably accurate model.

- Dalgarno *et al.*<sup>(39)</sup> used the ABAQUS programme to analyse synchronous belt tooth failure. Good correlation between results obtained from FEA and those from experiment was demonstrated.
- Seki *et al.*<sup>(33)</sup> proposed a numerical method for the stress-strain analysis of multilayer elastomeric bearing under large deformation. A new apparatus was applied to determine the strain energy density function empirically, called as the strip-biaxial testing machine. A comparison of the results obtained from the experiment and those obtained from the developed numerical method was made and found to be remarkably good over a wide range of deformation.
- Takayama *et al.*<sup>(40)</sup> performed an analysis of a laminated rubber bearing using FEA based on a strain energy density function which was determined through biaxial elongation tests. The computed load-deformation relationship agreed quite well with the experimental results. By using the simulated stress and strain distributions, a mechanism for supporting a vertical load during horizontal deformation was proposed.
- Nicholson and Nelson<sup>(2)</sup> applied the ABAQUS programme, based on the Mooney-Rivlin model, to analyse automotive exhaust hangers. The material data were derived from a uniaxial tension test. A least squares technique was used by the ABAQUS programme to fit the collected data in order to determine the Mooney-Rivlin material constants. After gaining confidence with the estimated constants, the exhaust hanger was modelled and analysed. The deformation mode and stress-strain relation were studied.
- Lindley<sup>(41)</sup> described the application of FEA to the deformation of rubber sheets. The sheet problem was considered as plane stress behaviour in which one of the principal stresses was zero, so that the other principal stresses could be evaluated. In addition,

the plane strain analysis of rubber was also carried out.<sup>(42)</sup> A form of strain energy density function which enabled solutions to be obtained at very high strains (beyond those of linear classical elasticity theory), was also introduced in the published work.

- Tabaddor<sup>(43)</sup> conducted an experiment using FEA, based on the Mooney-Rivlin model (ADINA code), to analyse the problems of a cube under symmetrical loading and a sheet under symmetrical biaxial loads in the states of plane stress and plane strain. The stability of the solutions was evaluated analytically.
- Finney<sup>(29)</sup> illustrated the benefits of FEA in the design of elastomeric components and applied FEA to:
  - i) determine shrinkage or expansion when elastomeric parts are subjected to a thermal load;
  - ii) determine the shape of edge contour to optimise particular properties, and
  - iii) design a helicopter rotor thrust bearing in order to obtain a lower uniform value of shear strain when subjected to a real working condition.
- Medri *et al.*<sup>(44)</sup> applied a new finite element programme, particularly developed for large hyperelastic deformations, to investigate the stress-strain field in fluid seals. Experiments were performed to check the validity of this programme. The numerical data were found in good agreement with the experimental data.
- Cho *et al.*<sup>(45)</sup> used FEA (MARC code) to approximate the local stress of the rubber blocks with thin glass rods in their centres when subjected to tensile stress. The aim of this work was to get a better understanding of internal fracture of an elastomer containing a rigid inclusion.

The above published work only represents some examples of the application of FEA in rubber field. The importance of FEA in rubber design is being significantly increased due to superior advantages of this technique when compared to either cut-and-try process or closed-form solutions.

### 2.3 Dynamic properties of rubbers

Rubber is a very versatile material which has been widely used in many applications. The successful use of rubber components arises from its flexibility, cushioning and damping properties to accommodate unwanted movement. For many engineering purposes, rubber is normally used for applications in which it undergoes rapid dynamic deformation. As a consequence, the use of rubber as an engineering material inevitably requires a basic knowledge of its dynamic properties. It is therefore of great importance to review the dynamic properties of rubber in this section.

#### 2.3.1 Terminology of dynamic properties

Dynamic mechanical properties are generally defined as responses to periodically varying strains or stresses.<sup>(46,47)</sup> When a stress is applied to rubber, the strain does not respond instantaneously to the applied stress. In fact, it lags slightly behind the stress and this lag can be of practical importance in certain circumstances because it causes heat generation in the component. For small deformations in simple extension where a linear stress-strain relation exists, if stress and strain variations are sinusoidal (Figure 2.7), the stress and strain can be represented as;

$$\sigma_{(t)} = \sigma_0 \sin (\omega t + \delta) \quad \text{----- (2.58)}$$

$$\epsilon_{(t)} = \epsilon_0 \sin \omega t \quad \text{----- (2.59)}$$

where  $\sigma_0$  and  $\epsilon_0$  are respectively the stress and strain amplitudes,  $\omega$  is the angular frequency (defined by  $2\pi$  times frequency in cycles per second),  $t$  is the time and  $\delta$  is the lag angle or phase angle between the sinusoidal stress and strain.

The total stress can be decomposed into two components; (i) an elastic stress component which varies strictly in-phase with the strain and (ii) a viscous component which is 90° out-of-phase with the strain. The latter component is 90° in advance of strain because the viscous resistance depends mainly on the deformation rate. The out-of-phase stress therefore reaches a maximum when the strain rate is increasing most rapidly, which takes place when the strain itself is zero.

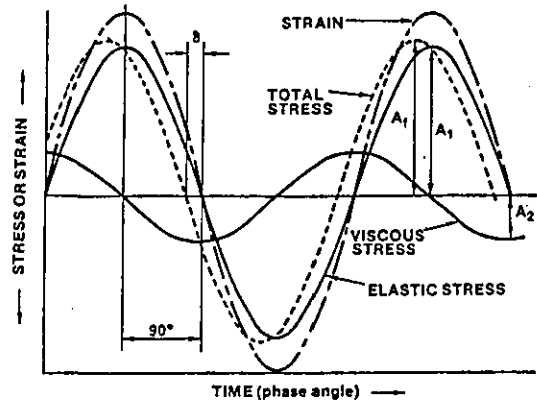


Figure 2.7 Sinusoidal stress and strain cycles

The total stress can then be expressed mathematically as

$$\sigma = \epsilon_0 (E' \sin \omega t + E'' \cos \omega t) \quad \text{----- (2.60)}$$

where  $E'$  is the storage or elastic modulus defined as a measure of elastic energy stored and recovered during the cyclic deformation and  $E''$  is the loss modulus defined as a measure of energy dissipated as heat. Both  $E'$  and  $E''$  can be represented by

$$E' = \text{in-phase stress amplitude/strain amplitude}$$

$$E'' = \text{out-of-phase stress amplitude/strain amplitude}$$

A complex modulus  $E^*$  can then be represented in terms of a vector combination of the two moduli (See Figure 2.8) as

$$E^* = E' + i E'' \quad \text{----- (2.61)}$$

where  $i$  denotes a component 90° out-of-phase.

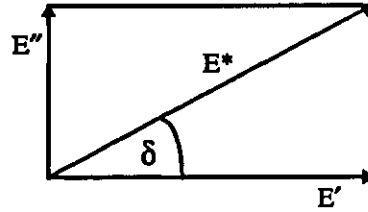


**Figure 2.8** Graphical relation between in-phase, out-of-phase and complex moduli

The absolute value of the complex modulus then becomes

$$|E^*| = \{ (E')^2 + (E'')^2 \}^{1/2} \quad \text{----- (2.62)}$$

The ratio of  $E''/E'$  is  $\tan \delta$ , generally known as “loss factor”, “loss tangent” or “hysteresis factor”. This hysteresis factor is quite important in the practical use of rubber in engineering application as it indicates the amount of energy input to be lost into heat.

Alternatively, the dynamic properties can be expressed in terms of the compliance which is defined as follows.

$$\text{Complex compliance} : C^* = 1/E^*$$

$$\text{Storage compliance} : C' = E'/(E^*)^2$$

$$\text{Loss compliance} : C'' = E''/(E^*)^2$$

For small deformations in simple shear, the corresponding shear moduli  $G'$  and  $G''$  are defined in a manner analogous to the ratio of the in-phase and out-of-phase shear stresses to the practical shear strain. A complex shear modulus ( $G^*$ ) is also represented by a similar equation. Likewise, the letter  $J$  is used instead of  $C$  for the compliance.

Under small deformations, rubbers are considered as linearly elastic materials. Since they possess an extremely high bulk modulus compared to shear modulus, they are always regarded as relatively incompressible materials with the Poisson's ratio approaching 0.5 and the Young's modulus ( $E'$ ) is approximately three times higher than the shear modulus ( $G'$ ).



## 2.3.2 Factors controlling the dynamic properties

Basically, there are several factors controlling the dynamic properties of rubber vulcanisate such as compounding ingredients, processing factors and environmental factors. Some of these factors are given in details below.

### 2.3.2.1 Effects of temperature and frequency and their interaction

The properties of rubber compounds are strongly dependent on both temperature and frequency (or strain rate for static deformation). This is clearly seen from the fact that rubbers progressively stiffen with either decreasing temperature or increasing frequency. It is understandable that a decrease in temperature causes a considerable reduction of thermal energy which is required for thermal motions of rubber molecules. Since rubber deformation depends greatly on these thermal motions, the response of these molecules to the external stress becomes more sluggish and the rubber becomes harder, or in other words, the modulus is increased. If the temperature continues to decrease until it reaches a certain value where no molecular motion can take place, the rubber will behave like a glass in which deformation completely depends on inter-atomic bonds. In the glassy state, very high stress is required for rubber to deform (very high modulus).

A similar response is also obtained with increasing frequency of deformation. As rubber molecules require time to response or deform correspondingly to the applied stress, increasing frequency means that less time is available for deformation to occur, therefore, rubber progressively stiffens with increasing frequency.

Based on changes in properties with frequency, the characteristics of unvulcanised rubber can be divided roughly into four different zones as shown in Figure 2.9.<sup>(46,48)</sup> In the “flow region” where very low frequency is applied, the rubber molecules have enough time to snake through their entanglement constraints and completely rearrange their configurations. In the “rubbery or plateau zone”, the elastic modulus changes very

little with frequency and the loss modulus passes through a minimum. This behaviour is not well understood, however, it is usually interpreted by a concept of entanglement coupling.<sup>(46)</sup>

According to this concept, the entangled macromolecules have a potential to form a network in which they act in some respects as if they were tightly coupled at widely separated points. Within this zone, there is plenty of time for the network strands

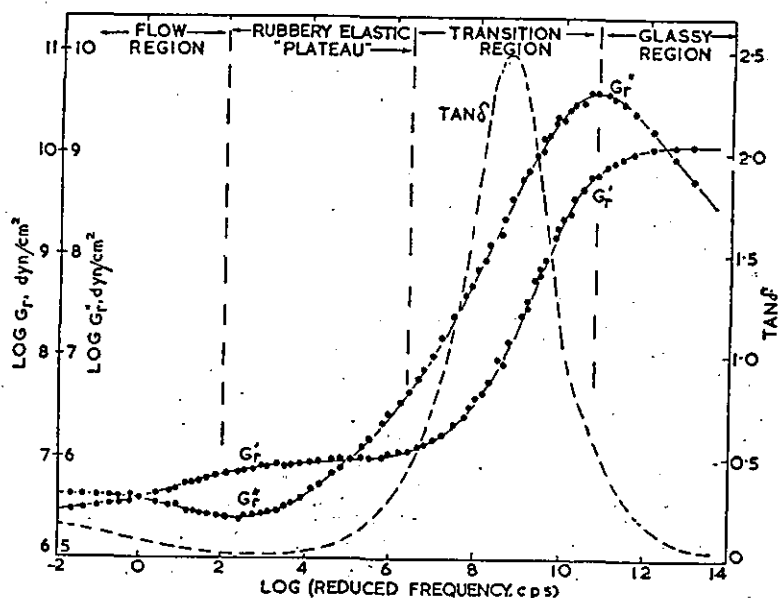


*Figure 2.9* Dynamic properties of unvulcanised NR over a wide frequency range at 25°C<sup>(48)</sup>

between coupling points to rearrange their configurations and store elastic energy through an entropy change but there is not enough time for much more complicated molecular rearrangements such as snaking motions through the entanglements to occur. At higher frequency, the rubber characteristic is passing the rubbery zone into the “transition or semi-rigid zone” where the deformation time becomes too short to allow all the feasible configurational changes of a strand located between two entanglements. Then the strain corresponding to a given stress is less, and the modulus increases with

frequency. A lag between changing stress and changing strain results in the energy loss or energy dissipation and, therefore, both elastic and loss moduli increase with frequency, while  $\tan \delta$  passes through a maximum. In the “glassy zone” where the deformation time is not long enough to permit any conformational rearrangements, the rubber becomes a hard glass-like solid.

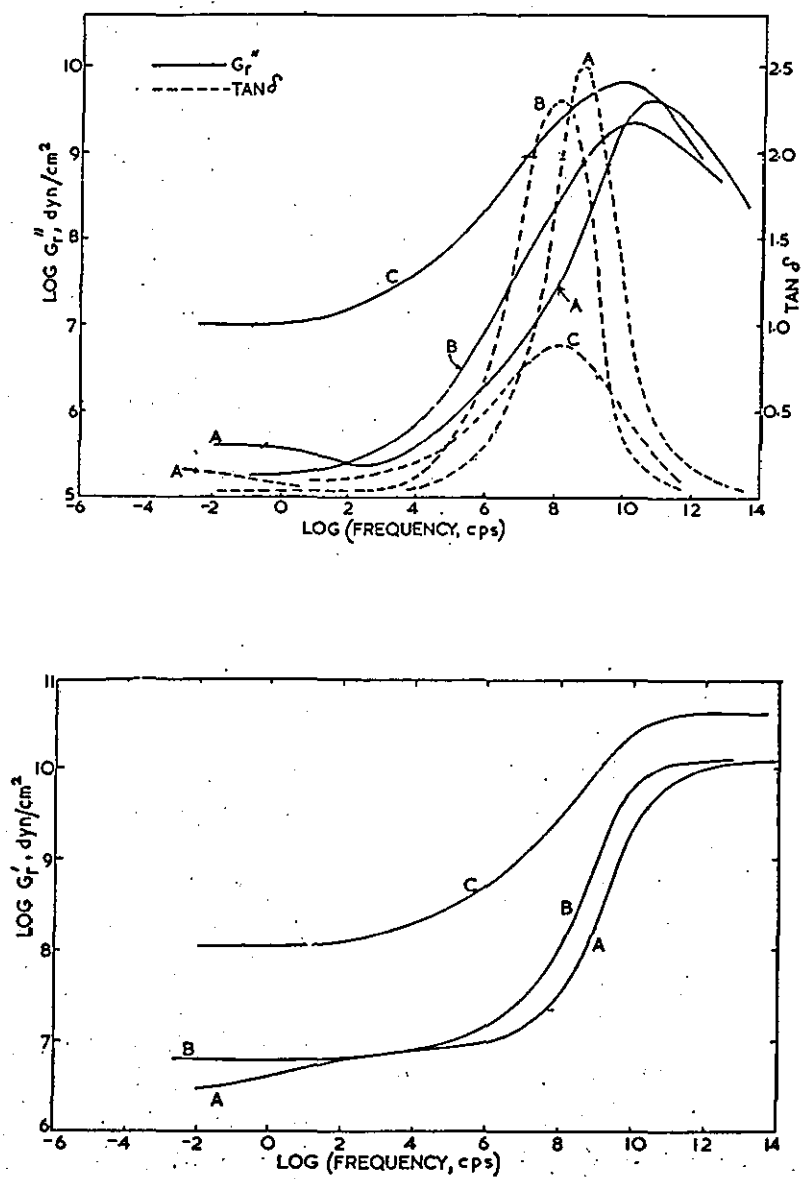


Figure 2.10 Comparisons of dynamic properties between; A, unvulcanised; B, soft vulcanisate without filler, C, CB-filled vulcanisate<sup>(48)</sup>

From the qualitative standpoint, the above pattern is also applicable to the behaviour of vulcanised elastomers (both filled and unfilled ones), as shown in Figures 2.10. Nevertheless, in vulcanised rubber, chemical crosslinks introduce the three-dimensional network structure which prevents a permanent disentanglement of rubber molecules. For this reason, the flow region should not exist in the vulcanised rubbers.

Up to this point, it is important to note that rubbers are most commonly used in the rubber zone where the magnitude of the elastic modulus is in its flat region and the loss (measured by  $\tan \delta$ ) is at minimum.

As previously explained, the effects of increasing frequency and temperature seem to be inversely interrelated. The time-temperature superposition principle holds for various dynamic parameters, so that, a change in temperature from  $T$  to  $T_0$  would give identical effect to a change in frequency from  $\omega$  to  $\omega a_T$ , where  $a_T$  is a shift factor. This shift factor is given by the semi-empirical WLF equation as;

$$\log a_T = \frac{-16.2 (T-T_g)}{55.6 + (T - T_g)} \quad \text{----- ( 2.63)}$$

where  $T_g$  is the glass transition temperature. However, the equation is valid only for unfilled compounds and in a limited zone, say from the glass transition temperature ( $T_g$ ) to about  $T_g + 100^\circ\text{C}$ .<sup>(48,49)</sup>

### 2.3.2.2 Effects of strain amplitude and carbon black

Many workers<sup>(47,50,51)</sup> have found that the dynamic properties of gum vulcanisates are independent of strain amplitude. However, the presence of carbon black (CB), in filled vulcanisates, makes the strain amplitude dependence of the dynamic properties become very pronounced. Because of the interrelation involved, the effects of strain amplitude

and carbon black on dynamic properties of CB-filled vulcanisates will be reviewed simultaneously.

(i) Effect on elastic modulus

The effect of strain amplitude on elastic modulus of CB-filled rubbers has been investigated extensively. During the 1960's, work in this field was dominated by Payne<sup>(50,51,52)</sup> who proposed the mechanism of amplitude effect on dynamic properties of filled vulcanisates. His work was done on both NR and butyl vulcanisates. Experimental results showed that the addition of carbon black considerably increases the elastic modulus of the vulcanisates, especially at very high loading and very low strain amplitude, as can be seen in Figure 2.11.

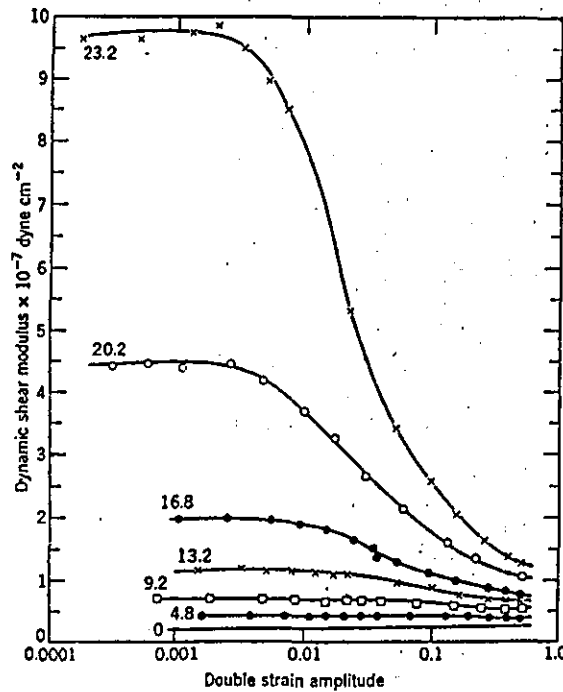


Figure 2.11 Strain amplitude dependence of  $G'$  (IIR with up to 23.2% volume of N330 at ambient temperature, 0.1 Hz)<sup>(50)</sup>

At very low strain, the elastic modulus remains constant (at  $G_0'$ ) up to a certain strain amplitude. With increasing strain amplitude, the elastic modulus starts decreasing up to a relatively high strain amplitude where the elastic modulus levels off at  $G_{\alpha}'$ . The reduction of elastic modulus with strain amplitude is not pronounced in gum and low CB-loading vulcanisates but it is very dominant in vulcanisates with high loading of carbon black. This effect is a consequence of the formation of carbon black structure (sometimes called secondary network) as it is evident that carbon black aggregates in an elastomeric matrix have a tendency to form networks, particularly at high loading giving rise to a secondary structure. Even though this structure is not comparable to the continuous network, it has a significant effect on the properties of filled rubber at very low strain. With increasing strain amplitude, the structure is partly destroyed, resulting in the reduction of elastic modulus until the structure is completely destroyed where the elastic modulus becomes constant. The difference in modulus ( $\Delta G' = G_0' - G_{\alpha}'$ ) is therefore attributable to interaggregate association at low amplitude. It has been shown by many published work<sup>(47,53,54)</sup> that the effect of carbon black on elastic modulus at high strain ( $G_{\alpha}'$ ) depends on structure of carbon black and does not depend on surface area of black. On the other hand, Medalia<sup>(55)</sup> and Payne<sup>(56,57)</sup> revealed that  $\Delta G'$  is a function of surface area but independent of structure of black. By definition,  $G_0' = G_{\alpha}' + \Delta G'$ , thus  $G_0'$  should be a function of structure of carbon black which governs  $G_{\alpha}'$ , surface area and other carbon black properties as well as the degree of dispersion which govern  $\Delta G'$ . In addition, Payne *et al.*<sup>(51)</sup> also found that, at high strain where the carbon black network is completely broken down, the modulus of the filled vulcanisate is still higher than that of the corresponding gum vulcanisate. This difference has been considered as a hydrodynamic effect. The principle of the hydrodynamic theory was first originated by Einstein<sup>(58)</sup> based on the effect of a suspension of spherical particles on the viscosity of a liquid. Then this theory was applied to explain the properties of rubber compounds by Smallwood<sup>(59)</sup> and Guth.<sup>(60)</sup> They proposed that the addition of carbon black increases the modulus of gum compound by the factor of  $X$  which is given by;

$$X = 1 + 2.5 \psi + 14.1 \psi^2 \quad \text{----- (2.64)}$$

where  $\psi$  is the volume fraction of the spherical filler particles.

Equation (2.64) is generally known as Guth and Gold equation and is valid only if the filler particles are spherical. Unfortunately, most carbon blacks depart considerably from spherical shape. Therefore, modification of Equation (2.64) was done by Medalia.<sup>(61)</sup> He suggested that the volume fraction of filler,  $\psi$ , must be replaced by the effective filler volume fraction,  $v$ ; so that Equation (2.64) becomes

$$X = 1 + 2.5 v + 14.1 v^2 \quad \text{----- (2.65)}$$

The effective filler volume fraction includes the rubber which is trapped within the indentations and void space of the carbon black aggregates and prevented from responding to the strain field of the surrounding elastomeric matrix. This rubber is called “occluded rubber” and it does not participate in any deformation process.

#### (ii) Effect on loss tangent ( $\tan \delta$ ) and loss modulus

Like elastic modulus, there is also a dependence of the loss tangent on amplitude, which is again more pronounced as the loading of carbon black is increased.<sup>(47)</sup> As can be seen from Figure 2.12,  $\tan \delta$  is low at very low amplitude. With increasing strain amplitude,  $\tan \delta$  rises to a maximum and then decreases somewhat. Obviously, an increase in carbon black loading affects the  $\tan \delta$  considerably; the higher the loading of carbon black, the greater the value of  $\tan \delta$ .<sup>(50-52)</sup>

In addition to carbon black loading, Medalia and co-workers<sup>(53,62)</sup> also found that  $\tan \delta$  is strongly dependent on the surface area but independent of the structure of carbon black. However, it should be realised that, since the structure of carbon black considerably affects the elastic modulus and  $E'' = E' \tan \delta$ , it also affects the loss modulus. The

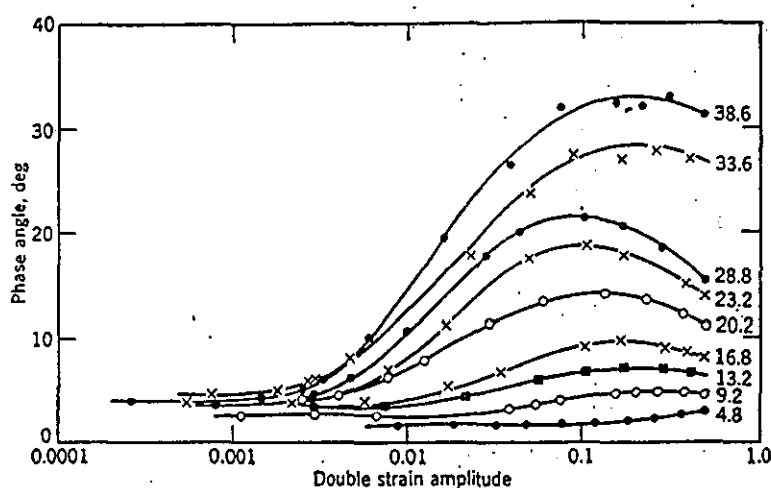


*Figure 2.12* Strain amplitude dependence of phase angle of CB-filled butyl vulcanisates<sup>(50)</sup>

dependence of loss modulus on strain amplitude is similar to that of loss tangent (See Figure 2.13). The loss modulus passes through a maximum as a function of strain amplitude.

The effect of carbon black dispersion on  $\tan \delta$  is also of great importance, as many authors<sup>(62-65)</sup> have shown that  $\tan \delta$  decreases with improved carbon black dispersion. This is possibly due to the reduction of carbon-carbon frictional losses as the dispersion is improved. In the same standpoint, an increase in rubber-carbon interaction, which can result in better dispersion during mixing process, also decreases the  $\tan \delta$ . It is believed that improved dispersion on the micro-level, as the rubber-carbon interaction is increased, is attributable to (i) more successful separation of the carbon black aggregates from each other during mixing owing to the additional drag of the surface-bonded polymer molecules and (ii) prevention of reagglomeration of carbon black aggregates after mixing.<sup>(47)</sup> An increase in interaction between rubber and carbon black can be achieved by several techniques such as the addition of promoters or surface oxidation of carbon black, etc.<sup>(66)</sup>



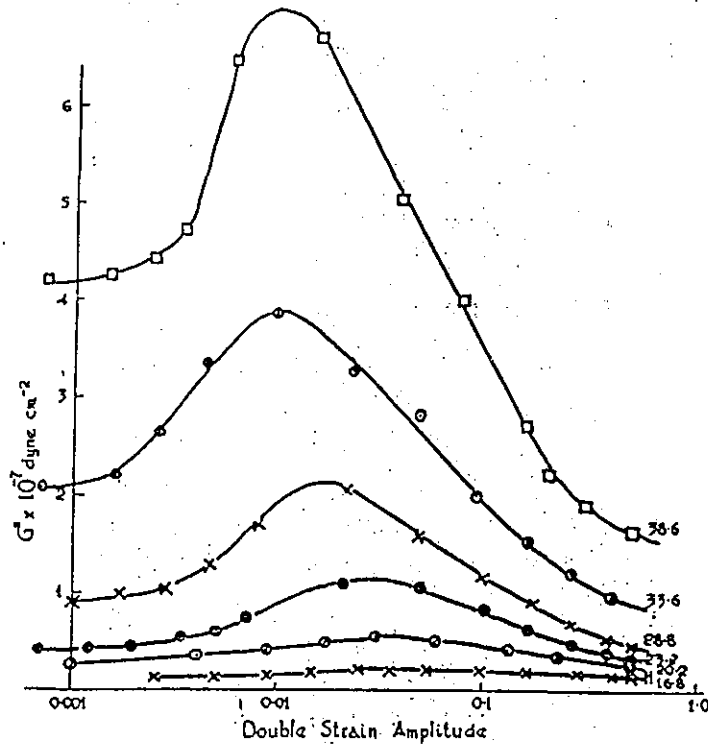


Figure 2.13 Strain amplitude dependence of loss modulus of CB-filled butyl vulcanisates<sup>(52)</sup>

### 2.3.2.3 Effect of crosslink density

It is widely known that the modulus of rubber vulcanisate is proportional to the crosslink density. Payne *et al.*<sup>(51)</sup> has found that an increase in the degree of crosslinking increases the elastic modulus of both gum and filled vulcanisates. On the contrary,  $\tan \delta$  tends to decrease with increasing crosslink density. Similar results were also obtained by Meyer and Sommer<sup>(67)</sup> who found the reduction of  $\tan \delta$  in CB-filled SBR vulcanisate as the amount of sulphur was increased up to a certain value before the  $\tan \delta$  remained constant.

### 2.3.3 Hysteresis and heat generation

As mentioned earlier, rubber is not a perfectly elastic material, as it is made-up from both elastic and viscous components. The viscous component gives rise to the phase difference ( $\delta$ ) between stress and strain during dynamic deformation. This means that a part of the energy input during deformation is not recovered during the recovery part of the cycle. This irreversible part of energy is termed as “energy loss” or “hysteresis” which is the main source of heat generation in rubber component.

#### 2.3.3.1 Molecular aspects of hysteresis

##### ◆ Hysteresis in unfilled elastomers

For unfilled elastomers, the viscous component which is responsible for hysteresis arises from friction of rubber molecules during the deformation.<sup>(49)</sup> This deformation involves dragging of rubber chains and chain segments within the rubber. If the molecular chains are forced into new locations more rapidly than the creation rate of vacant sites (holes) which takes place due to the thermal motion of the surrounding molecules, some of the mechanical energy input must be converted into thermal energy (heat) to promote random thermal motion of these molecules. The creation of vacant sites may be regarded as migration of holes constituting the free volume of the rubber. At lower temperatures, the vacant sites are created less rapidly giving rise to an increase in molecular friction and, hence, hysteresis. Increasing frequency of deformation also gives a similar effect as decreasing temperature. At adequately low temperature (or high frequency), the rubber characteristic approaches the glassy state where it becomes impossible for molecular motion to occur. In the transition zone between rubbery and glassy state, the hysteresis factor ( $\tan \delta$ ) increases to a maximum as the molecular motion becomes more difficult meaning that more thermal energy is needed to create the vacant sites. Then the

hysteresis factor starts falling again as the molecular motion is suppressed in the glassy zone.

The effect of crosslinks is also of particular importance for molecular friction of rubber. Crosslinks and trapped entanglements, which are defined as entanglements that cannot be unravelled because each of the entangled subchains leads to crosslinks at both ends, impede the motion of molecular segments to which they are attached.<sup>(49)</sup> The higher the crosslink density, the lower the amount of dangling chain ends and of untrapped entanglements. Since friction is brought about by dragging of these species, higher crosslink density therefore causes lower friction and, hence, lower hysteresis.

#### ◆ Hysteresis in carbon black reinforced elastomers

Apart from the internal friction of rubber matrix, in filled rubber compounds, reinforcing filler such as carbon black (CB) also plays a major contribution to hysteresis and heat generation.<sup>(47)</sup> Carbon black is normally in the form of aggregates of primary particles fused together. As previously mentioned, these carbon black aggregates in rubber matrix tend to form agglomerates, especially at high loading, leading to chain-like filler structures which are generally termed “secondary network” or “carbon black network”.<sup>(68)</sup> At low amplitude, there is little breakdown of interaggregate bonds, therefore, hysteresis is very low. However, when a rubber compound is stretched to a larger magnitude of strain, a continuous process of network breakdown and reformation takes place.<sup>(49,69)</sup> Increasing strain causes breakdown of interaggregate bonds, starting with the weakest bonds and progressing to the stronger bonds. At the same time, as the rubber is distorted, the aggregates form new bonds at new positions, which are again ruptured and then reformed in other positions. The breakage and reformation of the interaggregate bonds is a hysteretic process which takes place consecutively during the deformation and causes a major share of the heat generation in filled compounds. At very high strain amplitudes where the carbon black network is broken down extensively, the reformation of network is very much slower than the cycle time, giving rise to the

reduction of hysteresis factor which represents the fraction of the mechanical energy input converted into heat. At high strain, the hysteresis is mostly dependent on molecular slippage.

### 2.3.3.2 Mathematical aspects of hysteresis and heat generation

When the dynamic stress is plotted against strain, for a single deformation cycle, the resulting plot is called hysteresis loop as shown in Figure 2.14.

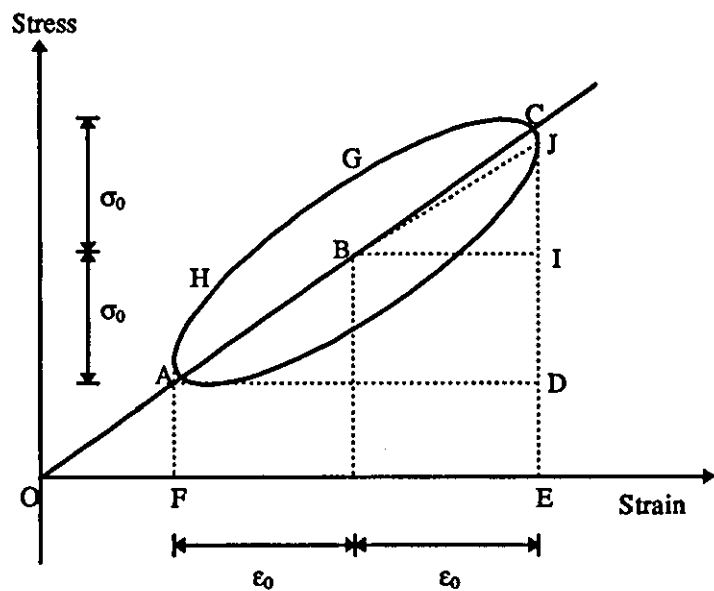


Figure 2.14 Hysteresis loop in dynamic stress strain cycles

If the stress and strain cycles are sinusoidal and the rubber behaviour is linear, the loop will be an ellipse. The slope of the ellipse's main axis (AC) represents the complex dynamic modulus ( $E^*$ ) while the area enclosed by the ellipse is the energy lost per cycle and per unit volume of rubber which can be expressed as;

$$E_{loss} = \pi \sigma_0 \epsilon_0 \sin \delta \text{ ----- (2.66)}$$

where  $\sigma_0$  = stress amplitude  
 $\epsilon_0$  = strain amplitude

Alternatively, the total energy loss for an actual piece of rubber can be obtained by replacing stress and strain amplitudes by the force and deformation amplitudes, respectively.

In addition to Equation (2.66), an expression of energy loss has been proposed in various ways; e.g.,<sup>(48,70)</sup>

$$\begin{aligned} \text{Damping factor} &= \text{area of loop/ area of triangle BIJ} \\ &= 2 \pi \tan \delta \\ \text{Percentage damping} &= (\text{area of loop/ area ADIJGH}) \times 100 \\ &= (1/2) \pi \sin \delta \times 100 / [1 + (1/4) \pi \sin \delta] \\ &= (1/2) \pi \sin \delta \times 100 \quad (\text{if } \delta \text{ is small}) \end{aligned}$$

With reference to Figure 2.14, it should be noted that the area ADC is not the total energy input to the rubber during the deformation from point A to point C. This energy is represented by the area ACDEF. Therefore, the percentage damping is not the percentage of the energy input that is lost. To calculate the actual energy lost in one cycle (area of the loop), the percentage damping must be multiplied by the triangular area ADC (or more precisely area ADIJGH) as represented in Equation (2.67).

$$E_{\text{loss}} = (1/2) \pi \sin \delta (\text{area ADC}) \quad \text{----- (2.67)}$$

As can be seen, Equation (2.67) is identical to Equation (2.66) as the area ADC is equivalent to  $(1/2) (2\sigma_0) (2\epsilon_0)$ .

Since the energy loss is converted into heat and if the rate at which heat is dissipated away is not fast enough, this can cause a considerable temperature rise. This effect is obviously more pronounced in thick rubber components. Theoretically, if it is assumed that there are no heat losses from the component, the rate of temperature rise can be calculated by the following equation.<sup>(71)</sup>

$$\frac{\Delta T}{\Delta t} = \frac{E_{\text{loss}} \cdot f}{C} \quad \text{----- (2.68)}$$

where  $f$  = frequency

$t$  = time

$T$  = temperature

and  $C$  = heat capacity per unit volume

### 2.3.3.3 Practical aspects of hysteresis and energy loss

In engineering design, several parameters should be taken into account in order to reduce the energy loss in the dynamic deformation. Some of these parameters are described below.

#### ♦ Effects of service conditions

##### - Constant strain amplitude conditions

From Equation (2.66), substitution of  $\sigma_0 = E^* \epsilon_0$  yields

$$E_{\text{loss}} = \pi E^* \epsilon_0^2 \sin \delta \quad \text{----- (2.69)}$$

As  $E'' = E^* \sin \delta$ , Equation (2.69) then becomes

$$E_{\text{loss}} = \pi E'' \epsilon_0^2 \quad \text{----- (2.70)}$$

Equation (2.70) shows that energy loss per cycle and per unit volume of rubber ( $E_{\text{loss}}$ ) is directly proportional to the loss modulus ( $E''$ ) under the constant strain conditions. Meinecke and Taft<sup>(72)</sup> proposed that  $E''$  is, as a good first approximation, independent of frequency and temperature range within which elastomers are normally used in technical applications. This implies that, under the constant strain conditions, the energy loss per cycle and per unit volume of rubber is proportional to the square of strain amplitude and independent of the frequency and temperature in this practical range as well.

- Constant stress amplitude conditions

By substituting  $\epsilon_0 = \sigma_0/E^*$ , Equation (2.66) becomes

$$E_{\text{loss}} = \pi \sigma_0^2 \sin \delta / E^* \quad \text{----- (2.71)}$$

Since the loss compliance can be defined as  $C'' = \sin \delta / E^*$ , then

$$E_{\text{loss}} = \pi \sigma_0^2 C'' \quad \text{----- (2.72)}$$

Therefore, under this service condition, hysteresis is proportional to the loss compliance.

- Constant energy input conditions

As can be clearly seen from Equation (2.66), if the energy input ( $\sigma_0 \epsilon_0$ ) is kept constant, the energy loss per cycle and per unit volume of rubber is proportional to  $\tan \delta$ .

◆ Effect of carbon black loading

An addition of carbon black into rubber matrix has a marked effect on the energy loss due to two main reasons. The first one is attributed to the effect of filler networking as previously described. Another reason is attributable to the effect of strain amplification (or hydrodynamic effect).<sup>(73,74)</sup> As the modulus of carbon black is very high compared to that of rubber so that it can be considered as an inextensible filler, the rubber matrix in CB-filled compound has to deform to a larger degree than the macroscopic strain applied. Based on the hydrodynamic theory, the actual strain in elastomeric matrix should be higher than the one applied macroscopically by a factor X which is given by

$$X = 1 + 2.5 v + 14.1 v^2 \quad \text{----- (2.73)}$$

Where v is the effective volume fraction of filler.

On the basis of Equation (2.70), if macroscopic strain is kept constant, the addition of carbon black should increase the energy loss with the square of the strain amplification factor, provided that the presence of carbon black does not change the energy dissipation

process inside the elastomeric matrix. In the meantime, the volume of elastomeric matrix subject to hysteretic loss is reduced by the amount of occluded rubber. Consequently, it might be thought to cause a reduction in the energy loss per cycle per unit volume. However, Meinecke<sup>(75)</sup> has shown that this effect should not be taken into account. Moreover, he also found that the effect of carbon black loading on energy loss is insignificant if the rubber is subjected to constant stress amplitude conditions. This is a consequence of the enhanced modulus which results in a reduction of macroscopic strain by the factor of  $X$ . In the meantime, the local microscopic strain in the elastomeric matrix is increased by the same amount. Therefore, the effect of strain amplification is counterbalanced in this case.

#### ◆ Effect of crosslink density<sup>(75)</sup>

Since the modulus is directly proportional to the crosslink density, an increase in crosslink density will decrease the value of  $\tan \delta$  ( $E''/E'$ ). It is important to note that the reduction in  $\tan \delta$  is mostly attributed to a change in elastic response ( $E'$ ) rather than in the viscous response ( $E''$ ). Increasing crosslink density means that higher stress is required at the same strain amplitude and, at the same time, it reduces the value of  $\tan \delta$ . With reference to Equation (2.66), the effect of increased stress amplitude counterbalances that of reduced  $\tan \delta$ . Therefore, under constant strain amplitude, the energy loss is not significantly dependent on crosslink density.

On the contrary, under constant stress amplitude, the increase in modulus with crosslink density leads to reductions of both strain amplitude and  $\tan \delta$ . As a result, the energy loss decreases with increasing crosslink density in this condition. Likewise, under constant energy input conditions, an increase in crosslink density reduces the value of  $\tan \delta$ , resulting in the reduction of energy loss.



#### 2.3.3.4 The effects of hysteresis and heat generation on elastomers

Heat generation causes a temperature rise in rubber components. Possible physical consequences of higher temperature include deterioration of some properties such as ultimate tensile strength, abrasion resistance, decreased modulus in filled vulcanisates, etc. More serious consequence arises from the chemical effects which take place faster at elevated temperature. Oxidation reactions are of great concern in this case because they play a major part not only in the properties of rubber but also in the fatigue life of rubber components. One such reaction is responsible for changes in the crosslink system. Basically, oxidation of unstretched rubber network causes both chain scission and crosslinking. If the former is predominant, the elastomer softens, while if the latter is predominant, the elastomer stiffens and finally becoming brittle. Either condition will weaken an elastomer. It is apparent that the amount of chain scission will be greater than that of crosslinking in a stretched network due to the chain rupture resulting from mechanical loading.<sup>(76)</sup> Even though the oxidation reaction is a slow process at ambient temperatures, however, over a long periods of time, the effects of chemical changes are accumulated. Obviously, oxidation is speeded up at higher temperatures, therefore, it can be expected that an increase in temperature accelerates changes in the properties of rubber compounds.

In addition, it is also evident that an increase in temperature gives rise to higher crack growth rate, resulting in a lower fatigue life of rubber component.<sup>(77,78)</sup> However, the degree of increase in crack growth rate is strongly dependent on the type of elastomer.<sup>(79)</sup> Experimental results obtained by Lake and Lindley<sup>(80)</sup> show that an increase in temperature yields a dramatic reduction in the fatigue life of SBR gum vulcanisates (See Figure 2.15).

The results correlate well with the increase in static cut growth rate measured over the same temperature range by Greensmith and Thomas<sup>(81)</sup> on another SBR gum vulcanisate. However, they also found that the effect of temperature on fatigue life of NR vulcanisate

is not very pronounced due to crystallising effect. On the contrary, Young<sup>(78)</sup> studied the effect of temperature on fatigue crack growth of NR gum compound and found that an increase in temperature from ambient temperature (25°C) causes a considerable increase in fatigue crack growth rate, leading to a marked reduction of fatigue life.

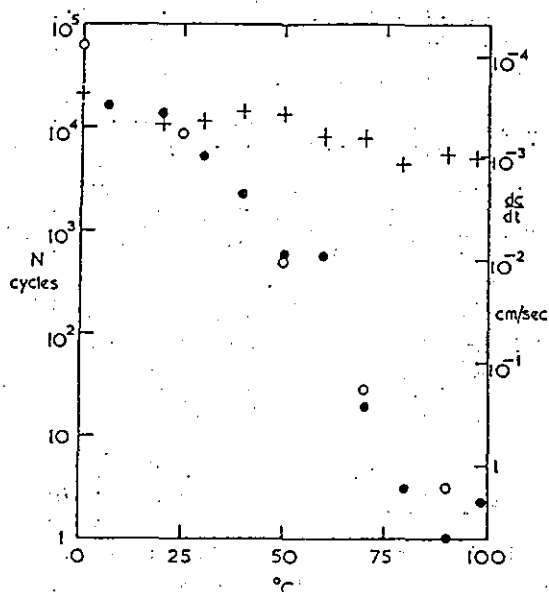
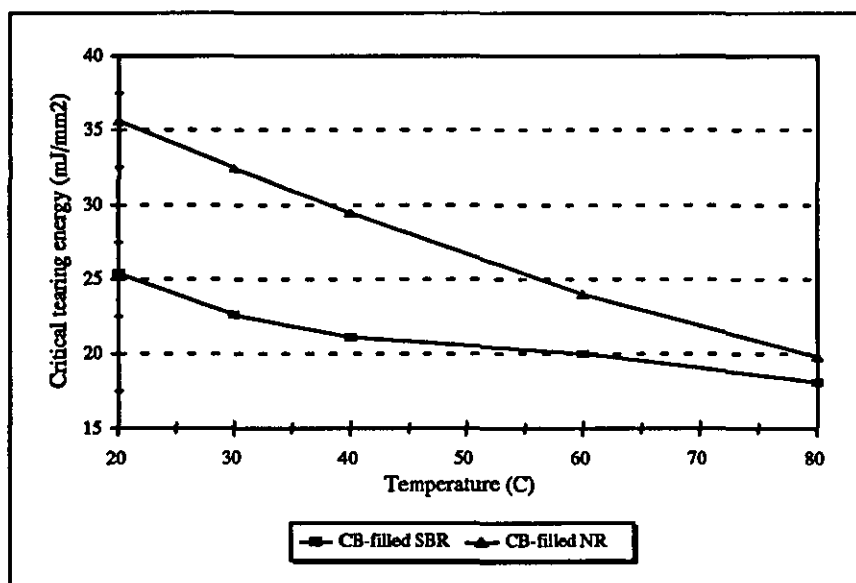


Figure 2.15 Temperature dependence of fatigue life of SBR and NR at 100 cycles/min.; (●) SBR at 175% max. strain; (+) NR at 250% max. strain (left hand scale)<sup>(80)</sup>; (o) cut growth rate at constant tearing energy obtained by Greensmith and Thomas<sup>(81)</sup> on another SBR gum vulcanisate (right hand scale)

Supportive results of the temperature dependence of fatigue life are also obtained from the work of Gent *et al.*<sup>(82)</sup> They proposed that an increase in temperature not only increases the crack growth rate of SBR gum compounds, but also reduces the threshold tearing energy which is defined as the minimum tearing energy required for crack to grow. This means that premature tearing can take place easily as the temperature increases.

In addition, preliminary analysis of the effect of temperature on the critical tearing energy of CB-filled vulcanisates reveals that the critical tearing energy decreases with increasing temperature (See Figure 2.16). The results suggest that an increase in temperature causes a reduction in strength or resistance to tearing of the rubber vulcanisates. Consequently, premature failure is likely to take place as the temperature is increased.



*Figure 2.16* Temperature dependence of critical tearing energy of filled NR and SBR vulcanisates

Another important phenomenon caused by heat generation is known as “blow out”. This is normally found and considered as a major failure source in thick rubber components. When rubber is deformed, some part of the energy input is transformed into heat. If the heat generated internally is not conducted away rapidly enough, the internal temperature will become high enough to cause the thermal decomposition of the rubber compound. Volatile products resulting from this decomposition can then develop an internal pressure which, if high enough, can tear open a path to the exterior (explosive rupture). In addition to the products of thermal decomposition, the internal pressure can also be brought about by volatilisation of either an ingredient of the rubber mix or a by-product

of vulcanisation. Gent and Hindi <sup>(83)</sup> studied heat build-up and blow-out of rubber blocks. They found that different elastomers have different blow out temperatures:- approximately 180°C for butyl rubber compounds and about 200°C or higher for NR and SBR compounds. Apart from the temperature rise, another factor that governs the blow-out of rubber is the Young's modulus of the rubber at the blow-out temperature. The compounds with low modulus at high temperature will soften and lose resistance to cavity expansion, thus, they are prone to blow out easier than those with high modulus.

#### 2.3.3.5 Basic principles to minimise heat generation

To reduce the resulting deterioration of rubber components subjected to rapid dynamic deformation, certain strategies<sup>(49)</sup> can be applied to minimise heat generation or heat build-up.

- ♦ The components should be designed in such a way that the strain amplitude at all points is kept to a minimum.
- ♦ The rubber should possess low hysteresis at the temperature and frequency of interest. This can be achieved by using the carbon black with grade as coarse as possible (low surface area), provided that the requisite properties are maintained. Alternatively, the loading of black should be kept to a minimum, consistent with strength and modulus. Higher crosslink density is also beneficial in this case, provided that other essential properties such as tear strength are maintained at adequate levels.
- ♦ The rubber should have high resistance to deterioration by heat and oxygen. Some compounding additives such as antioxidants and crack growth inhibitors should be taken into considerations.
- ♦ Low service frequency, high heat conductivity and heat transfer coefficient between rubber and the surroundings are also of great concern to reduce the temperature rise in rubber components.
- ♦ For rubber components subjected to constant strain conditions, heat build-up can be minimised by minimising  $E'' (= E' \tan \delta)$ ; i.e., by using carbon black of low structure to

minimise  $E'$ , and of low surface area to minimise  $\tan \delta$ . On the other hand, for those subjected to constant stress conditions, heat build-up can be minimised by using a black with high structure and low surface area to minimise the loss compliance. At a given modulus, the reduction of  $\tan \delta$  can be achieved by using a low loading of a high structure black.<sup>(53,62)</sup>

♦ Since carbon black dispersion also plays an important role on hysteresis of rubber compound; the better the carbon black dispersion, the lower the hysteresis, other techniques that can improve dispersion of carbon black such as the addition of promoters should be taken into account.

## **2.4 Thermal properties of rubber compounds**

In the previous section, the dynamic properties of rubber were discussed, however, there are a number of other properties such as thermal properties with which engineers should be familiar in a general way, since they may be important for engineering applications of rubber compounds. As a consequence, a basic understanding of heat transfer and thermal properties of rubber is given herein.

### **2.4.1 Basic principle of heat transfer**

Holman<sup>(84)</sup> proposed a definition of heat transfer as “science which seeks to predict the energy transfer which may take place between material bodies as a result of a temperature difference”. The energy transfer is known as heat. There are three modes of heat transfer: conduction, convection, and radiation.

### 2.4.1.1 Conduction heat transfer

When a single body is subjected to a temperature gradient, heat (or energy) will be transferred from the high temperature region to the low temperature region. This mode of heat transfer is called “conduction” and, from Fourier’s law for steady state conduction, the heat transfer rate per unit area is proportional to the normal temperature gradient, as shown in the following equation.

$$\frac{dQ}{dt} = -kA \frac{\partial T}{\partial X} \quad \text{----- (2.74)}$$

where  $\frac{dQ}{dt}$  is the heat transfer rate and  $\frac{\partial T}{\partial X}$  is the temperature gradient in the direction of the heat flow. A is the area at right-angles to the direction of heat flow. The constant k is called the thermal conductivity of the material which is defined<sup>(85)</sup> as “the heat transport in a material per unit temperature gradient per unit area between two isothermal planes”.

In the case of unsteady state (transient) conduction, where the temperature at any point within a body varies with both time and position, the basic Fourier equation becomes a partial differential:

$$\frac{\partial T}{\partial t} = \frac{k}{\rho C} \frac{\partial^2 T}{\partial X^2} \quad \text{----- (2.75)}$$

where C and  $\rho$  are specific heat and density respectively. The expression  $\frac{k}{\rho C}$  is called “thermal diffusivity” of the material and is represented by  $\alpha$ . A high value of  $\alpha$  could either result from a high value of thermal conductivity (k), which would indicate a rapid energy transfer rate, or from a low value of the thermal heat capacity  $\rho C$ . The low value of the heat capacity indicates that less of the energy moving through the material would be absorbed and used to raise the temperature of the material; thus more energy would be available for further transfer. Therefore, the larger the value of  $\alpha$ , the faster will heat diffuse through the material.

### 2.4.1.2 Convection heat transfer

Convection is termed as a mode of heat transfer that takes place between material bodies, for example, between a solid and a gas. When heat exchange occurs between solid and fluid, there is a thermal boundary region or film at the surface in which the temperature changes from that of the solid surface to that of the bulk fluid. The overall effect of convection can be expressed by Newton's law of cooling:

$$\frac{dQ}{dt} = hA(\Delta T) \quad \text{----- (2.76)}$$

Here the heat transfer rate is directly proportional to the overall temperature difference between fluid and the solid surface area. The quantity  $h$  is called as "convection heat transfer coefficient". The heat transfer coefficient is sometimes called the film conduction or film coefficient because of its relation to the conduction process in the thin stationary layer of fluid at the solid surface.

### 2.4.1.3 Radiation heat transfer

In addition to the mechanisms of conduction and convection, heat may also be transferred into regions where a perfect vacuum exists. The mechanism in this case is electromagnetic radiation which is propagated as a result of a temperature difference.

For an ideal radiator or black body, the rate of energy emission is proportional to the fourth power of the absolute temperature (Kelvin, °C+273) of the body. When two bodies exchange heat by radiation, the net heat exchange can be expressed as;

$$\frac{dQ}{dt} = \sigma A(T_1^4 - T_2^4) \quad \text{----- (2.77)}$$

where  $\sigma$  is the proportionality constant, called Stefan-Boltzmann constant with the value of  $5.67\text{E-}08 \text{ W/m}^2\cdot\text{K}^4$ .

For other types of surfaces, like a glossy painted surface or a polished metal plate, less energy will be radiated compared to the black body. However, the total radiation emitted by these bodies still follows the  $T^4$  proportionality but another factor is introduced called “emissivity,  $\epsilon$ ”, which relates the radiation of these surfaces to that of an ideal black surface. It is also noted that not all of the radiation leaving one surface will reach the other surface since some will be lost to the surroundings. The overall heat exchange then becomes;

$$\frac{dQ}{dt} = \sigma F_G F_\epsilon A (T_1^4 - T_2^4) \quad \text{----- (2.78)}$$

where  $F_G$  is the geometric “view factor” function and  $F_\epsilon$  is the emissivity function. Emissivity is the ratio of the intensity (energy emitted per unit time and area) of emitted radiant energy to that emitted by a black body at the same temperature. In general, it is a surface property of a material (not a bulk property) and is a function of temperature. At thermal equilibrium, emissivity and absorptivity of a surface are equal.

## 2.4.2 Thermal properties of rubber compounds

### 2.4.2.1 Thermal conductivity

Thermal conductivity is the basic parameter for defining heat flow in a material. Normally, the thermal conductivity of rubber compounds is inversely proportional to temperature<sup>(86)</sup> but, in the range of 20-90°C, the values of thermal conductivity of both gum and CB-filled compounds are slightly changed, therefore, it can be assumed that the thermal conductivity of rubber is independent of temperature without any significant errors.<sup>(85)</sup>

It is evident that thermal conductivities of raw polymers and their gum vulcanisates are very similar, although crosslinking and vulcanisation additives normally increase conductivity of a polymer somewhat.<sup>(85,87-89)</sup> However, the inclusion of filler has a



marked effect on thermal conductivity of the rubber compounds. Carwile and Hoge<sup>(90)</sup> postulated that 10 phr of carbon black may be expected to increase the thermal conductivity by about 17% at room temperature. In the meantime, Williams<sup>(87)</sup> and Barnett<sup>(88)</sup> also proposed that thermal conductivity was an additive property depending on the volume fractions of the ingredients and it therefore could be calculated by multiplying the volume fraction of each ingredient by an appropriate conductivity and adding these products to the thermal conductivity of gum vulcanisate. Although it was assumed that a large variation in filler dispersion might have a measurable effect on the thermal conductivity of a compound but Sperberg, Harison, and Svetlik<sup>(91)</sup> have proved this assumption to be negligible.

A large dependence of conductivity on loading of carbon black was reported by Kainradl.<sup>(92)</sup> He concluded that thermal conductivity of rubber compound increased almost linearly with black content in the range of 10-50 phr black. Likewise, a similar conclusion was also obtained from Kong *et al.*<sup>(93)</sup> They carried out an experiment based on NR and SBR with various loadings of carbon black (N330). Experimental results clearly showed that thermal conductivity increased linearly with black loading (as shown in Figure 2.17) and, therefore, the mathematical relations between thermal conductivity and carbon black loading were introduced as;

$$k(w) = k(0) + 0.32w \quad \text{----- (2.79)}$$

$$k(\Phi) = k(0) + 0.4\Phi_f \quad \text{----- (2.80)}$$

where  $w$  is the weight fraction and  $\Phi_f$  is the volume fraction of carbon black. A list of thermal conductivities of various gum vulcanisates is given in Table 2.2.

Apart from carbon black loading, carbon black structure seems to have an influence on the thermal conductivity of rubber as well. Sircar and Wells<sup>(94)</sup> studied the effect of carbon black structure on thermal conductivity of NR and found that higher carbon black structure gives higher value of thermal conductivity. However, the degree of change in

thermal conductivity as a function of carbon black structure is small and is not straight forward.

Table 2.2 Thermal conductivities of gum vulcanisates<sup>(85)</sup>

Gum vulcanisates	k (X10 <sup>4</sup> ), W/m.K	Temperature, °C
Silicone rubber	1758.1	25
Butyl rubber(Enjay365)	1297.7	20
Butyl rubber(Enjay365)	1130.2	90
NBR(Perbunan N2810)	2051.1	20
NBR(Perbunan N2810)	1758.1	90
SBR(Buna Huls 152)	1925.6	20
SBR(Buna Huls 152)	1674.4	90
SBR	1758.1	30
Polybutadiene(SKB-50)	1632.5	90
NR <sup>a</sup>	1465.1	30
cis-Polybutadiene <sup>a</sup>	1674.4	30

<sup>a</sup> Vulcanised with 2 phr. dicumyl peroxide

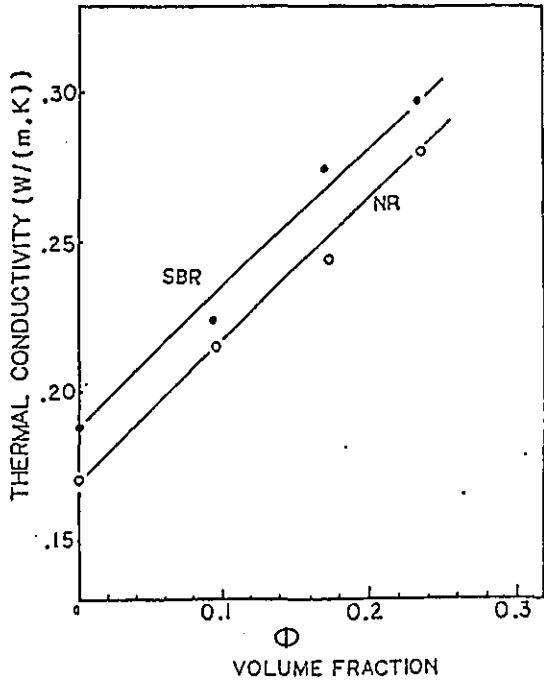


Figure 2.17 Thermal conductivity of NR and SBR filled with various amount of carbon black (N330)<sup>(93)</sup>

#### 2.4.2.2 Thermal diffusivity ( $\alpha$ )

Thermal diffusivity can be conveniently determined by observing temperature change as a function of time for simple geometrical shapes under heating condition.<sup>(85,95)</sup>

Alternatively, of course, if  $k$ ,  $\rho$  and  $C_p$  are known or separately determined,  $\alpha$  can be calculated from its definition as  $\alpha = k/\rho C_p$ . As specific heat is an additive property, it is generally convenient to calculate specific heats of rubber compounds than to measure them. Specific heat of a compound is given by

$$C_p = w_1 C_1 + w_2 C_2 + w_3 C_3 + \dots \quad \text{----- (2.81)}$$

where  $w_1$ ,  $w_2$  and  $w_3$  are weight fractions of the ingredients and  $C_1$ ,  $C_2$ , and  $C_3$  are their specific heats. Table 2.3 lists specific heats and densities of some polymers and compounding ingredients which may be useful in calculating the thermal diffusivity of rubber compounds. A value of 0.5 can usually be assumed without applicable overall error for minor ingredients such as organic accelerators, antioxidants, and softeners, if their actual values are not known.

In general, for rubber compound above the glass transition,  $\alpha$  tends to decrease slightly with increasing temperature. This is attributed to an increase of specific heat as temperature increases.<sup>(89,96-97)</sup> However, some authors<sup>(98)</sup> stated that there is no significant change in thermal diffusivity over the temperature range from room temperature up to 140°C.

#### 2.4.2.3 Heat transfer coefficient

Heat transfer coefficient is not a material property of rubber and depends upon geometrical factors, fluid velocity, surface roughness, temperature gradient, wetting, and a radiation component depending on surface emissivity.

**Table 2.3** Specific heat and density of rubbers and some mixing ingredients<sup>(85)</sup>

	Specific heat, J/g.K	Density, g/cm <sup>3</sup>
NR	1.88	0.92
Polybutadiene (emulsion)	1.97	0.892
SBR(25.5%bound styrene)	1.88	0.933
NBR(39% bound AN)	1.97	0.996
Butyl rubber	1.94	0.92
Neoprene	2.18	1.229
Carbon black	0.85	1.82
Magnesium oxide	1.00	3.31
Zinc oxide	0.52	5.63
Stearic acid	1.67	0.85
Extender oils	1.88	~0.94
Sulphur	0.72	2.03

In heating and cooling of rubber in liquids or gases such as air or steam, the most appropriate heat transfer coefficient under particular circumstances is usually obtained from extensive compilation of such coefficients. However, if precise values are required, it is necessary to determine heat transfer coefficient experimentally, under the exact conditions. It should be borne in mind that such determinations inevitably require exact measurements of the surface temperature of the rubber and great care must be taken to avoid errors due to heat conduction along thermocouple wires. Approximate values of heat transfer coefficient for air flow parallel to a flat surface, generally useful for miscellaneous heat transfer calculations, are given in Table 2.4. The value of heat transfer coefficients of crude rubber and rubber filled with carbon black was also reported by Hahn<sup>(99)</sup> to be 6.70 W/m<sup>2</sup>.K with an air speed of 1.98 m/sec. In addition, Cuthbert<sup>(100)</sup> also revealed that the heat transfer coefficient of rubber articles taken from moulds, for normal cooling to room temperature, was approximately 11.355 W/m<sup>2</sup>.K.

Basically, solid surface films always introduce a barrier to heat flow between materials and, therefore, must be taken into account in most circumstances in which there is

**Table 2.4** Heat transfer coefficients for air flow parallel to flat surface<sup>(85)</sup>

Air speed, m/sec	Heat transfer coefficient ( <i>h</i> ), W/m <sup>2</sup> .K
0	6.245
1.5	11.355
3.0	17.032
4.5	22.709
6.0	28.386
7.5	34.0632

a surface contact between solid materials. The interface contact resistance depends upon the intimacy of contact of the surfaces. In general, if intimate contact between two surfaces is assured, the thermal resistance between the interface contact can be ignored.

#### 2.4.2.4 Emissivity

The ability of a surface to emit radiant heat is represented by its emissivity. Emissivity of rubber usually decreases with increasing temperature.<sup>(101)</sup> For radiant heat exchange of rubber with surroundings at temperature up to 100°-200°C, emissivity will almost certainly be in the range of about 0.95 to 0.80 regardless of whether the compound is white or black.<sup>(85)</sup>

## **CHAPTER 3**

### **PROJECT STRUCTURE AND METHODOLOGY**

#### **3.1 Introduction**

This research is primarily concerned with the application of FEA in predicting the effect of hysteresis on temperature rise of rubber components under dynamic test conditions. Throughout this work, the finite element programme used for numerical computations was NISA II (Numerically Integrated element for System Analysis), developed commercially by Engineering Mechanics Research Corporation (EMRC). To use the programme, material constants were required. Those defining elasticity were based on the theory of “constant true Young’s modulus with varying Poisson’s ratio”.<sup>(102)</sup> Consequently, this chapter is aimed not only to represent the schematic diagrams of the experimental work, but also to describe some fundamental aspects of NISA II finite element programme as well as the basic principle of the above theory.

#### **3.2 Project layout**

Basically, the application of FEA in rubber field contains three distinct stages. The first stage deals with the characterisation of material behaviour required for the subsequent finite element analysis. The second stage is concerned with model simulation and analysis of the problems of interest. This stage involves model creation, specification of boundary conditions and material data, numerical computations as well as interpretation of finite element results. In the final stage, it is essential to carry out experiments and comparisons between experimental results and finite element predictions should be made. Thus, in summary, the project work can be divided into three main sections, as shown below.

**Section I : Preliminary determinations of material data.**  
**(Chapter 4)**

The material data include Mooney-Rivlin material constants, hysteresis factor ( $\tan \delta$ ) and heat transfer coefficients. Figure 3.1 shows the schematic diagram of work plan for the preliminary determinations.

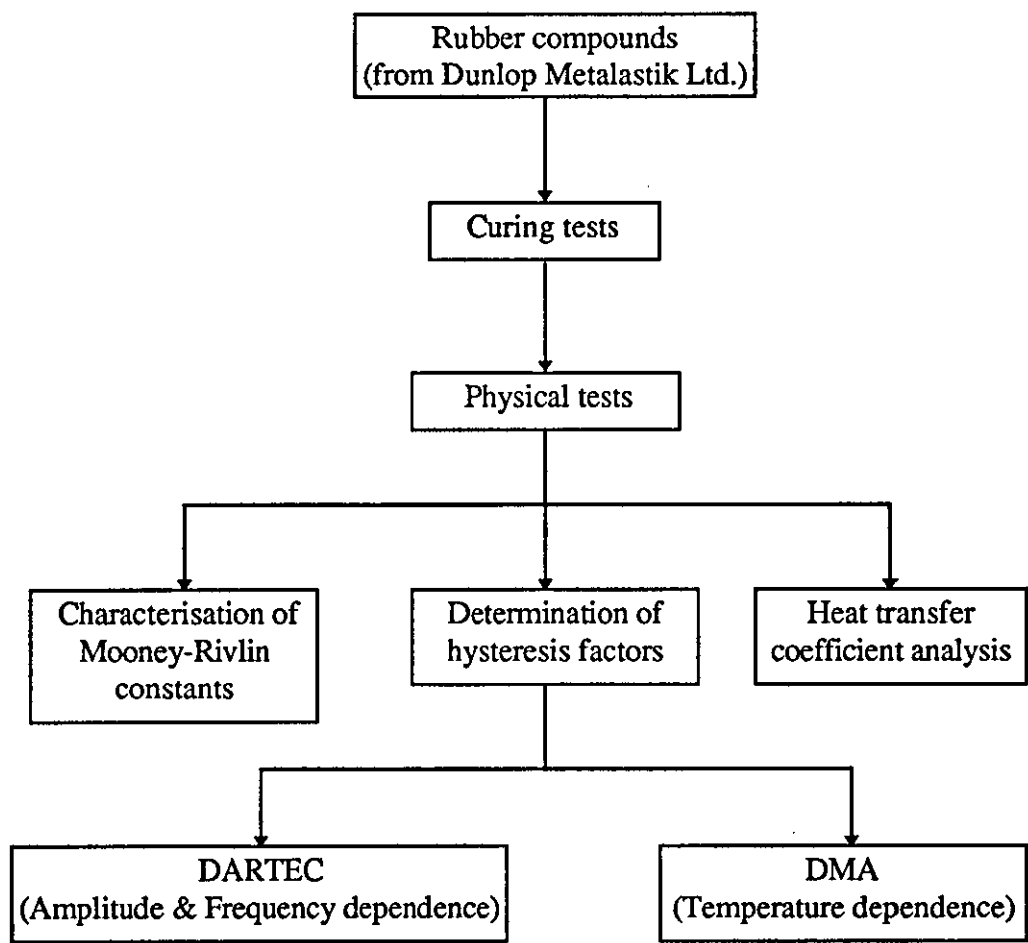


*Figure 3.1* Schematic diagram of work plan for preliminary determinations of material data

**Section II : Finite element analysis of temperature rise in rubber components.**  
**(Chapter 5)**

Engineering components chosen for this study were cylindrical anti-vibration mountings and a Chevron spring. The effects of service conditions (strain amplitude and frequency) on the internal temperature rise were studied. In addition, for anti-vibration mountings, the effects of geometric factor and deformation mode were also included. The entire FEA procedure is schematically summarised as shown in Figure 3.2, including the material data requirements (in the parentheses) for each step.

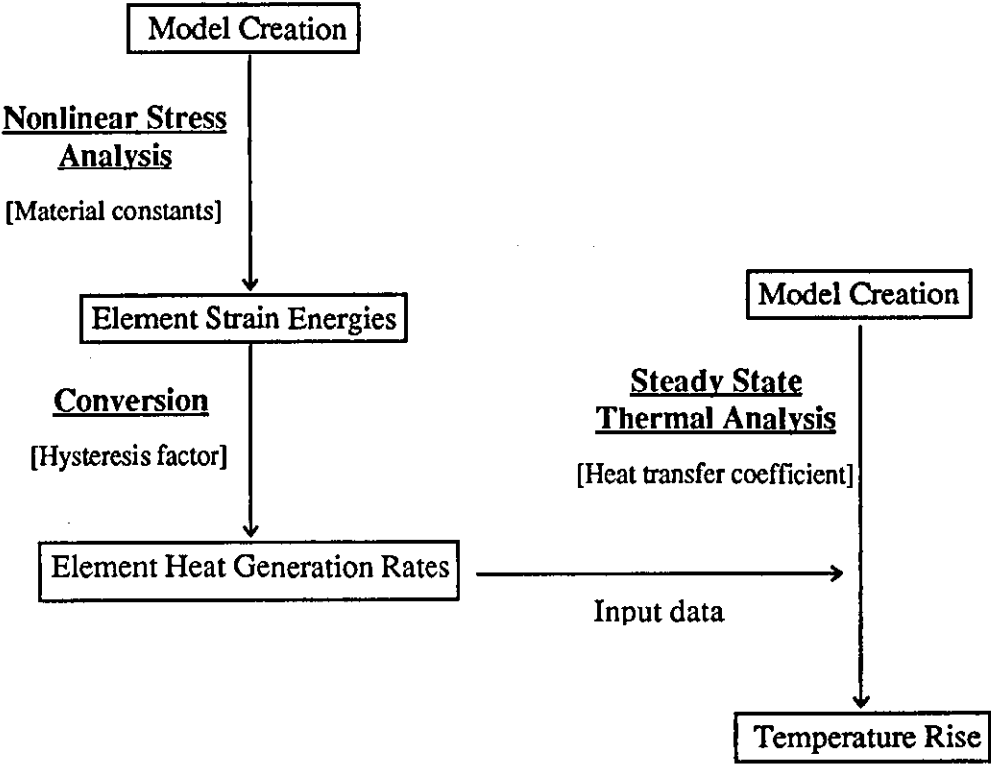


Figure 3.2 Schematic diagram of the entire FEA procedure



### **Section III : Evaluation of FEA results.**

#### **(Chapter 6)**

To gain confidence in the prediction values obtained from Section II, temperature measurements of the rubber components subjected to various test conditions were carried out and comparisons between the experimental results and the FE predictions were made. All dynamic tests of rubber components in this section were undertaken at Dunlop Metalastik Ltd, Leicester, England. Figure 3.3 summarises the work plan for this section.

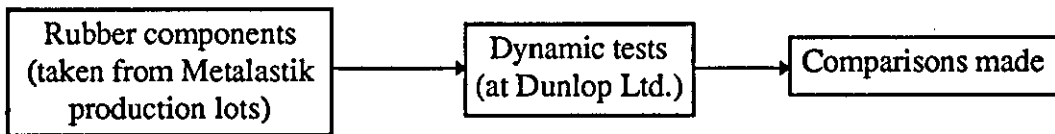


*Figure 3.3* Work plan for evaluation of FEA results

### **3.3 NISA II**

#### **3.3.1 Introduction**

NISA II is a general purpose finite element analysis programme, developed particularly for structural and heat transfer analysis. A wide range of analysis capabilities are available including:

- Linear static analysis.
- Nonlinear static analysis.
- Steady state and transient heat transfer analysis.
- Eigenvalue analysis.
- Buckling analysis.
- Modal dynamic analysis including transient dynamic, random vibration, frequency response and shock spectrum analysis.

### 3.3.2 NISA Pre- and Post- processors

NISA II is interfaced directly with a 3-D interactive colour graphics finite element pre- and post- processing programme, called DISPLAY.<sup>(103)</sup> This means that DISPLAY can write a file containing all the model and analysis directives required in a format acceptable to NISA II as well as read an output file containing the analysis results. In addition, DISPLAY can read or write a neutral file (or ASCII file) containing the model data in a well documented format which can be used by third party software or a user's own software to exchange information with DISPLAY.

#### ◆ Pre-processing

In the first step of finite element analysis, it is necessary to create a geometrical model of the main body and, then, discretize this body into a mesh of nodes and elements. The pre-processing module in DISPLAY has been introduced for this purpose. It allows a user to create the FE model which is ready for calculations. This FE model usually consists of a mathematical description of the boundary and interior of the body. To achieve this, DISPLAY provides facilities to specify locations in space (called GRIDS), straight or curved line segments (called LINES), surfaces (called PATCHES) and solids (called HYPERPATCHES). All the above are referred to as geometric entities. In general, the pre-processor in DISPLAY provides a large number of operations for the generation and modification (such as translation, rotation, copying, mirror imaging, etc.) of geometric entities.

To create a mesh for the body (meshing), there are also a variety of operations available in DISPLAY to accomplish FE generation. Meshing can be done either manually on each geometric entity or automatically by the automatic meshing capabilities of DISPLAY. It is also possible to create a FE model by using a combination of the two processes. The boundary conditions of the model (loads, constraints, etc.) can be applied easily with the auxiliary operations in DISPLAY. In addition, some sophisticated checks for distortion,

warping, skewness, etc. of elements, including potential discontinuities in the model, can be achieved with this powerful pre-processor.

In addition to standard view, different model orientations are available to let the user obtain the most informative views. The model can be displayed in different plotting modes to obtain the maximum graphical information. Some highlights of the NISA pre-processing capabilities are given below:

- CAD/CAM interface, directly from a geometry data base or through the IGES format.
- 3-D geometric modelling, including points, lines, arcs, curves, surfaces and solids as well as surface intersections.
- Geometric transformations, including translation, rotation, scaling, mirror imaging and dragging a curve along an arbitrary 3-D path.
- 3-D interactive finite element mesh generation including automatic node and element generation.
- Merging separate models into a larger one.
- Definition of element attributes including material and geometric properties.
- Specification of loading and boundary conditions.
- Extensive model editing capabilities.
- Extensive plotting options.
- Model checking including calculation of element areas, volume and distortion index.
- Complete NISA data deck generation.

#### ◆ Post-processing

Graphical representation and manipulation of the results may be performed interactively using the DISPLAY post-processing module. The major capabilities of the post-processing module are listed below:

- Deformed geometry plots, separate or superimposed on undeformed geometry.
- Contour plots of displacements, stresses, strains, temperatures and etc. on the original or deformed geometry.

- Contour plots of cut sections for 3-D models.
- XY history plots for various output quantities (especially useful for transient heat transfer analysis, where X is time).
- Animated deformed shapes.
- Deformed history plots for nonlinear static analysis.

### 3.3.3 Analysis types

#### ♦ Linear static analysis (STATIC)

Linear static analysis deals with the linear behaviour of elastic structure under certain boundary conditions and statically applied loads. The analysis may involve the calculation of displacements, strains, stresses, element volume and energy in the structure. The basic equation for linear static analysis is derived from the principle of minimum potential energy and can be expressed mathematically by

$$[K] u = P$$

where  $[K]$  is the linear stiffness matrix of the structure,  $u$  is the nodal displacement vector and  $P$  is the load vector.

#### ♦ Nonlinear static analysis (NLSTATIC)

Nonlinear static analysis is concerned primarily with the nonlinear behaviour of structures under static loading. There are two types of nonlinearity commonly found in real life problems. These are material and geometric nonlinearities.

Material nonlinearity arises from the nonlinear behaviour of stress-strain relation. Applications for material nonlinearity are normally encountered in viscoelastic and elastoplastic problems. Three types of material nonlinear behaviour are accommodated in the programme.<sup>(104)</sup> These are (i) the elastoplastic material behaviour, (ii) creep model

and (iii) the hyperelastic or rubber-like material models. For hyperelastic material models, various forms of strain energy functions with finite compressibility or near incompressibility behaviour are available.

The geometric nonlinearity is ascribed to large-deflection problems in which the deformed configuration must be involved in the analysis calculation. In this case, the classical theory of infinitesimal strains does not hold, and the strains are obtained from the displacements via a nonlinear differential operator. Applications for geometric nonlinearity are generally found in problems with large deformation, especially with rubber-like materials.

In geometric nonlinearity, or combined geometric and material nonlinearities, a distinction between the undeformed and the deformed configurations of the structure must be taken into account. In this case, the equilibrium or energy balance equations must be applied to the deformed configuration. As a result, two stress-strain formulations have been introduced, depending on the chosen reference configuration to describe the deformation of the body. These formulations are known as the total and update Lagrangian formulations. The total Lagrangian formulation uses a fixed configuration (undeformed state) as a reference, while, in the updated Lagrangian formulation, the reference configuration is always updated. It should be noted that both formulations are equivalent mathematically and, therefore, the same approximations should be obtained (except for round-off differences). The advantage of one formulation over one another is concerned with numerical efficiency, ease of handling particular nonlinear boundary conditions, etc.

#### ◆ Heat transfer analysis

Heat transfer analysis is concerned with the flow or transfer of heat energy as a result of temperature gradients. This phenomenon is caused by three different processes: conduction, convection and radiation. In NISA II, problems involving heat transfer due

to conduction with convection and radiation boundary conditions can be analysed. In addition, NISA II is also capable of analysing solidification and melting processes, provided that the assumptions of no volume change and no convection effect in the analysis are held.

Heat transfer analysis can be classified into two main categories: steady state heat transfer analysis (SHEAT) and transient heat transfer analysis (THEAT). The analysis in the former category deals with problems when material properties and boundary conditions are time independent. Conversely, if the material properties and/or the boundary conditions of the problem are time dependent, the transient heat transfer analysis must be performed to solve such problem.

In each category, both linear and nonlinear analysis may be performed. The problem will be analysed by a linear heat transfer analysis, if the following conditions are met:

- no radiation boundary conditions;
- no phase change, and
- material properties, convective coefficients, specific heat fluxes, and specified internal heat generations are temperature independent.

However, if the above of these conditions are not satisfied, a nonlinear heat transfer analysis is required to solve that particular problem.

### **3.3.4 Material models**

#### **♦ Linear elastic material model**

In this model, the stress-strain relation of the material is assumed to be constant, i.e., independent of the stress and strain states. The behaviour of ideal elastic solid obeys Hooke's law, thus, this model is alternatively known as the Hookean material model. This model requires elastic constants to characterise the constitutive relation. If the

elastic constants are directionally independent, the model is generally known as the “isotropic linear elastic model”. In this case, only two independent constants (Young’s modulus and Poisson’s ratio) are required to define the constitutive relations. On the other hand, if the material has different elastic constants in three mutually perpendicular directions at any point in the material, the model will be called “orthotropic linear elastic model” and more independent constants are required to define the constitutive relations.

#### ◆ Elastoplastic material model

The materials in this model are assumed to behave elastically up to a certain stress value (Yield point), after which a combined elastic and plastic behaviour takes place. Plasticity is characterised by an irreversible permanent straining that occurs in the material once the elastic stress limit is reached. NISA II provides various options of specifying the stress-strain relation of this model, for instance: elastic and perfectly plastic, elastic and linear hardening, etc.

#### ◆ Hyperelastic material model

A hyperelastic material is an elastic material of which its behaviour can be represented by a strain energy density function. This model normally represents rubber-like materials. For isotropic material, the strain energy function is expressed in terms of the strain invariants  $I_1$ ,  $I_2$  and  $I_3$ . Both finite compressibility and near incompressibility can be handled in NISA II. Even though rubbers are considered virtually incompressible, as evidenced by their very high bulk modulus compared to their shear modulus, the default value of the Poisson’s ratio ( $\nu = 0.499$ ) for near incompressibility is usually sufficient for analysis of problems under incompressibility assumption.

#### ◆ Heat transfer material models

Similar to the linear elastic material model, heat transfer material model can be divided into two main groups: isotropic and orthotropic material models. For isotropic material model, all thermal properties are assumed to be directionally independent. If this is the case, only one thermal conductivity value is required, coupled with some other applicable thermal properties such as specific heat and density. On the contrary, for orthotropic material model, the thermal properties are assumed to be directionally dependent and, therefore, three values of thermal conductivity are required, along with some other applicable thermal properties.

For both heat transfer material models, the material properties can be defined as constants or variables as a function of time or temperature.

#### 3.3.5 Solution techniques for nonlinear analysis

Application of FEA to problems involving linear elastic materials is straightforward, because the material parameters are constant and only one application of the solution process is required to solve a particular loading case. However, it is obvious that many phenomena found in real applications are nonlinear. Depending on the sources of nonlinearity, nonlinear problems can be divided into three categories as follows.<sup>(105)</sup>

- (i) Problems with material nonlinearity. This category is limited to problems in which the stresses are not linearly proportional to the strains, but in which only small displacements are considered.
- (ii) Problems with geometric nonlinearity. The problems in this category involve linear elastic material being subjected to a large deformation.
- (iii) Problems with a combination of material and geometric nonlinearities. The problems in this category involve nonlinear constitutive behaviour as well as relatively large deformation. The deformation of a rubber-like material is the obvious example of this category.



Since the fundamental methods of solving the problems under all three categories are the same, the solution techniques described in this section are based on the problems under the first category. In general, the solution of nonlinear problems by FEA is usually accomplished by one of the three basic techniques: incremental or stepwise method, iterative or Newton-Raphson methods and step-iterative or mixed methods.

#### 3.3.5.1 Incremental method

According to the incremental method, the solution of the nonlinear problems can be obtained by subdividing the applied load into many small partial loads or increments, then, calculating the displacements based on the linear equations. In other words, a fixed value of stiffness matrix  $[K]$  is assumed throughout each increment, however, different values of stiffness matrix may be applied in different load increments. The displacement increments are accumulated to give the total displacement at any stage of loading, and the incremental process is repeated until the total specified load has been reached. The accuracy of the incremental method is dependent upon the size of load increments. It is evident that the accuracy of the solution can be improved by taking smaller increments of load, however, an increase in accuracy is obtained with an expense of additional effort.

#### 3.3.5.2 Iterative method

The iterative method is a sequence of calculations in which the structure is fully loaded in each iteration. After each iteration, the portion of the total loading that is not balanced is calculated and used in the next step to compute an additional increment of the displacements. This process is performed repeatedly until equilibrium under the total load is approximated to some acceptable degree, or in other words, convergence of the solution is achieved.

Let  $\{Q_0\}$  and  $\{q_0\}$  be the initial loads and displacements. For the  $i^{\text{th}}$  cycle of the iteration process, the required load for an additional displacement is determined by

$$\{Q_i\} = \{Q\} - \{Q_{e,i-1}\} \quad \text{----- (3.1)}$$

where  $\{Q\}$  is the total load to be applied and  $\{Q_{e,i-1}\}$  is the load equilibrated after the previous step. The basic equation to compute an increment to the displacements during the  $i^{\text{th}}$  step then becomes

$$[K^{(i)}] \{\Delta q_i\} = \{Q_i\} \quad \text{----- (3.2)}$$

where  $[K]$  is the tangent stiffness matrix and the superscript (i) denotes a cycle of iteration. The total displacement after the  $i^{\text{th}}$  iteration is computed from

$$\{q_i\} = \{q_0\} + \sum_{j=1}^i \{\Delta q_j\} \quad \text{----- (3.3)}$$

Finally,  $\{Q_{e,i}\}$  is calculated as the load required to maintain the displacement  $\{q_i\}$ . The procedure is repeated until the increments of displacement or the unbalanced force become zero. That means  $\{\Delta q_i\}$  or  $\{Q_i\}$  becomes null or sufficiently close to null according to some pre-selected convergence tolerance.

During each increment, the tangent stiffness matrix maybe updated at each iteration (Newton-Raphson method), or kept constant in all iterations (modified Newton-Raphson method). Both conventional method and the modified Newton-Raphson methods are illustrated graphically in Figure 3.4.

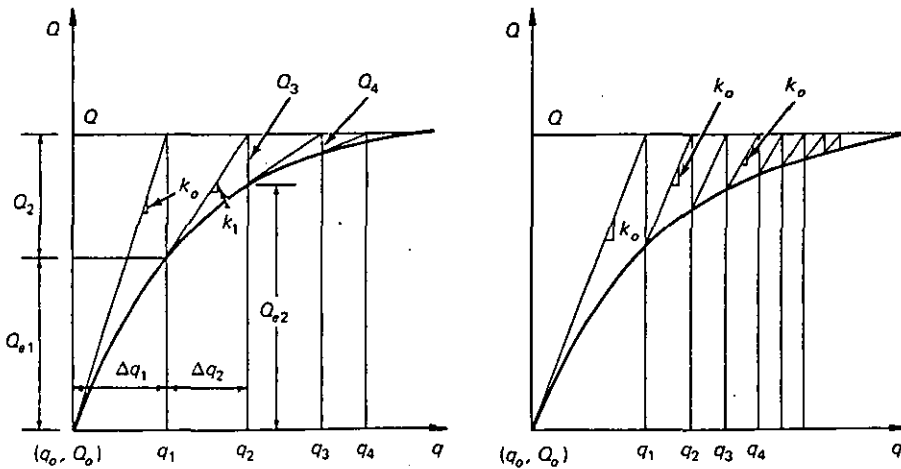


Figure 3.4 Newton-Raphson methods: (a) conventional and (b) modified method

Although the use of the modified Newton-Raphson method may be cost effective in some specific material nonlinearity applications, the utilisation of this method is not always successful in solving problems with general material and geometric nonlinearities.

### 3.3.5.3 Mixed procedures or step-iteration method

Basically, this method is a combination of the incremental and iterative schemes. In this method, the load is applied incrementally, and, in each increment, the iterative scheme is performed until specified convergence is achieved or maximum specified iterations are reached. It is reported that the method provides higher accuracy with more computational effort. A graphical representation of this method is given in Figure 3.5.

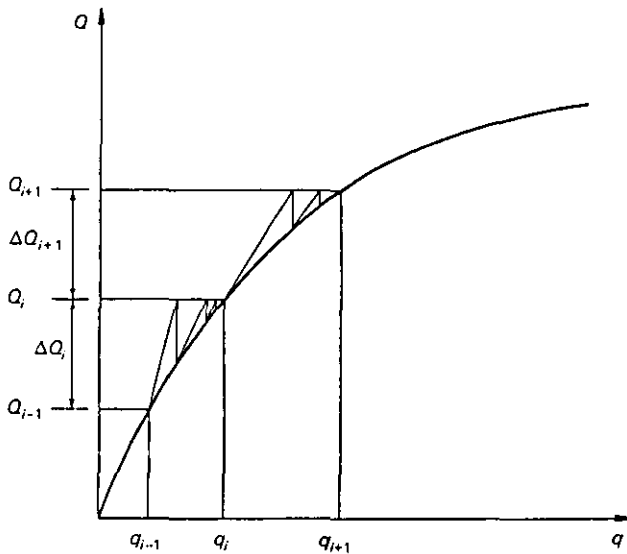


Figure 3.5 Step-iteration or mixed method

## 3.4 Characterisation of material constants via the theory of “constant true Young’s modulus with varying Poisson’s ratio”

In general, the material behaviour of rubbers is usually represented in terms of the strain energy density function, originally developed by Rivlin.<sup>(106)</sup> It is offered as an option in

most commercial FE programmes, such as ABAQUS, PATRAN, NISA II and MARC. For relatively low strains, the first two terms of Rivlin function (Mooney-Rivlin model) can provide a good prediction of rubber behaviour. However, for higher strains, more terms including power or cross product terms are needed.

Practically, FE programmes require the material constants  $C_{ij}$  as the input data. The material constants can be determined by the methods reviewed in Section 2.2. However, it is obvious that the material constants derived from uniaxial tensile data alone, using the conventional methods, are not sufficiently accurate to describe rubber behaviour in multiaxial deformations. Therefore, combined tests or biaxial tests are always recommended. Unfortunately, in this case, specially designed equipment is necessary.

As a consequence, to reduce the complexity and overcome the need for equipment for multiaxial data test, a new approach called “constant true Young’s modulus with varying Poisson’s ratio” has been introduced by Turner and Brennen<sup>(102)</sup> to generate the general biaxial tensile data from the uniaxial tensile data. This approach has been supported and further validated by other authors.<sup>(107-108)</sup>

### 3.4.1 General concept of the approach

It is a fact that, in uniaxial tension, the relation between true elastic stress and strain is linear over the strain range encountered in most engineering applications (say, up to 100% strain). A true elastic stress is defined as a ratio of the extension elastic force to the current cross-sectional area. From the assumption of incompressibility, where  $\lambda_1\lambda_2\lambda_3 = 1$ , the relationship between a true stress ( $t_i$ ) and an engineering stress ( $\sigma_i$ ) is given by

$$t_i = \frac{\sigma_i}{\lambda_j \lambda_k} = \sigma_i \lambda_i \quad \text{----- (3.4)}$$

where the subscripts refer to the directions of the principal stresses.

Based on the standard equations of elasticity at low strain (where the Young's modulus is assumed to be constant), the rubber's nonlinear multiaxial behaviour can be accommodated by considering the Poisson's ratio to be a variable, i.e., a function of the principal extension ratios. Thus, the stress-strain relations are given by

$$\epsilon_1 = \lambda_1 - 1 = (1/E) [t_1 - v(t_2 + t_3)] \quad \text{----- (3.5)}$$

$$\epsilon_2 = \lambda_2 - 1 = (1/E) [t_2 - v(t_3 + t_1)] \quad \text{----- (3.6)}$$

$$\epsilon_3 = \lambda_3 - 1 = (1/E) [t_3 - v(t_1 + t_2)] \quad \text{----- (3.7)}$$

where  $v$  is the Poisson's ratio.

For biaxial deformation, when  $t_3 = 0$ , rearrange Equation (3.6) and substitute into Equation (3.5), then

$$t_1 = \frac{E [(\lambda_1 - 1) + v (\lambda_2 - 1)]}{(1 - v^2)} \quad \text{----- (3.8)}$$

Similarly;

$$t_2 = \frac{E [(\lambda_2 - 1) + v (\lambda_1 - 1)]}{(1 - v^2)} \quad \text{----- (3.9)}$$

By substituting Equations (3.8) and (3.9) into Equation (3.7) and rearranging, the equation becomes

$$\lambda_3 - 1 = \frac{-v [(\lambda_1 - 1) + (\lambda_2 - 1)]}{(1 - v)} \quad \text{----- (3.10)}$$

By multiplying Equation (3.10) with  $-(1-v)$  and rearranging, the Poisson's ratio is then given by

$$v = \frac{1 - \lambda_3}{(\lambda_1 + \lambda_2 - \lambda_3 - 1)} \quad \text{----- (3.11)}$$

If incompressibility is assumed [ $\lambda_3 = (\lambda_1 \lambda_2)^{-1}$ ], the Poisson's ratio can then be defined as a function of  $\lambda_1$  and  $\lambda_2$  by

$$v = \frac{\lambda_1 \lambda_2 - 1}{\lambda_1 \lambda_2 (\lambda_1 + \lambda_2 - 1) - 1} \quad \text{----- (3.12)}$$

### 3.4.2 Conversion of true Young's modulus into Rivlin material constants

From the above approach, only a single material property (a constant true Young's modulus) is required to describe the rubber elastic behaviour. Unfortunately, most FE programmes dealing with nonlinear hyperelastic analyses only accept the material data input in terms of the Rivlin strain energy function or other similar functions such as Ogden, etc. As a consequence, the true Young's modulus must be converted into such a function.

With a given true Young's modulus, the varying Poisson's ratio theory can be used to calculate the true stresses for any biaxial state of deformation as defined by the two extension ratios  $\lambda_1$  and  $\lambda_2$ . If the combinations of the biaxial state are chosen carefully to cover the entire range of interested deformation, the constants of a Rivlin strain energy function can then be determined by a regression technique.

For this purpose, special software "elastic.exe", specifically written by Dr. P.S. Oubridge<sup>(109)</sup>, has been introduced. A basic principle of this programme is that, with a specified maximum strain, the programme generates a series of combinations of the two extension ratios  $\lambda_1$  and  $\lambda_2$ . Initially, six values of  $\lambda_1$  are selected with equi-spaced interval up to maximum strain, but excluding 0% strain ( $\lambda_1 = 1$ ). For each value of  $\lambda_1$ , the values of  $\lambda_2$  are selected in such a way that the numbers of  $\lambda_2$  are graduated from 5 at the lowest  $\lambda_1$  to 10 at the highest. Subsequently, the programme employs the true Young's modulus to calculate the principal true stresses for each of the 45 combinations of the extension ratios. Based on the stress-strain relation in any biaxial state (See Equation (3.13)), if the Rivlin strain energy function ( $W$ ) is partially differentiated with respect to the two strain invariants ( $I_1$  and  $I_2$ ) and substituted into the equation, the Rivlin material constants can then be obtained by the multiple regression technique.

$$t_i - t_j = 2 (\lambda_i^2 - \lambda_j^2) \left[ \frac{\partial W}{\partial I_1} + \lambda_k^2 \frac{\partial W}{\partial I_2} \right] \quad \text{----- (3.13)}$$

For instance, in the Mooney-Rivlin material model where  $W = C_{10} (I_1 - 3) + C_{01} (I_2 - 3)$ , the terms  $\frac{\partial W}{\partial I_1}$  and  $\frac{\partial W}{\partial I_2}$  will be equivalent to the material constants  $C_{10}$  and  $C_{01}$ ,

respectively. Equation (3.13) then becomes

$$t_i - t_j = 2 (\lambda_i^2 - \lambda_j^2) [ C_{10} + \lambda_k^2 C_{01} ] \quad \text{----- (3.14)}$$

where  $C_{10}$  and  $C_{01}$  are the Mooney-Rivlin constants.

## **CHAPTER 4**

### **PRELIMINARY DETERMINATIONS OF MATERIAL DATA**

#### **4.1 Introduction**

This chapter describes the determination of all material data governing the temperature rise of the rubber components. Of particular importance are the material constants required to define the elastic behaviour of the rubber compounds. Other parameters needed are thermal conductivity and the hysteresis factor ( $\tan \delta$ ). The latter parameter indicates the portion of strain energy to be converted into heat. Finally, to define the amount of heat dissipated to the surroundings, heat transfer coefficients for all constituent materials of the components to air must also be determined.

#### **4.2 Materials**

##### **♦ Rubber compounds**

Two different rubber compounds were used in this study. Both of them were supplied by Dunlop Metalastik Ltd., UK. and were coded as “Metalastik 19055” and “Metalastik 32053”. The compound recipes are not given as, for commercial reasons, they should be kept confidential. Nevertheless, brief information of each compound is given below.

- “Metalastik 19055” is used mainly in anti-vibration mountings. It is natural rubber reinforced with N539 black to obtain the required hardness of 55 IRHD (International Rubber Hardness Degree).
- “Metalastik 32053” is used mainly in Chevron springs. It is polyisoprene rubber reinforced with N660 black to obtain the required hardness of 53 IRHD.



- ◆ Mild steel (Bright Drawn Steel), supplied by A.H. Allen Steel Services (Derby) Ltd., UK. (for heat transfer coefficient analysis only).
- ◆ Aluminium (commercial grade), supplied by East Midland Alloys Ltd., UK. (for heat transfer analysis only).

### **4.3 Curing test**

An investigation of optimum curing time ( $t_{95}$ ) of the two compounds was undertaken using a Wallace Shawbury Precision Cure Analyser. The test conditions were set at 1.7 Hz, 0.24 strain and 150°C. For each compound, the test was repeated three times and the average value of  $t_{95}$  was used for the subsequent mouldings.

### **4.4 Determination of Mooney-Rivlin constants**

#### **4.4.1 Introduction**

Determination of Mooney-Rivlin constants from simple uniaxial tensile data via the theory of “constant true Young’s modulus with varying Poisson’s ratio” was undertaken successfully by using the software “elastic.exe”. As this programme requires the true Young’s modulus as an input, the following experimental procedure has been developed to fulfil this requirement.

#### **4.4.2 Methodology**

To determine the true Young’s modulus, an approximately 2 mm. thickness test sheet for each compound was prepared by using a compression mould at 150°C for a period of  $t_{95}$

(6 minutes for “Metalastik 19055” and 14 minutes for “Metalastik 32053”). The test specimens were then produced by means of a cutter with general dimensions as shown below. The orientation of the test pieces was chosen to follow the direction of milling.

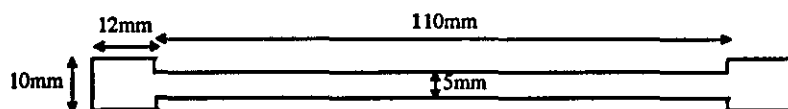


*Figure 4.1* The test piece dimensions for the near equilibrium stress-strain measurement.

Since both “Metalastik 19055” and “Metalastik 32053” rubber compounds are reinforced with carbon black, the viscoelastic effect (stress relaxation) is of great importance. As a consequence, to obtain near elastic deformation data, the effect of stress relaxation must be eliminated.<sup>(102)</sup> Therefore the following test procedure was used for this purpose. Initially, the test specimens were stretched by means of the Hounsfield tensile testing machine to a certain extension, say 10% strain, and were held at that extension for 600 seconds, allowing the rubber molecules to relax before the current force was recorded. Then, the same procedure was repeated at higher extensions (up to 80% strain).

From the experimental force-extension data, a relationship between engineering stress and strain was established. Based on Equation (3.4), the engineering stresses at any particular strain were then converted into the true stresses. Thereafter, a graphical correlation between true stress and strain was established and the true Young’s modulus of the vulcanisate was defined by the initial slope.

To investigate the temperature dependence of elastic properties, the test was also carried out at different temperatures ranging from ambient temperature up to 100°C.

As previously mentioned, conversion of the true Young's modulus into the Mooney-Rivlin constants was undertaken by the programme "elastic.exe". Apart from the true Young's modulus, the only other datum required for this programme was the maximum strain to be considered. Within this maximum strain, the programme would generate a sequence of combinations of the two extension ratios  $\lambda_1$  and  $\lambda_2$  and calculate the principal true stress for each combination created. Finally, multiple regression analysis was employed to obtain the Mooney-Rivlin elastic constants.

#### 4.4.3 Results and discussion

The plots of engineering stress versus strain for "Metalastik 19055" and "Metalastik 32053" are shown in Figures 4.2 and 4.3, respectively. The results clearly show that the relationship between engineering stress and strain of both compounds is markedly nonlinear.

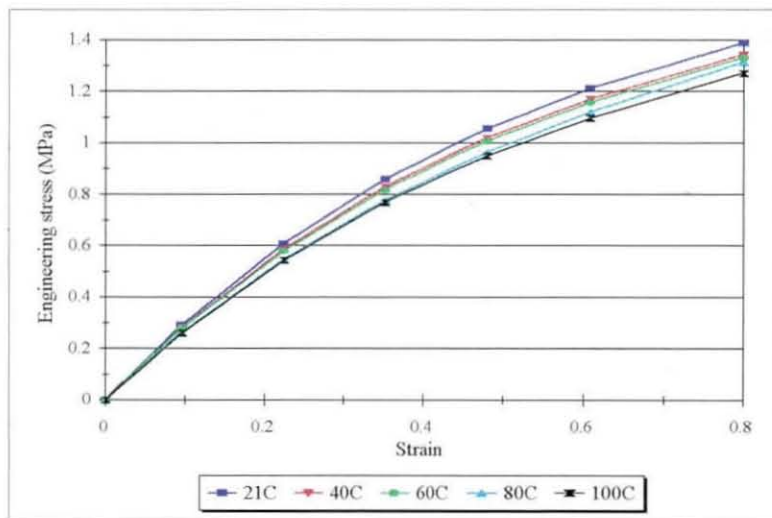


Figure 4.2 Engineering stress against strain for "Metalastik 19055"

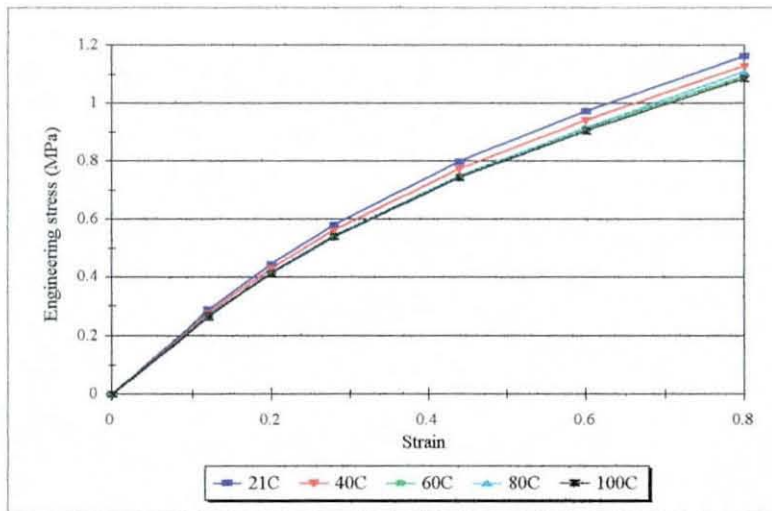


Figure 4.3 Engineering stress against strain for “Metalastik 32053”

On the contrary, as the ordinate axis is changed from engineering stress into true stress (See Figures 4.4 and 4.5), a perfectly linear relationship is obtained, at least up to 80% strain. Similar results were also obtained by Meinecke and Taft<sup>(72)</sup> who made measurements of relaxed stress under uniaxial extension on filled SBR and found a linear relationship up to 80% strain for the high loading.

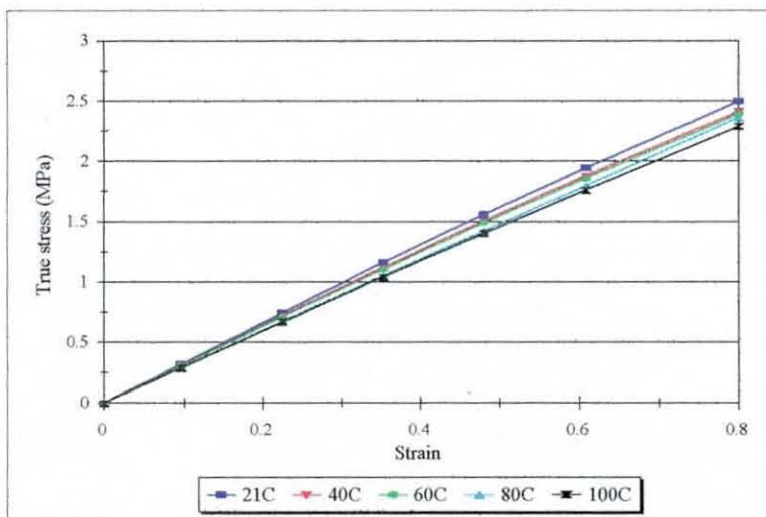


Figure 4.4 True stress against strain for “Metalastik 19055”

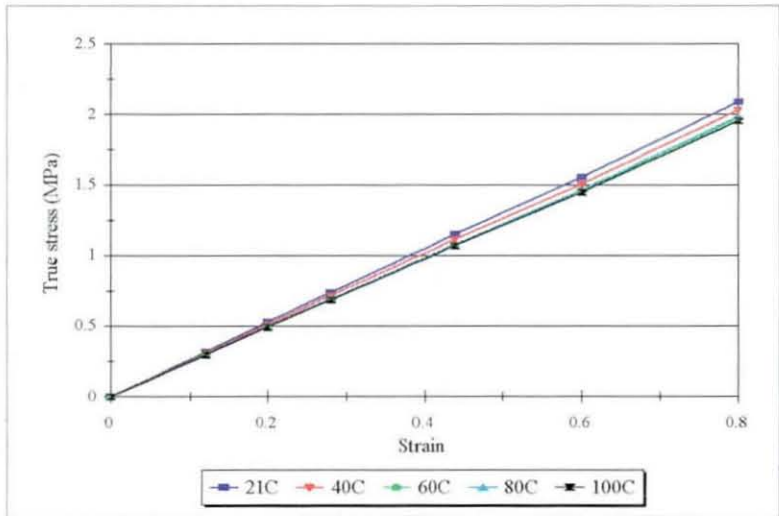


Figure 4.5 True stress against strain for “Metalastik 32053”

In addition, a linear relationship between true stress and strain for gum vulcanisates was also found by Tsuge *et al.*<sup>(110)</sup> This assures us that, at low strain amplitudes, only a single material parameter (the true Young’s modulus) is required to represent the elastic behaviour of the rubber compounds.

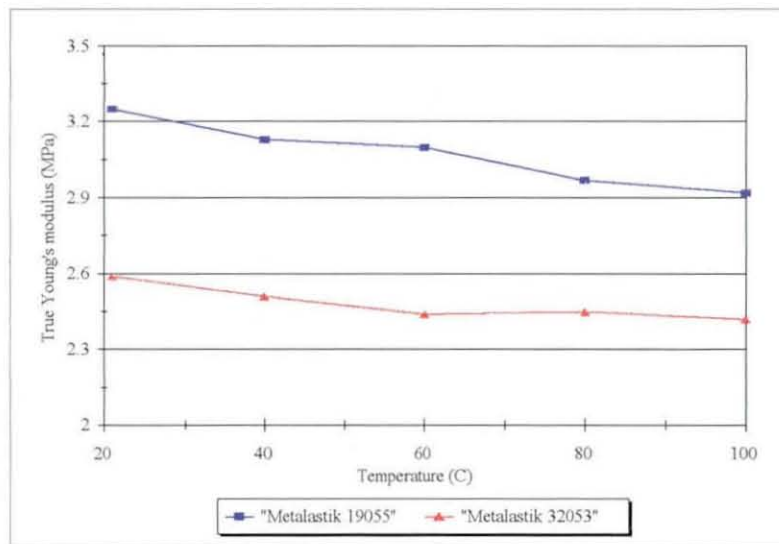


Figure 4.6 The effect of temperature on true Young’s modulus

Figure 4.6 illustrates the temperature dependence of the true Young's modulus. As can be seen, the true Young's modulus gradually decreases with increasing temperature. This is attributed to the increase in thermal mobility of rubber molecular chains with increased temperature. However, it can be observed that the reduction in modulus is not pronounced within the test temperature range.

Table 4.1 shows the results obtained from the programme "elastic.exe" with the specified maximum strain of 80%. Results clearly show the existence of correlation between temperature and the Mooney-Rivlin constants.

*Table 4.1* The Mooney-Rivlin elastic constants

Material	Temperature (°C)	Mooney-Rivlin constants	
		$C_{10}$	$C_{01}$
"Metalastik 19055"	21	0.42	0.11
	40	0.40	0.11
	60	0.40	0.10
	80	0.38	0.10
	100	0.37	0.10
"Metalastik 32053"	21	0.33	0.08
	40	0.32	0.07
	60	0.31	0.07
	80	0.31	0.07
	100	0.31	0.07

It is obvious that both  $C_{10}$  and  $C_{01}$  are inversely proportional to the temperature. This is likely due to the fact that both  $C_{10}$  and  $C_{01}$  are directly related to the true elastic (Young's) modulus as shown approximately, for simple extension, by  $E = 6 (C_{10} + C_{01})$ .<sup>(11)</sup> Therefore, as the temperature increases, the true Young's modulus decreases and, hence, the material constants also decrease. Nevertheless, it should be noted that the reduction of material constants with increased temperature is not really significant in

terms of quantitative considerations. As a consequence, the effect of temperature on material constants can be assumed to be negligible without serious error.

#### 4.4.4 Conclusions

The following conclusions can be drawn from the experimental results.

- i) Within the measured strain range, the uniaxial elastic behaviour of the rubber compounds is perfectly linear and can be represented by true Young's moduli.
- ii) The temperature dependence of both the true Young's modulus and the material constants is not pronounced, even though a slight reduction in their values with increasing temperature is observed.
- iii) Regardless of the temperature effect, the Mooney-Rivlin constants of both compounds used in this project are given below.

For "Metalastik 19055":  $C_{10} = 0.42 \text{ MPa}$  and  
 $C_{01} = 0.11 \text{ MPa}.$

For "Metalastik 32053":  $C_{10} = 0.33 \text{ MPa}$  and  
 $C_{01} = 0.08 \text{ MPa}.$

## **4.5 Determination of hysteresis factor**

### **4.5.1 Introduction**

Basically, there are several factors controlling the dynamic properties of rubber products, such as compound composition, processing factor and test conditions. However, only the influences of test conditions are of particular concern in this project. As, in most applications, rubber components are normally subjected to various strain amplitudes, frequencies and service temperatures and the hysteresis factor is, of course, dependent on these variables, therefore, the effects of these variables on the hysteresis factors of the two rubber compounds “Metalastik 19055” and “Metalastik 32053” have been thoroughly investigated in this section.

### **4.5.2 Methodology**

#### **♦ The effects of strain amplitude and frequency**

The investigation of the effects of strain amplitude and frequency on hysteresis factor was carried out by using a DARTEC ( $\pm 5$  kN) servo-hydraulic testing machine. The circular cross section test pieces with the dimensions shown in Figure 4.7 were prepared by bonding rubber to metal plates using a normal adhesion system. Firstly, the surfaces of the metal plates were cleaned with a fine steel wool to eliminate rust and dirt. Then, further surface treatment was achieved by using 1,1,1-trichloroethane to degrease and remove residual contamination. Finally, the bonding system, comprising of Chemlok 205 primer and Chemlok 220 covercoat (Durham Chemicals, UK.), was applied to the properly prepared surfaces with a drying period of 30 minutes between coats. After the surface preparation was complete, the rubber was then cured and bonded to the metal plates in a transfer mould at 150°C for a period of 16 minutes (for “Metalastik 19055”) and 22 minutes (for “Metalastik 32053”). Subsequently, the test pieces were tested at



three different frequencies; 0.1, 1 and 10 Hz. At each frequency, the test pieces were tested over a range of strain amplitudes, varying from 0.04 to 0.4. The ambient temperature was about 20°C and the tests were of short duration to avoid a significant temperature rise in the test pieces. Three test pieces were tested at each frequency and the average values of hysteresis factor were reported.

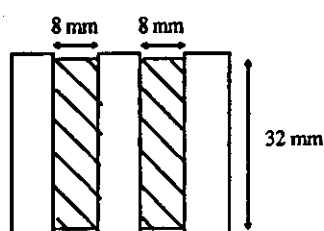


*Figure 4.7* The cross section view of the test specimen for the Dartec servo-hydraulic tester

#### ♦ The effect of temperature

An evaluation of the effect of temperature on hysteresis factor was undertaken successfully by using the Du Pont 928 DMA (Dynamic Mechanical Analyser). Specimens with approximate dimensions of 13X13X2 mm. were dynamically deformed in flexural mode with the oscillation amplitude of 1.00 mm. The frequency was kept constant at 1 Hz. The test temperature was increased continuously with a constant rate of 3°C/min, starting from ambient temperature up to 100°C. The value of hysteresis factor was then recorded at every 5°C interval.

### 4.5.3 Results and discussion

The effects of strain amplitude and frequency on hysteresis factor of both rubber compounds are graphically shown in Figures 4.8 and 4.9. Regardless of frequency range, results clearly show that the hysteresis factors of both compounds decrease slightly with increasing strain amplitude. However, within the strain amplitude ranging from 0.04 to

0.4, the decrease in hysteresis factor is insignificant. Consequently, for simplicity in modelling, it is assumed that hysteresis factor of these particular compounds is independent of strain amplitude and its value can be represented by a single mid-range value (See Figures 4.8 and 4.9).

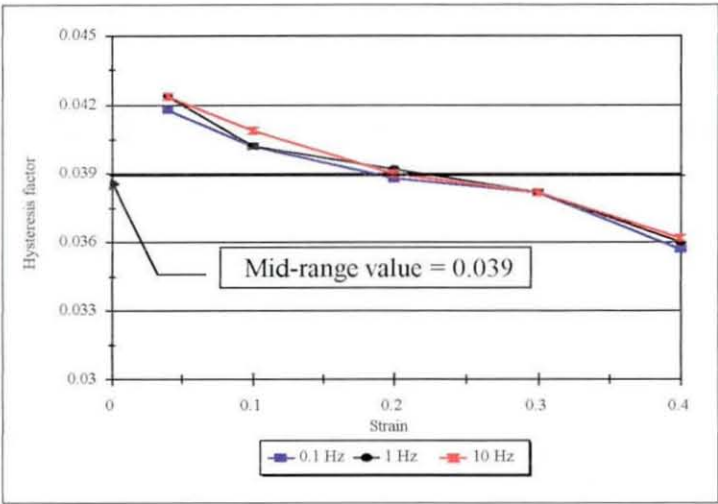


Figure 4.8 Hysteresis factor against strain amplitude of “Metalastik 19055”  
(Note the suppressed ordinate origin)

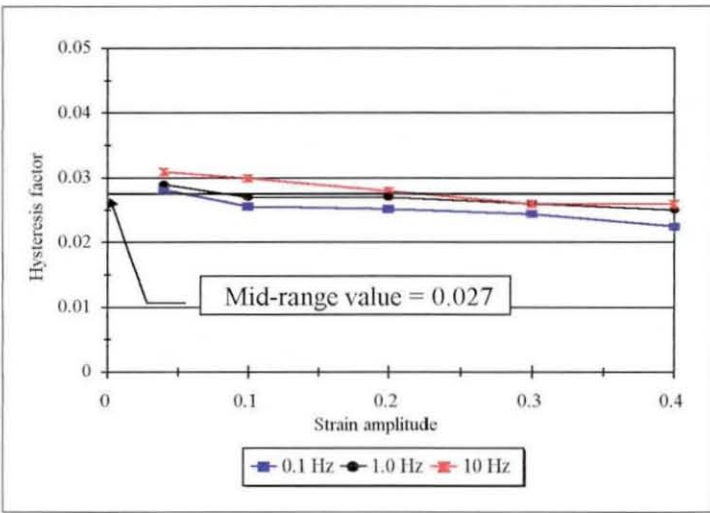


Figure 4.9 Hysteresis factor against strain amplitude of “Metalastik 32053”

When the effect of frequency is considered, it is apparent that frequency also has no significant effect on the hysteresis factor of both compounds, even though a slight increase in hysteresis factor with increased frequency can be observed.

Similarly, from DMA results (Figure 4.10), it can be seen that the effect of temperature on hysteresis factor is not pronounced, as the hysteresis factor of both compounds remains substantially constant over the test temperature range (25-95°C).

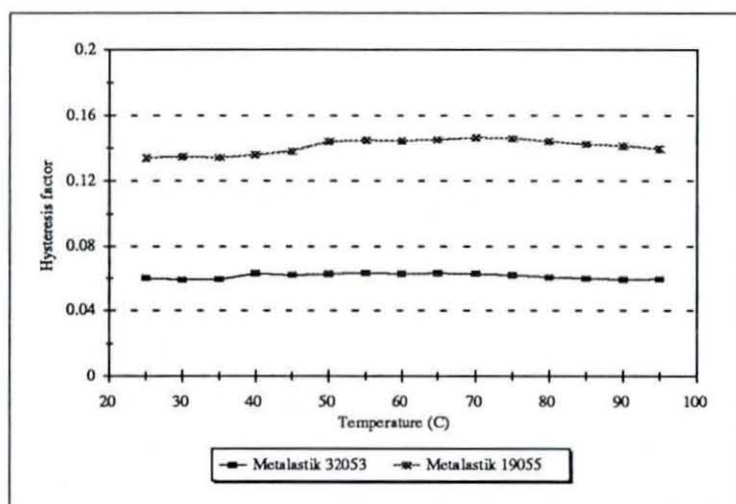


Figure 4.10 Hysteresis factor against temperature of two Metalastik compounds

The independence of hysteresis factor on both frequency and temperature can be explained below. In general, the effects of both frequency and temperature on hysteresis factor of a typical rubber vulcanisate containing carbon black are inversely interrelated and can be represented diagrammatically in Figure 4.11.<sup>(48)</sup> Within the experimental frequency range, the rubber molecular chains have adequate time to move in response to the applied stress. This means the rubber characteristic falls within the rubbery region where the frequency dependence is not pronounced. Moreover, it is evident that the presence of carbon black can also reduce the frequency dependence of the hysteresis factor.<sup>(112)</sup>

Likewise, at the test temperatures which are far above the glass transition temperatures ( $T_g$ ) of both natural and polyisoprene rubbers, the rubber molecules certainly possess the characteristics of the rubbery state as the molecular movement can take place very easily due to high thermal energy.

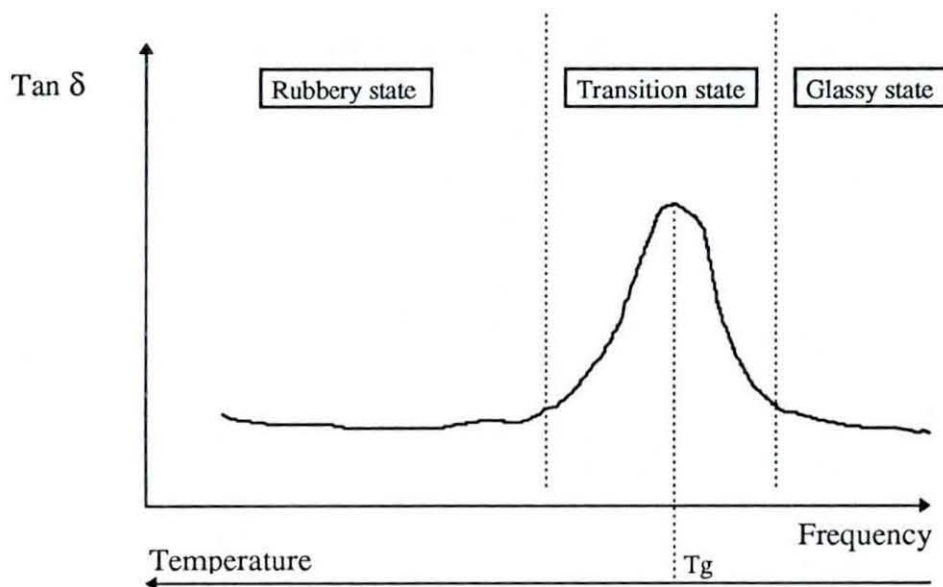


Figure 4.11 Typical hysteresis curve of CB-filled rubber vulcanisate

#### 4.5.4 Conclusions

Taken as a whole, it can be concluded that

- i) Regardless of the strain amplitude effect, the hysteresis factor of both compounds can be represented by a single value as shown below.

For “Metalastik 19055” : hysteresis factor = 0.039 or loss angle ( $\delta$ ) =  $2.23^\circ$

For “Metalastik 32053” : hysteresis factor = 0.027 or loss angle ( $\delta$ ) =  $1.55^\circ$

- ii) The hysteresis factors of both rubber compounds are found to be independent of both frequency and temperature within the tested ranges.

## **4.6 Heat transfer coefficient analysis**

### **4.6.1 Introduction**

Heat transfer coefficients of “Metalastik 19055”, “Metalastik 32053”, steel and aluminium to air were determined by using NISA finite element package based on results obtained experimentally by observing temperature changes at any point in the sample as a function of time.

### **4.6.2 Methodology**

#### **♦ Specimen preparation**

Three cylinder-shaped specimens for each material were prepared with the diameter and length of 26 and 46 mm, respectively. Vulcanisation of both rubber compounds was undertaken at 150°C for 30 minutes.

#### **♦ Experimental procedures**

Initially, one specimen for any material of interest was tested. A measurement of temperature change was carried out by creating a tiny hole into the specimen. Then, a fine (0.5 mm diameter) calibrated thermocouple wire was carefully inserted through the hole, ensuring that:

- (i) a good contact between thermocouple and material matrix was attained, and
- (ii) the exact position of the extreme of the thermocouple wire was known.

Thereafter, the assembly was brought to temperature equilibrium in an oven maintained at approximately 80°C and then suddenly brought out and hung in the air to cool down at a constant room temperature (18°C). The temperature readings were then recorded periodically for 1080 seconds and, finally, a graph of temperature reduction against time was created.



After recording the experimental data, a transient heat transfer analysis in NISA was performed to determine the value of heat transfer coefficient. According to the symmetric configuration, only a quarter of each specimen was modelled and analysed. The model was then subdivided into 276 axisymmetric eight-node quadrilateral elements as shown in Figure 4.12.

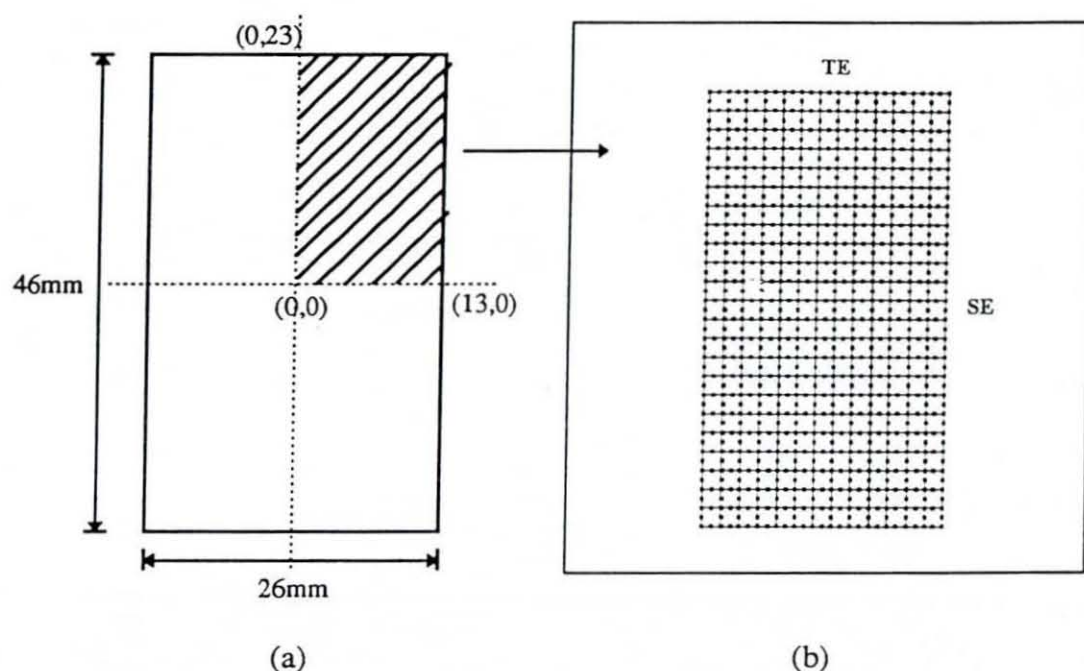


Figure 4.12 Geometry (a) and FE model (b) of a cylinder specimen for transient heat transfer analysis

The boundary conditions were applied as follows. The initial temperature of all nodes was set to be the same as the oven temperature. Likewise, the film temperatures at both side edge (SE) and top edge (TE) were defined by the room temperature. The material properties used for the analysis were given in Table 4.2.

Initially, one estimated value of heat transfer coefficient was applied to the element faces along the side edge and top edge. The transient thermal analysis was then performed to

Table 4.2 Material properties for thermal analysis

Material Property	Metalastik 19055*	Metalastik 32053*	Steel*	Aluminium**
Thermal conductivity (W/mm.K)	0.000225	0.000219	0.05	0.203
Specific heat (J/g.K)	1.975	1.995	0.460	0.90
Density (g/mm <sup>3</sup> )	0.00107	0.00106	0.0078	0.00271

\* Data supplied by Metalastik Ltd.

\*\* Data obtained from "Metallic materials"<sup>(113)</sup>

compute the temperature at any point in the model as a function of time. With the DISPLAY post-processor, a plot of computed temperature against time at a point in the model identical to the location of the thermocouple in the specimen was established. The curve was then compared to the experimental curve. Thereafter, the value of the heat transfer coefficient was adjusted to gain the best fit between the simulated and the experimental curves. This procedure yielded the best value of heat transfer coefficient for the specimen.

To check the validity of this value, the other two specimens for each material were tested with the same procedures, except that the thermocouple wire was inserted at different positions. The transient heat transfer analysis was then run by using the value of heat transfer coefficient previously obtained. Finally, the computer generated curves were compared to the experimental curves.

### 4.6.3 Results and discussion

The temperature reduction traces of "Metalastik 19055", "Metalastik 32053", steel and aluminium with various values of heat transfer coefficients are shown in Figures 4.13 to 4.16, respectively. Obviously, the results indicate that the method used herein is capable of estimating the value of heat transfer coefficient of materials with high accuracy as, when the right value of heat transfer coefficient is chosen, the computed curve fits very well with the experimental curve. It is also apparent that the temperature reduction traces

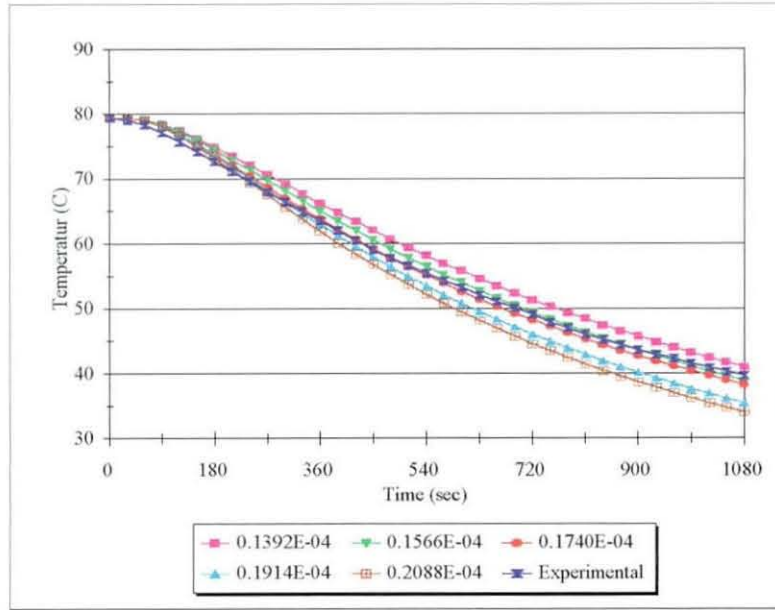


Figure 4.13 Temperature reduction traces of “Metalastik 19055” at position (5,10) with various values of heat transfer coefficient

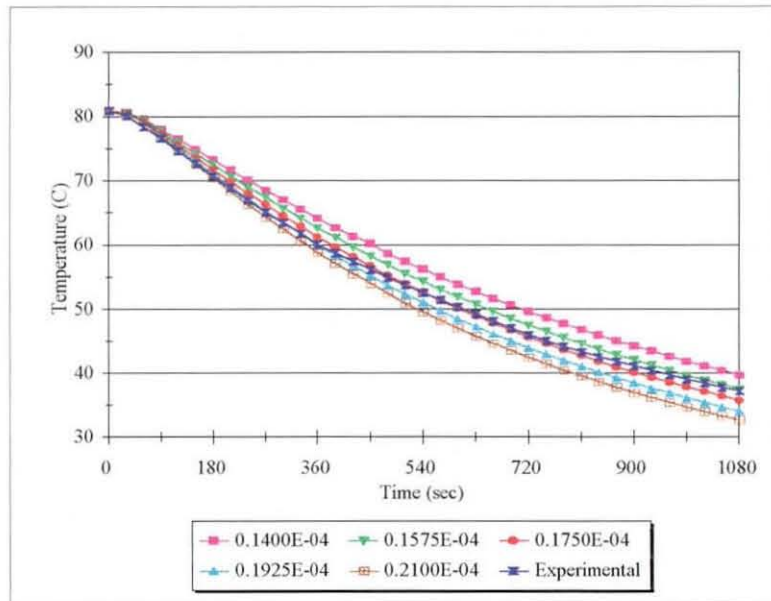


Figure 4.14 Temperature reduction traces of “Metalastik 32053” at position (8,10.5) with various values of heat transfer coefficient



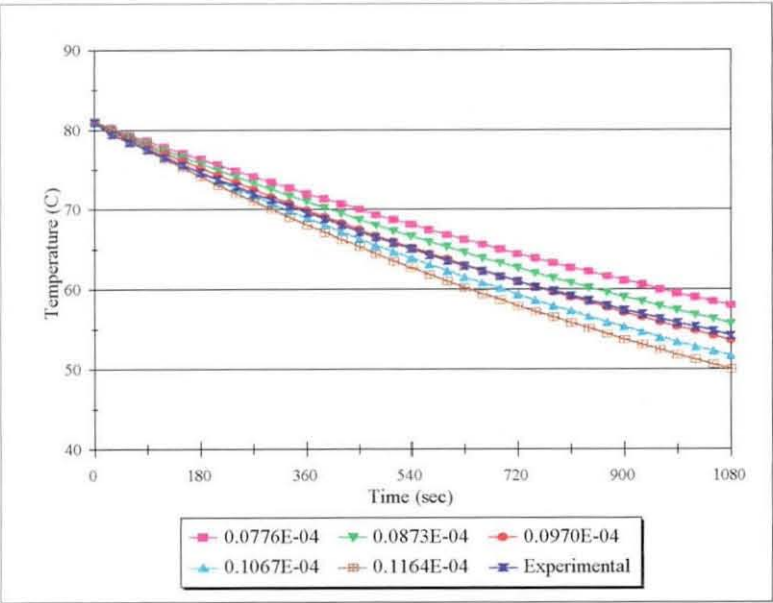


Figure 4.15 Temperature reduction traces of steel at position (8,5) with various values of heat transfer coefficient

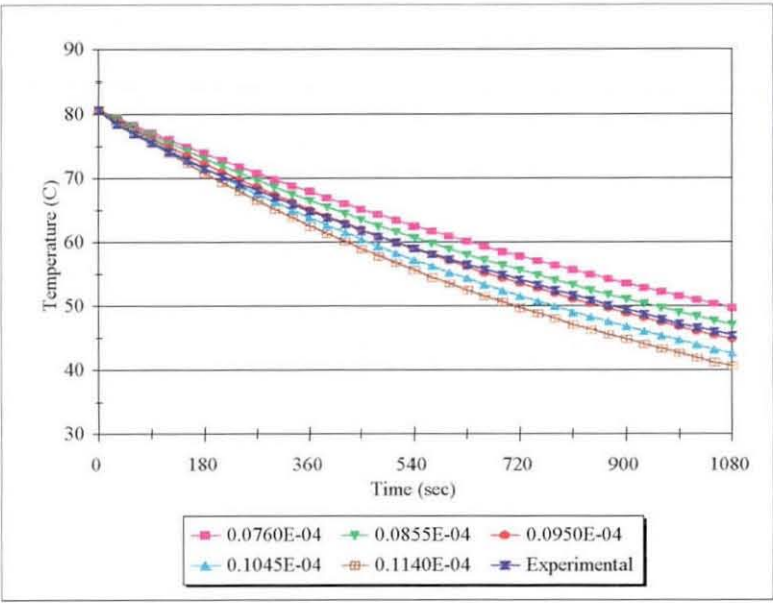


Figure 4.16 Temperature reduction traces of aluminium at position (9,15) with various values of heat transfer coefficient

are fairly sensitive to any changes in heat transfer coefficient. As can be seen, a slight change in heat transfer coefficient from the best value results in a noticeable deviation from the experimental curves. Table 4.3 represents the best values of heat transfer coefficient for each material.

Table 4.3 Heat transfer coefficients of materials

Material	Heat transfer coefficient (W/mm <sup>2</sup> .K)
“Metalastik 19055”	0.174E-04
“Metalastik 32053”	0.175E-04
Steel	0.097E-04
Aluminium	0.095E-04

To validate the best values of heat transfer coefficient obtained, the test was repeated at different positions by using the value of heat transfer coefficient shown in Table 4.3 for the transient thermal analysis. Figures 4.17 to 4.20 show the comparisons between the computed and experimental temperature traces for each material of interest at different positions.

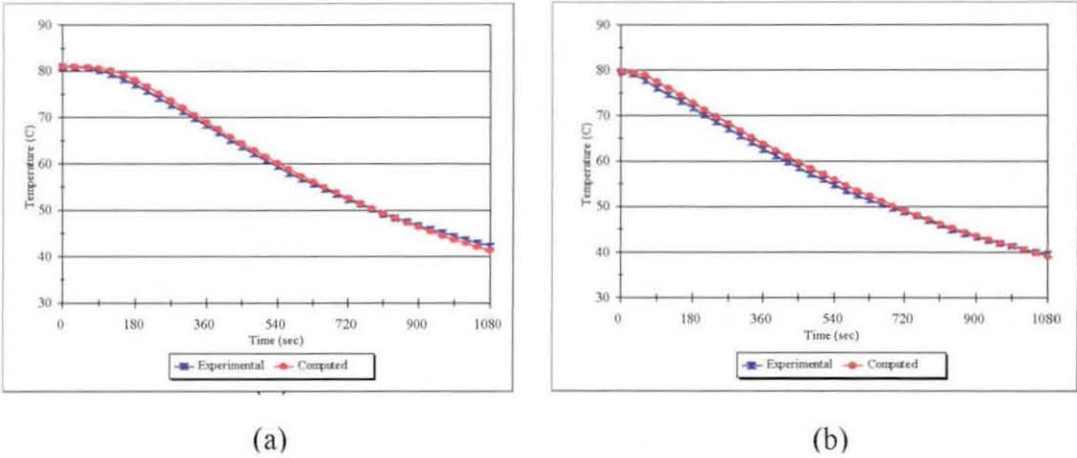
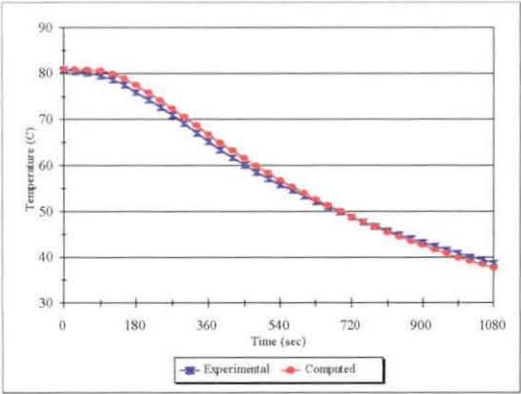
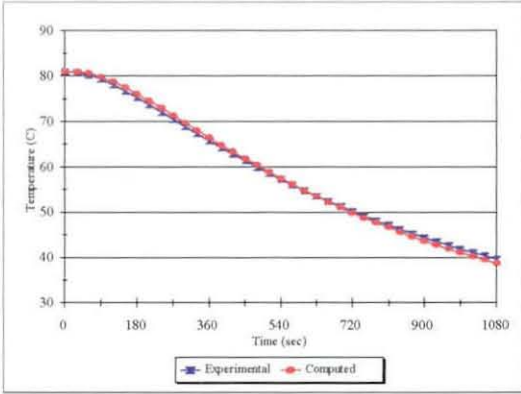


Figure 4.17 Temperature reduction traces of “Metalastik 19055” (a) at position (0,2) and (b) at position (6,0)

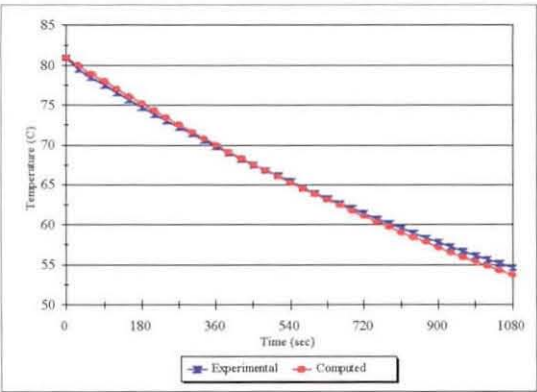


(a)

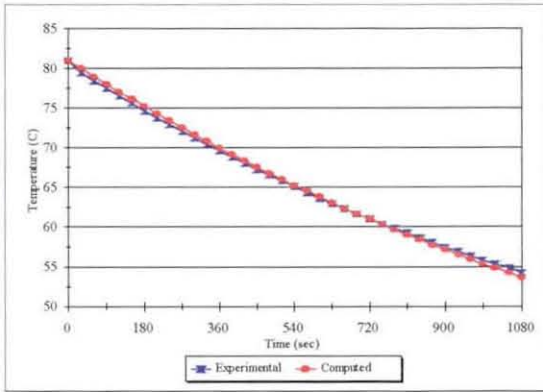


(b)

Figure 4.18 Temperature reduction traces of “Metalastik 32053” (a) at position (1,12.5) and (b) at position (5,6.5)

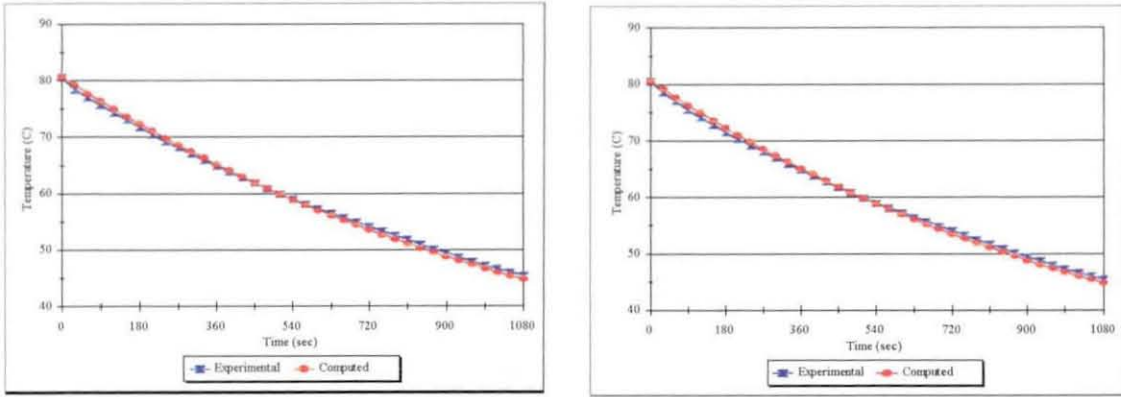


(a)



(b)

Figure 4.19 Temperature reduction traces of steel (a) at position (0,3) and (b) at position (6,10)



(a)

(b)

*Figure 4.20* Temperature reduction traces of aluminium (a) at position (0,11) and (b) at position (6,5)

As can be seen, the computed results fit very well with the experimental results in any positions selected. In fact, these results confirm that the values of heat transfer coefficient obtained from this method are accurate and reliable. It is also observed that the values of heat transfer coefficient of the two rubber compounds are almost identical and, similarly, for those of the two metals. This is attributed to the fact that heat transfer coefficient is not a material specific but, on the contrary, it depends mainly on several factors, for instance, specimen shape, temperature gradient, surface emissivity, etc. In this case, the values of heat transfer coefficient of rubber compounds are almost double those of metals. This is possibly due to the effect of surface emissivity as all test specimens were in the same shape and subject to the same heat treatment. Clearly, an addition of carbon black into rubbers would bring the compounds closer to the classical black body from which more energy will be radiated (higher surface emissivity) compared to a glossy painted surface or a polished metal surface.

Even though the heat transfer coefficient will be dependent on geometry, for simplicity of FEA in this project, the effect of geometry on the heat transfer coefficient is disregarded as various component geometries were modelled and analysed. An error introduced by this disregard will be discussed later in Chapter 6.

#### **4.6.4 Conclusions**

In summary, results clearly show that

1. the method used herein is capable of measuring the heat transfer coefficient of materials with high accuracy. The values of heat transfer coefficient for each material of interest are given in Table 4.3.
2. heat transfer coefficient is not a material specific but mainly dependent on the surface appearance. A material with glossy, polished surface tends to have lower value of heat transfer coefficient, compared to that with a black, matted surface.

## CHAPTER 5

### MODELLING WORK

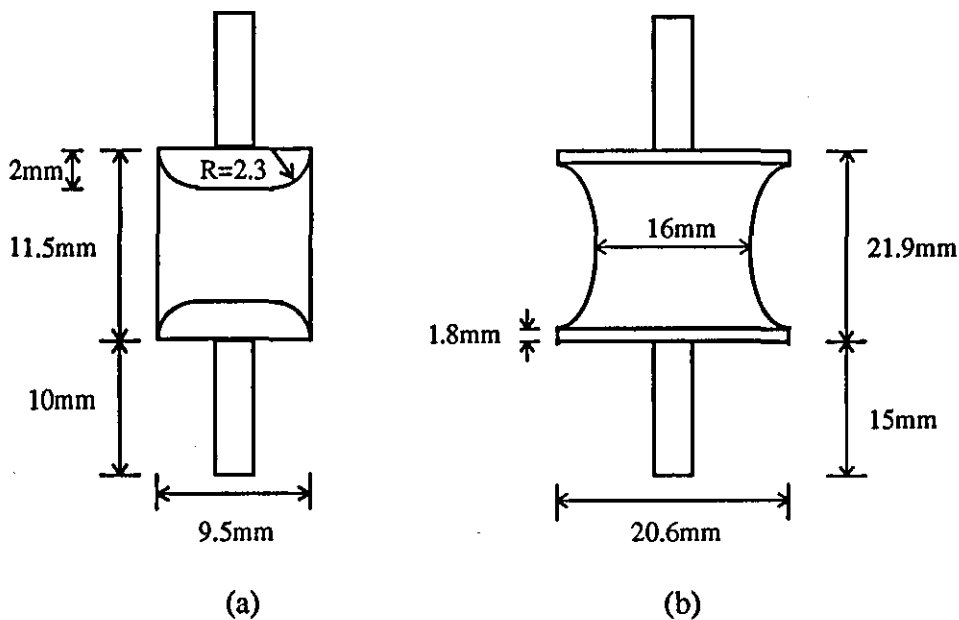
#### 5.1 Introduction

The prediction of the temperature rise of rubber components subjected to dynamic deformation was undertaken by means of Finite Element Analysis (FEA). Throughout this work, all finite element problems were modelled and solved numerically by the NISA<sup>(114)</sup> package installed into a PC 486/66 MHz.

#### 5.2 FEA of approximately cylindrical anti-vibration mountings

##### 5.2.1 Mounting geometry

Mountings with a wide variety of shapes and sizes are now commercially available to enable engineers to choose the appropriate design to protect instruments from vibration. In this study, three different sizes of mountings were selected from the "Metalastik Instrumountings Brochure"<sup>(115)</sup> and their geometries are displayed in Figure 5.1.



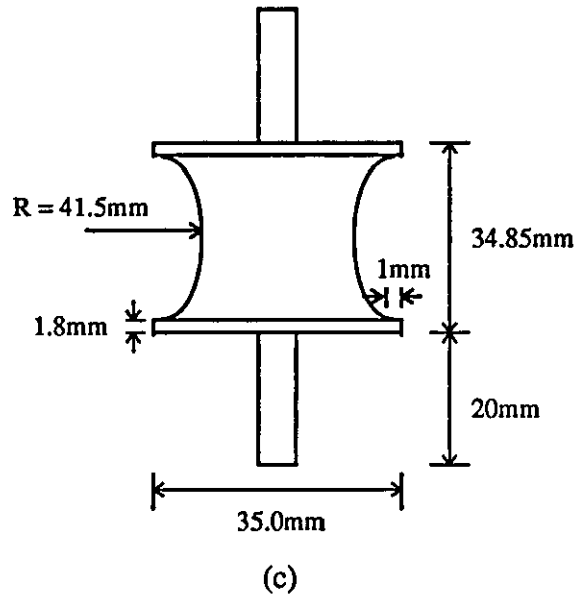


Figure 5.1 Geometries of (a) small, (b) medium and (c) large mountings

### 5.2.2 Rubber compound

The rubber compound considered in the modelling of rubber mountings was supplied by Metalastik and it was coded as “Metalastik 19055”. The compound recipe is not given herein as, for commercial reasons, it should be kept confidential. The mechanical properties of this compound were represented in terms of the Mooney-Rivlin hyperelastic material model. The two material constants used for the analysis, together with some other essential material data such as hysteresis factor and heat transfer coefficient, were determined using the procedures described in Chapter 4.

### 5.2.3 Problem description and experimental design

In a typical service environment, the mountings are normally subjected to either dynamic shear or axial deformation. Based on the deformation mode, the simulations of rubber mountings were of four kinds:

- (1) mountings subject to dynamic axial deformation without precompression;
- (2) mountings subject to dynamic axial deformation with 10% precompression;

- (3) mountings subject to dynamic shear deformation without precompression;  
and
- (4) mountings subject to dynamic shear deformation with 10% precompression.

For any kind of deformation, the performance of the mountings is strongly dependent on strain amplitude and frequency. Thus, the effects of these factors on temperature rise were of great interest in this project. To obtain a response equation relating the temperature rise to the two factors, an experimental design with 2 factors namely the central composite design<sup>(116)</sup> was introduced. In the design, it is preferable to define the factor levels in design units. The total design can be constructed as represented diagrammatically in Figure 5.2. According to this diagram, nine simulations were performed for each deformation mode. Details of the test conditions for these simulations are given in the subsequent sections.

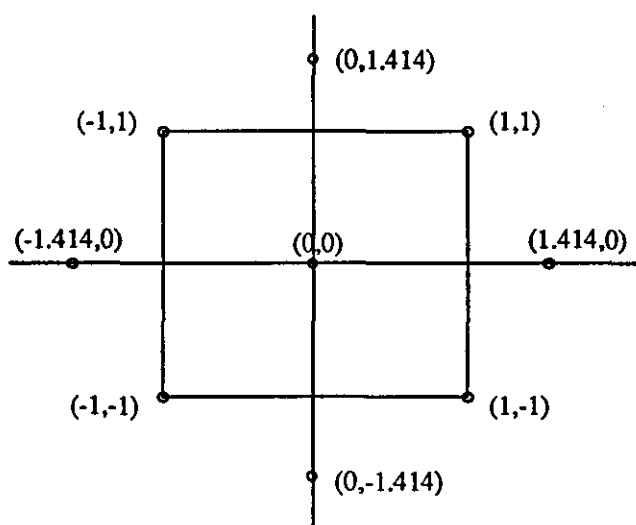


*Figure 5.2* The experimental design for 2 factors;-strain amplitude and frequency

#### 5.2.4 The FEA procedures

Basically, because of the complexity of the calculations, it is of great importance in FEA to make the number of unknowns as small as possible by taking advantages of symmetry



wherever applicable. However, a point to be borne in mind is that, to take the benefit from symmetry, both the geometry and the applied loading must be symmetrical.

The FEA procedures for the mountings described below are divided into two, based on the deformation mode because of the demands, or otherwise, of symmetry.

#### 5.2.4.1 Dynamic axial deformation.

When axial deformation is considered, the symmetrical requirements explained above can be met by 2-D axisymmetric modelling. As can be seen from Figure 5.3, symmetry considerations made it possible to model only a quarter of the domain (shaded area).

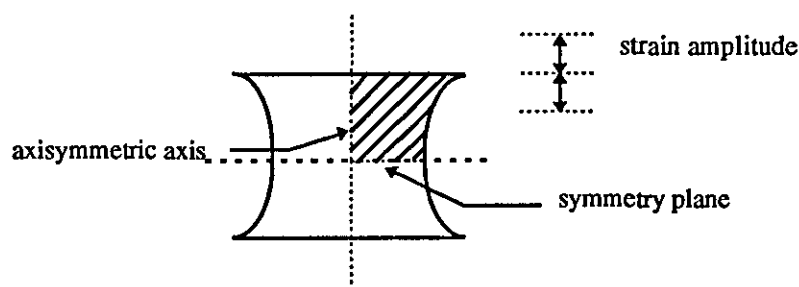


*Figure 5.3* 2-D axisymmetric modelling of rubber mountings

#### ♦ Dynamic axial deformation without precompression

By considering the mountings subject to 15% strain deformation at 40 Hz as an example, the FEA procedures can be described step by step as follows.

Step (1) The FE meshes for stress analysis were created and shown in Figures 5.4. Two-dimensional eight-node quadrilateral elements were chosen to represent these models. Only the rubber parts were modelled and analysed, since the metal parts were considered as a fully elastic material with a very

high Young's modulus value which would not distort or give any heat build-up under dynamic deformation.

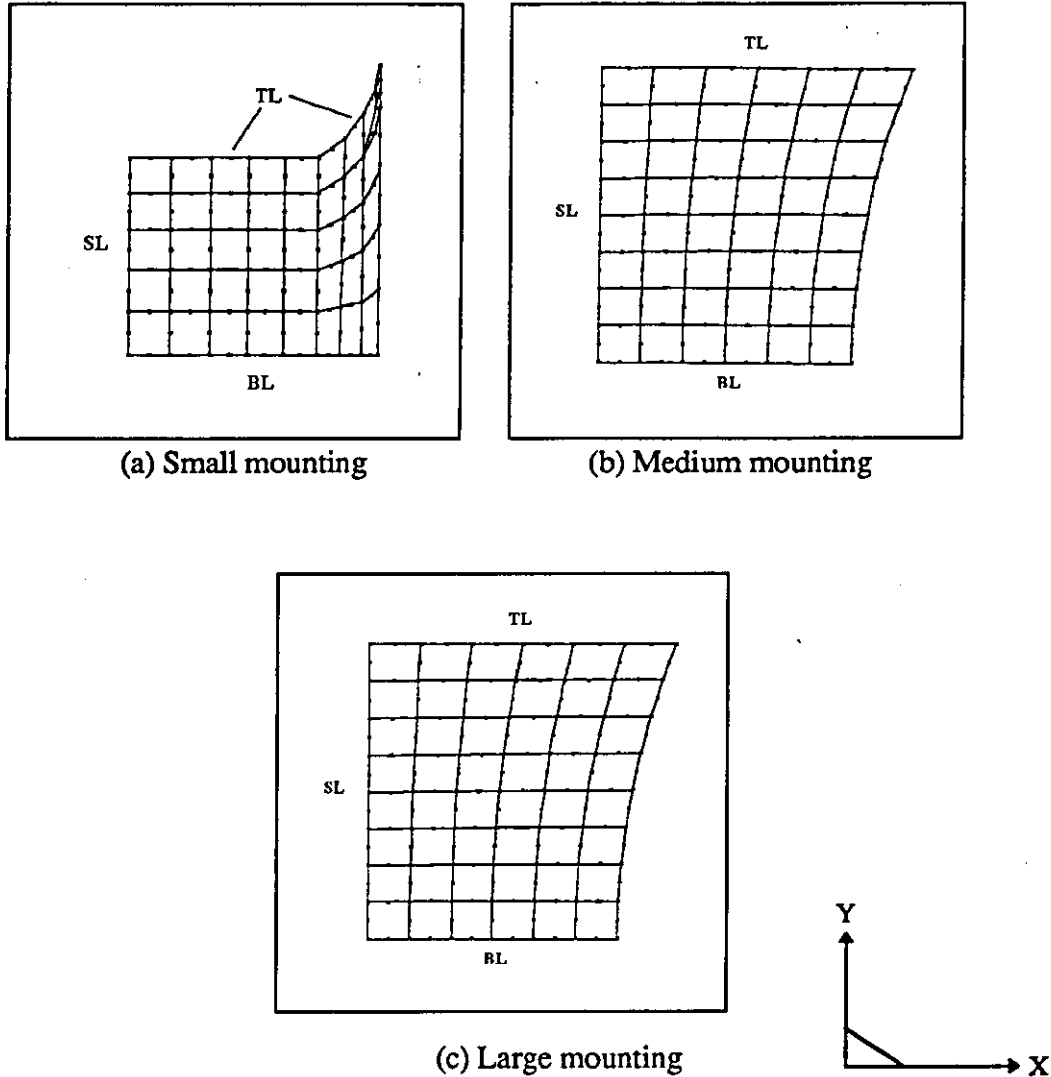


*Figure 5.4* FE meshes for stress analysis

**Step (2)** Since the mountings, in one cycle, were deformed in both extension and compression, two models per mounting were then created based on the deformation mode. For all models, the displacement boundary conditions were applied to ensure that all nodes along the bottom line (BL) were

restrained not to move in Y-direction, while all nodes along the symmetry line (SL) were restrained not to move in X-direction. As the rubber part was bonded to steel plate at the top line (TL), the steel plate constrained the movement of rubber at the interface. Consequently, while all nodes along this surface contact were specified to move either downwards (compression) or upwards (extension) to 15% strain, their movements along the X-direction were restricted.

Step (3) The hyperelastic Mooney-Rivlin material model was selected to define the material data. The two elastic constants were (See Chapter 4)

$$C_{10} = 0.42 \text{ MPa}$$

$$C_{01} = 0.11 \text{ MPa}$$

$$\text{and Poisson's ratio} = 0.499.$$

Step (4) The stress calculations of these models were then performed by means of nonlinear stress analysis. During the computation, the displacement was divided into, and applied in, 100 equal steps.

Step (5) After the nonlinear stress analysis, the element strain energies for each model were extracted from the output file and converted further into element energy losses and element heat generation rates per unit volume, respectively. At this stage, essential parameters for this conversion were the hysteresis factor, frequency and element volume data. Unfortunately, the element volume data cannot be obtained from nonlinear stress analysis, consequently, the same FE models were subjected to linear stress analysis in order to fulfill this requirement. The method and equations used for the conversion are fully described in Appendix I.

Step (6) To estimate the temperature rise resulting from heat generation, a finite element thermal analysis must be performed. In this analysis, the steel plate must be modelled together with the rubber matrix in order to accommodate the effects of both heat conduction and heat convection occurring during the analysis. The meshes previously shown were then modified by modelling

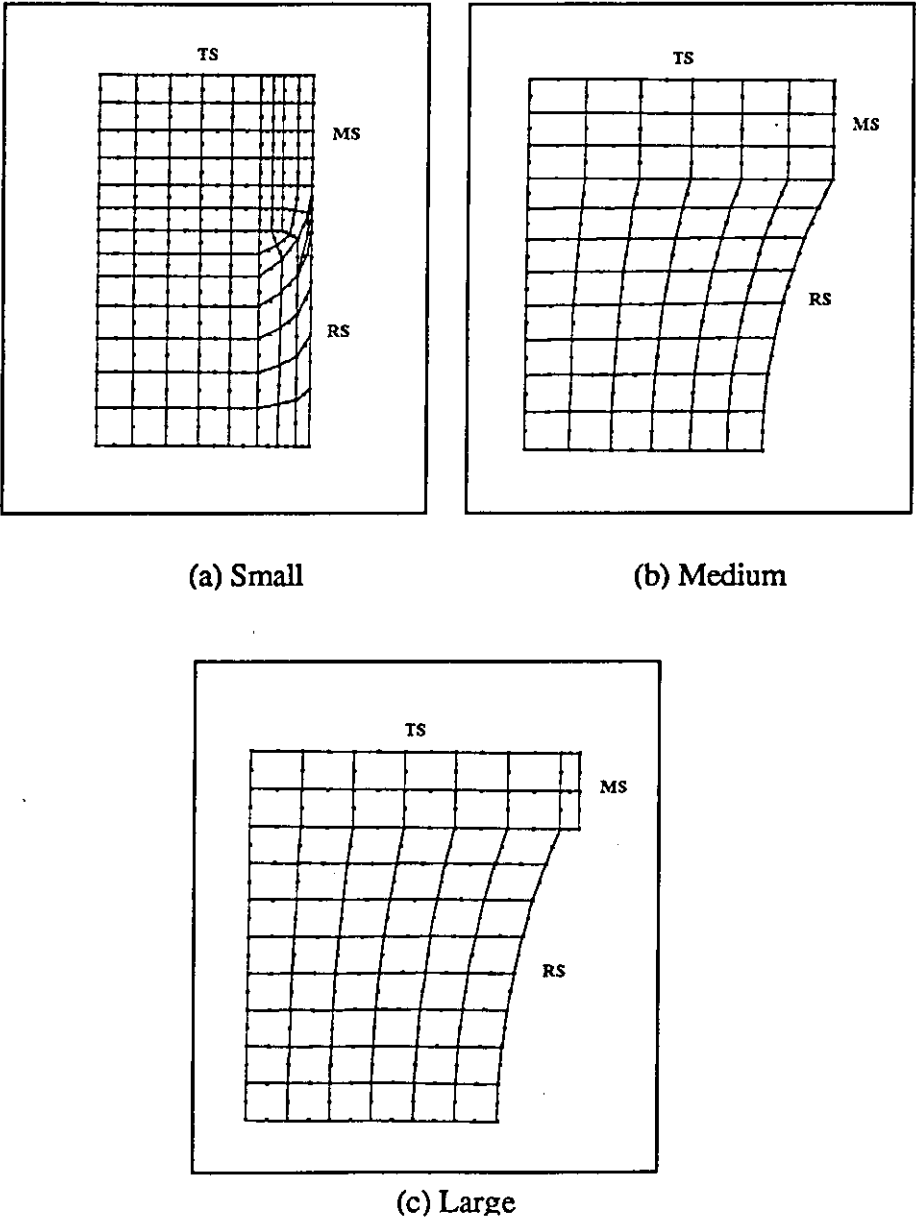


Figure 5.5 FE meshes for thermal analysis of rubber mountings

the steel plate bonded to the top of the rubber component as represented in Figures 5.5. Up to this point, it should be noted that bolts were ignored in the modelling as preliminary analyses had shown that the bolts had no effect on temperature rise in the mountings. Two-dimensional 8-node quadrilateral axisymmetric elements were selected to represent the thermal analysis models.

Step (7) The thermal boundary conditions were then applied based on the assumption that rubber mountings are always connected firmly to a huge metal instrument for testing and heat generated can be transferred from the rubber matrix into the steel plate and the instrument and finally convected to air. With regard to this assumption, the nodal temperatures at the metal plate-instrument interface (TS) were set to remain at ambient temperature (20°C) throughout the analysis. In the meantime, heat transfer coefficients, previously determined in Chapter 4, of “Metalastik 19055” (0.174E-04 W/mm<sup>2</sup>.K) and mild steel (0.097E-04 W/mm<sup>2</sup>.K) were applied to the element faces along the outer surfaces of rubber (RS) and steel plate (MS), respectively. Lastly, the element heat generation rates per unit volume, calculated from step (5), were applied to the elements in the rubber matrix.

Step (8) The material data used for thermal analysis were as follows.

For rubber matrix : Thermal conductivity = 0.000225 W/mm.K\*

For steel plate : Thermal conductivity = 0.05 W/mm.K\*

\*Data supplied by Metalastik

Step (9) After the FE models were complete, steady state thermal analysis was performed. With the NISA post-processor, contour plots of equilibrium temperature distribution of these mountings were established and the

maximum temperature rise was found by subtracting the ambient temperature from the maximum equilibrium temperature.

Step (10) The above procedures were then repeated with different analysis variables (strain amplitude and frequency) with particular regard to the experimental design sets as shown in Table 5.1. Finally, the “STATGRAPHICS”<sup>(117)</sup> programme was introduced to analyse the FE results, in order to estimate the mathematical relationship between maximum temperature rise and the two variables.

*Table 5.1* The experimental design sets for mountings (small, medium and large) subjected to dynamic axial deformation without precompression

Problem No.	A*	B*	Strain (%)	Frequency (Hz)	Note
1	+1	+1	15	40	Factorial point
2	+1	-1	15	10	Factorial point
3	-1	+1	5	40	Factorial point
4	-1	-1	5	10	Factorial point
5	+1.414	0	17.07	25	Star point
6	-1.414	0	2.93	25	Star point
7	0	+1.414	10	46.21	Star point
8	0	-1.414	10	3.79	Star point
9	0	0	10	25	Central point

\* A and B are in design units

#### ♦ Dynamic axial deformation with 10% precompression

In this case, even though the main FEA procedures were almost the same as those previously described, there were some exceptions as presented below.

- i) In step (2), the boundary conditions for nonlinear stress analysis were re-specified. Let us consider the mountings subjected to 7.5% strain at 40 Hz as an example. With 10% precompression, 3 models for each mounting were created based on three different levels of strain amplitude. Hence, the nodes along the top line (TL) of the three models were then moved to the strain levels of 2.5%, 10% and 17.5%, respectively, whereas the other displacement boundary conditions were set to remain the same as those in the previous section.
- ii) In step (10), the FEA procedures were repeated with the analysis variable sets as shown in Table 5.2.

*Table 5.2* The experimental design sets for mountings (small, medium and large) subjected to dynamic axial deformation with 10% precompression

Problem No.	A	B	Strain (%)	Frequency (Hz)	Note
1	+1	+1	7.5	40	Factorial point
2	+1	-1	7.5	10	Factorial point
3	-1	+1	2.5	40	Factorial point
4	-1	-1	2.5	10	Factorial point
5	+1.414	0	8.535	25	Star point
6	-1.414	0	1.465	25	Star point
7	0	+1.414	5	46.21	Star point
8	0	-1.414	5	3.79	Star point
9	0	0	5	25	Central point

#### 5.2.4.2 Dynamic shear deformation

Unlike the axial deformation, the symmetrical criteria for shear deformation can only be met by 3-D solid modelling. Only one particular symmetry plane lying parallel to the direction of shear could be taken into account for the modelling benefit. As a consequence, in this case, FE problems were created by modelling half of the whole domain.

#### ◆ Dynamic shear deformation without precompression

In general, the basic principles of the FEA procedure in this case are very similar to those illustrated in section 5.2.4.1. Only the FE meshes, boundary conditions and the simulated test conditions are different. As an example, by considering the mountings subject to 30% shear strain at 40 Hz, the FEA procedures can be summarised as shown below.

Step (1)     The FE meshes for stress analysis of small, medium and large mountings were created as shown in Figures 5.6. Three-dimensional 20-node hexahedron elements were selected to form these models.

Step (2)     As the mountings were considered as being sheared in both the X and -X directions, two models for each mounting were created based on the direction of shear. For all models, the displacement boundary conditions were applied in such the way that all nodes along the bottom surface were constrained not to move in any direction. Meanwhile, all nodes along the top surface were specified to move either to X or -X direction for 30% strain, whereas their movements in Y and Z directions were restricted during the deformation.

Step (3)     The material data were specified as  
                  $C_{10} = 0.42 \text{ MPa}$   
                  $C_{01} = 0.11 \text{ MPa}$   
                 and Poisson's ratio = 0.499.

Step (4)     Nonlinear stress analysis was then employed to compute the element strain energies of these models.



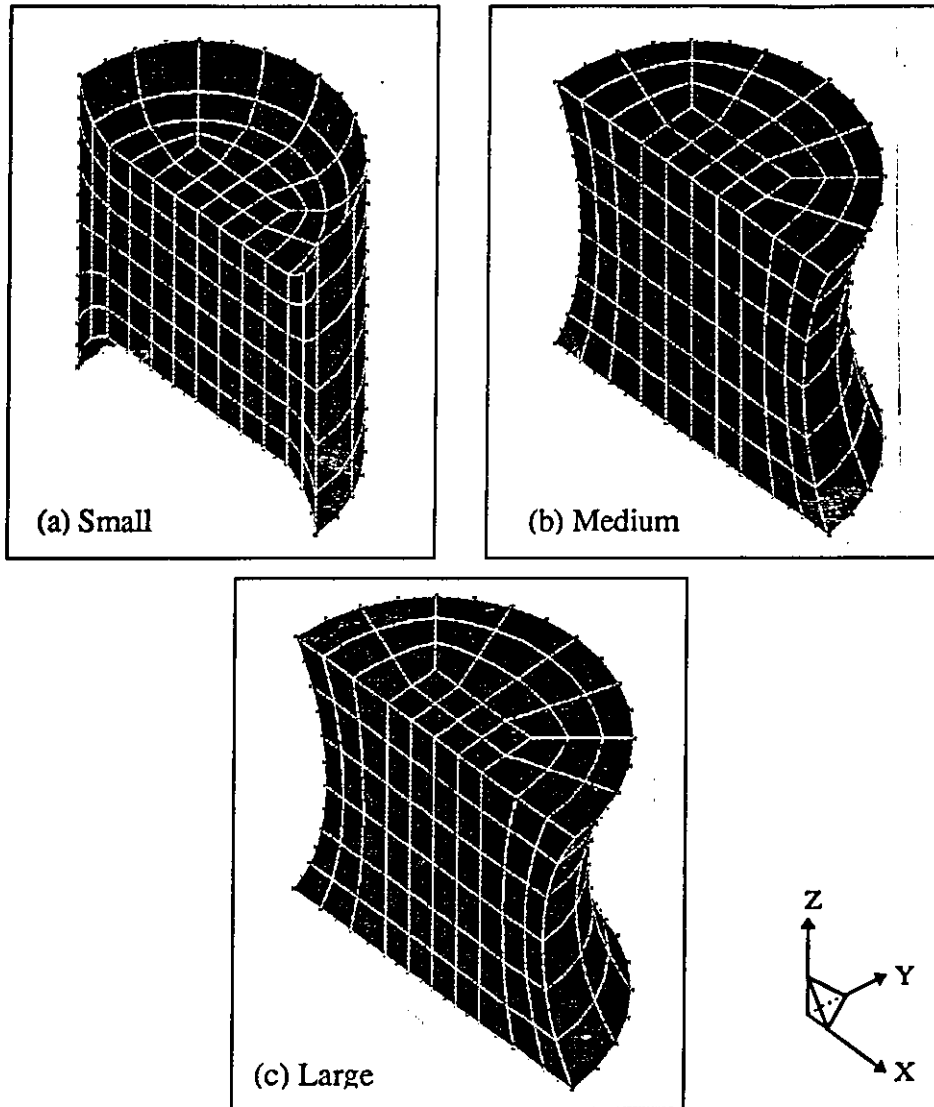


*Figure 5.6* FE meshes for stress analysis of mountings (3-D modelling)

- Step (5)** The element energies obtained were processed further by the method described in Appendix I in order to calculate the net element heat generation rates per unit volume for each mounting.
- Step (6)** Again, for steady state thermal analysis, modifications of the meshes shown in Figures 5.6 were made by modelling the steel plates to both ends (top and bottom) as represented in Figure 5.7.

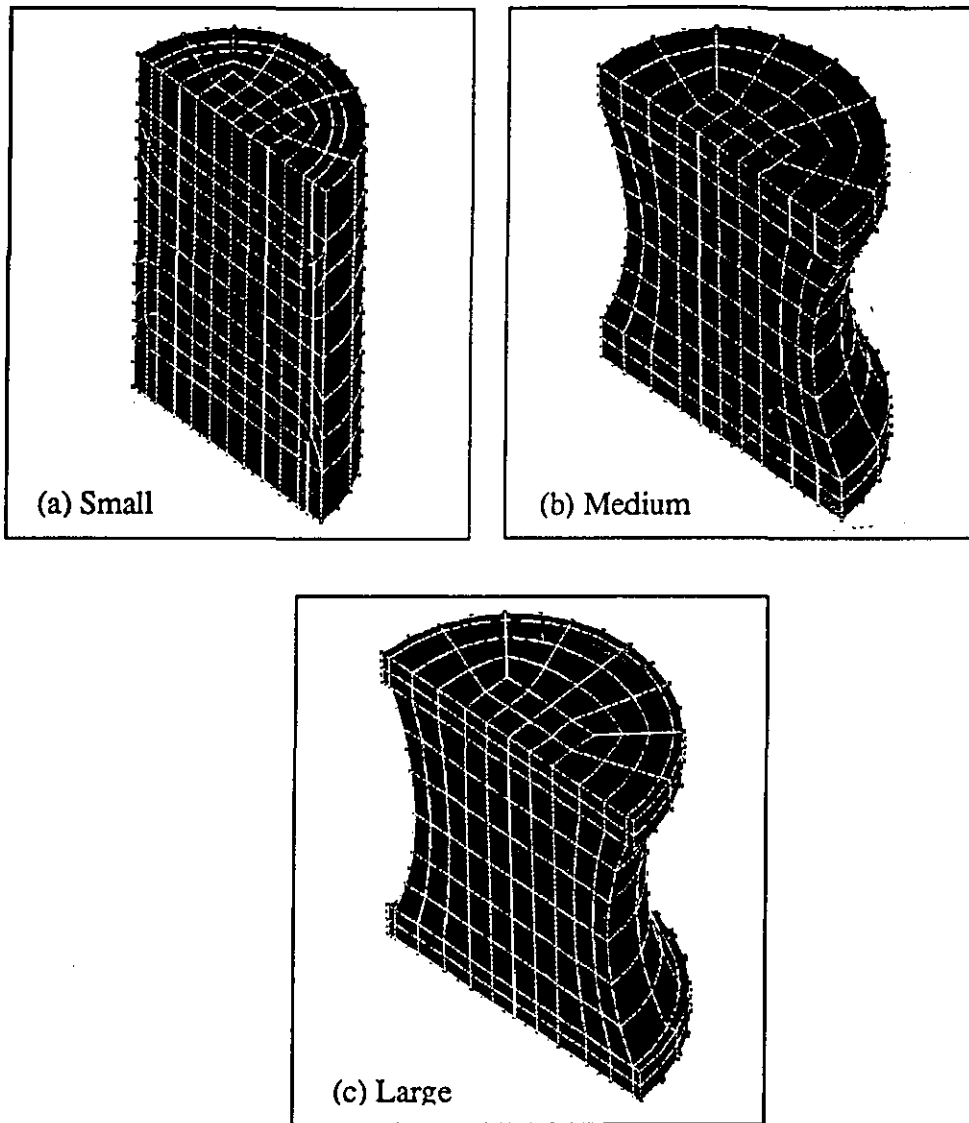


*Figure 5.7* The thermal 3D-solid element models of rubber mountings

- Step (7)**      The thermal boundary conditions were then specified as follows.
- ◆ All nodes along the top and bottom end surfaces were set to remain at 20°C throughout the analysis.
  - ◆ The heat transfer coefficients of rubber and mild steel were applied to the element face along the outer surfaces of rubber and steel, respectively. However, it should be noted that the surfaces along the symmetry plane

were insulated, as no heat was allowed to transfer across this plane.

♦ The element heat generation rates per unit volume, obtained from step (5), were finally applied to the rubber elements.

Step (8) The material data used for thermal analysis were:

For rubber ; Thermal conductivity = 0.000225 W/mm.K

For steel plate ; Thermal conductivity = 0.05 W/mm.K

Step (9) The steady state thermal analysis was then performed to estimate the maximum equilibrium temperature for each model and, by subtracting the ambient temperature (20°C), the maximum temperature rise was predicted.

Step (10) Based on the experimental design, the above procedures were repeated with different variable sets as shown in Table 5.3. Finally, the temperature rise results were analysed by the “STATGRAPHICS” programme.

*Table 5.3* The experimental design sets for mountings under dynamic shear deformation without precompression

Problem No.	A	B	Strain (%)	Frequency (Hz)	Note
1	+1	+1	30	40	Factorial point
2	+1	-1	30	10	Factorial point
3	-1	+1	10	40	Factorial point
4	-1	-1	10	10	Factorial point
5	+1.414	0	34.14	25	Star point
6	-1.414	0	5.86	25	Star point
7	0	+1.414	20	46.21	Star point
8	0	-1.414	20	3.79	Star point
9	0	0	20	25	Central point

♦ **Dynamic shear deformation with 10% precompression.**

The same analysis procedures described above were repeated with the following exceptions:

- i) In step (2), three models per mounting were created based on the boundary conditions applied. In the first model, to simulate the 10% precompression, all nodes along the bottom surface were restrained not to move in any direction. In the meantime, all nodes along the top surface were specified to move downwards to 10% strain while their movements in the other two directions were restricted. In addition, the nodes along the symmetry plane were specified not to move in Y-direction. For the other two models, the same boundary conditions were also applied. However, while the 10% precompression boundary conditions being retained, the nodes along the top surface were set to move further to a certain strain in X and -X directions for the second model and the third model, respectively.
- ii) In step (10), the above procedures were carried out repeatedly with the variable sets as represented in Table 5.4.

*Table 5.4* The experimental design sets for mountings under dynamic shear deformation with 10% precompression

Problem No.	A	B	Strain (%)	Frequency (Hz)	Note
1	+1	+1	15	40	Factorial point
2	+1	-1	15	10	Factorial point
3	-1	+1	5	40	Factorial point
4	-1	-1	5	10	Factorial point
5	+1.414	0	17.07	25	Star point
6	-1.414	0	2.93	25	Star point
7	0	+1.414	10	46.21	Star point
8	0	-1.414	10	3.79	Star point
9	0	0	10	25	Central point

## **5.2.5 Results and Discussion**

### **5.2.5.1 Dynamic axial deformation with/without precompression**

#### **- Contour characteristic of equilibrium temperature distribution**

With the NISA post-processor, the computed temperature results of the mountings can be represented in terms of a colour contour plot. For example, the contour plots of the equilibrium temperature distributions for the mountings subjected to dynamic axial deformation without precompression for 10% strain and 25 Hz (central point) are shown in Figure 5.8. Likewise, the contour plots for those subjected to dynamic axial deformation with 10% precompression for 5% strain and 25 Hz are shown in Figure 5.9. Similar patterns of temperature contours are also obtained for the mountings subjected to different test conditions. Obviously, the maximum equilibrium running temperature is found, in all cases, at the centre of the mountings, whereas the minimum equilibrium running temperature is found at the rubber-metal interface area. The contour plots show that there are various gradations of temperature between the centres and the rubber surfaces. This temperature distribution arises due to the fact that, during the dynamic deformation, heat generated as a result of hysteresis can be dissipated away from the rubber matrix by two main heat transfer processes: heat convection and heat conduction. Heat convection takes place at the rubber-air interface and the heat transfer rate depends mainly upon both the overall temperature difference and the convective heat transfer coefficient between the rubber surface and air. On the other hand, heat convection does not occur at the rubber-metal interface. As the rubber is well bonded to the metal plate, the intimate contact between rubber and metal surfaces is assured. The film barrier to heat flow (alternatively called the convective interface contact resistance) between the two materials, therefore, no longer exists.<sup>(85)</sup> Consequently, the only mode of heat transfer taking place at this interface is heat conduction by which heat is dissipated to the metal.

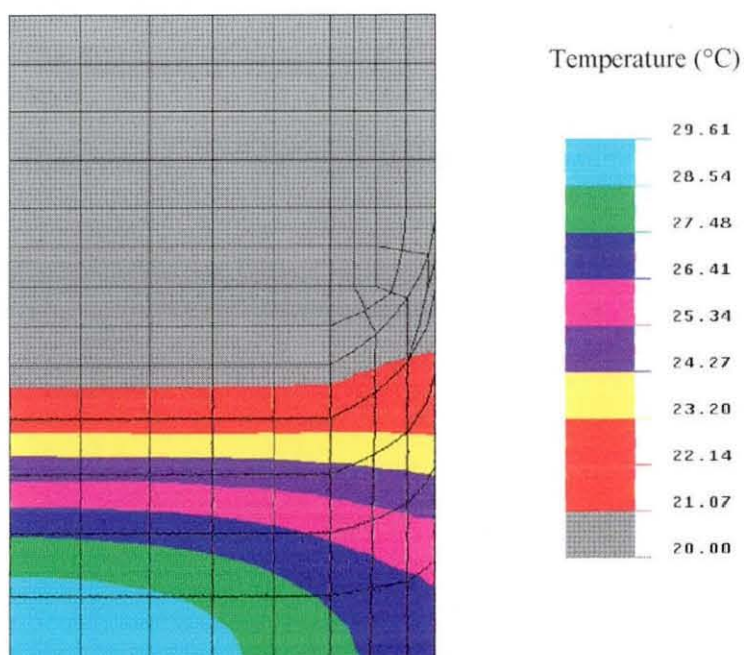


Figure 5.8(a) Equilibrium temperature distribution for the small mounting subjected to dynamic axial deformation without precompression (a quarter of mounting is shown)

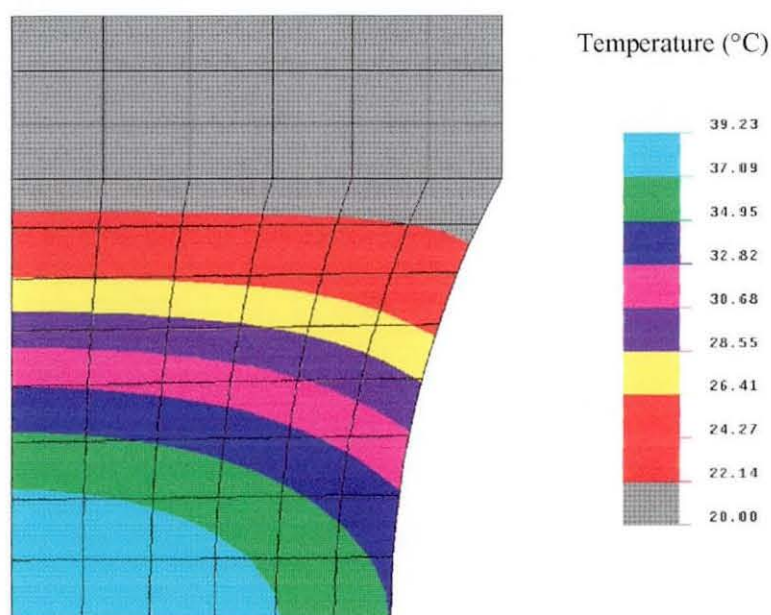


Figure 5.8(b) Equilibrium temperature distribution for the medium mounting subjected to dynamic axial deformation without precompression (a quarter of mounting is shown)

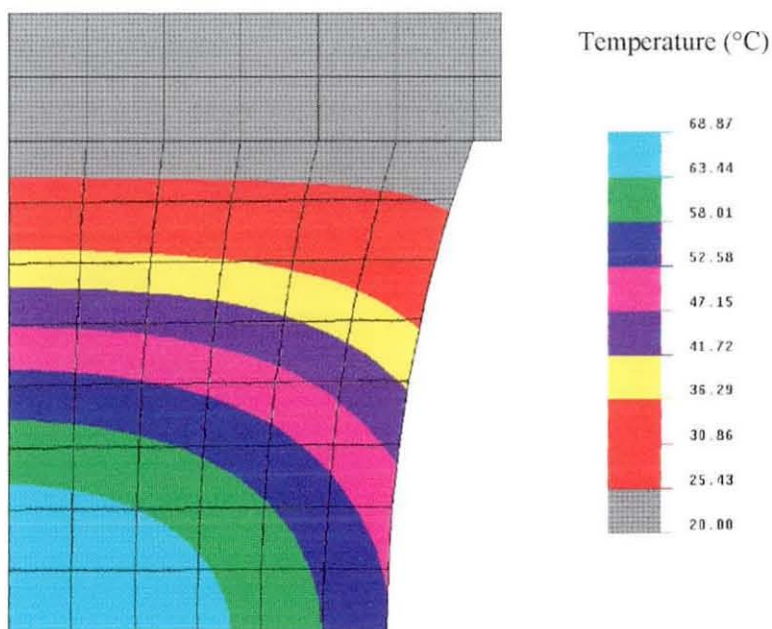


Figure 5.8(c) Equilibrium temperature distribution for the large mounting subjected to dynamic axial deformation without precompression (a quarter of mounting is shown)

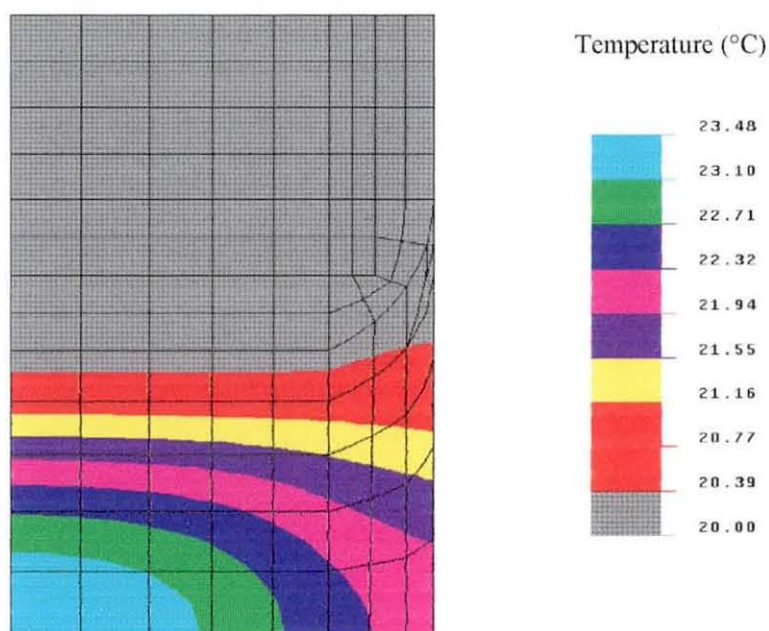


Figure 5.9(a) Equilibrium temperature distribution for the small mounting subjected to dynamic axial deformation with 10% precompression (a quarter of mounting is shown)



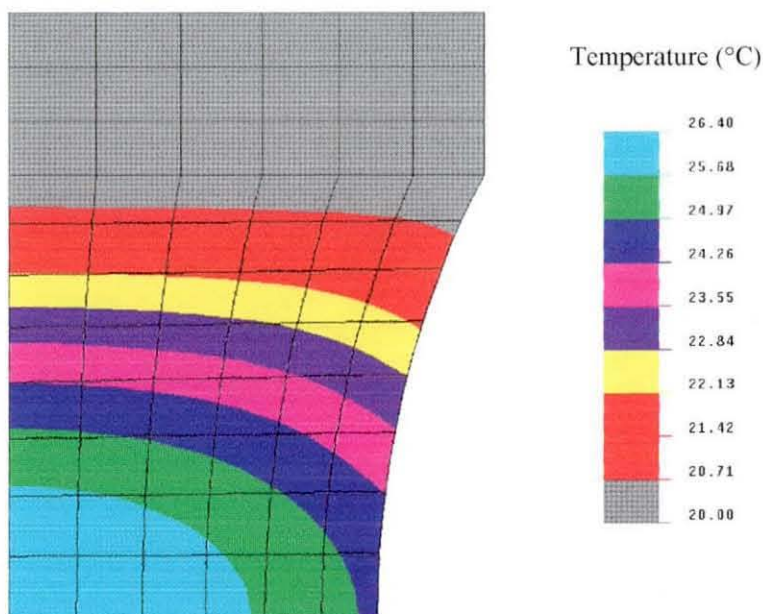


Figure 5.9 (b) Equilibrium temperature distribution for the medium mounting subjected to dynamic axial deformation with 10% precompression (a quarter of mounting is shown)

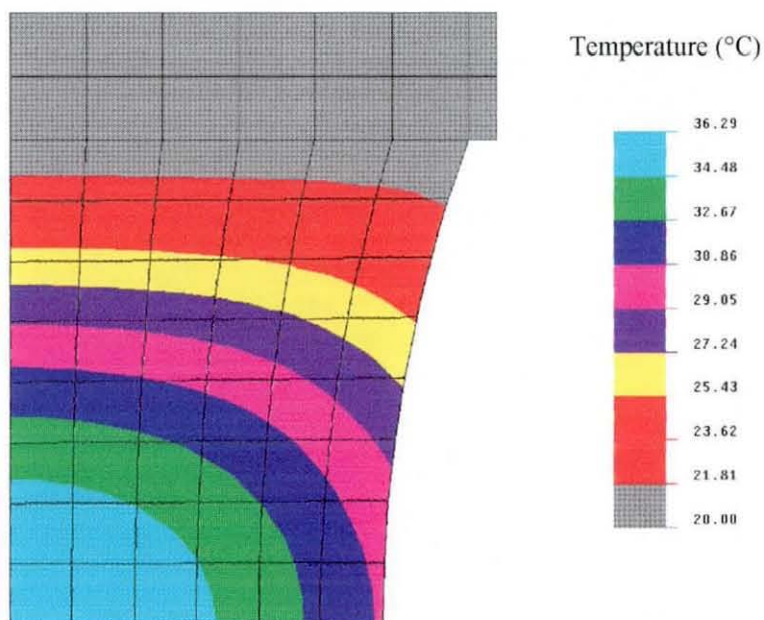


Figure 5.9 (c) Equilibrium temperature distribution for the large mounting subjected to dynamic axial deformation with 10% precompression (a quarter of mounting is shown)



Both heat convection and heat conduction mentioned above are responsible for the temperature reduction of the rubber surfaces. Once the temperatures at the rubber surfaces are lowered, the temperature difference within rubber itself brings about the conduction heat transfer. In this case, heat will be transferred from the high temperature region (at the centre of rubber matrix) to the low temperature region (at the rubber surfaces). It should be borne in mind that all these heat transfer processes take place simultaneously. Since rubber is a poor conductor, at equilibrium state where the element heat generation rate is equivalent to the element heat dissipation rate, the contour plots of equilibrium temperature distribution are obtained with various gradations of temperature between the innermost region and the outermost region. As the equilibrium temperature at the rubber-metal interface is lower than that at the rubber-air interface, this is an indication that the heat conduction rate at rubber-metal interface is much higher than the heat convection rate. A possible explanation is given to the assumption made earlier during the modelling. According to this assumption, the metal plate is connected firmly to a huge metal bar and, therefore, the conducted heat will be dissipated away very quickly, due to a very high thermal conductivity of metal, from the metal plate into the metal bar and, finally, to the surroundings. This phenomenon is generally known as “heat sink”. For this reason, the temperature of the metal plate is expected to remain at ambient temperature all the time, giving rise to a larger temperature difference between rubber and metal surfaces and, hence, a faster heat conduction rate at the rubber-metal interface. A mathematical proof of this will be given in the next chapter.

**- The effects of test conditions and geometric factor on the maximum temperature rise**

In the project, importance is given to the maximum equilibrium temperature because it is this parameter which indicates the degree of possible thermal degradation taking place inside the rubber matrix. However, instead of the maximum equilibrium temperature, the maximum temperature rise (the maximum equilibrium temperature - ambient temperature) is chosen to represent the temperature results in the subsequent section.

This is because the maximum equilibrium temperature depends on the ambient temperature whereas the preliminary analyses have shown that the maximum temperature rise is independent of the ambient temperature, provided that the variation in ambient temperature does not change significantly the physical and thermal properties of the rubber compound.

Table 5.5 summarises the maximum temperature rises ( $T_{max}$ ), together with the maximum element strain energy densities ( $E_{max}$ ) obtained during the dynamic deformation, for the mountings subjected to the various test conditions. As the strain energy density is directly proportional to the heat generation rate, the maximum temperature rise is found to increase with increasing the maximum element strain energy density when compared at the same frequency. However, it should be noted at this point that, apart from the strain energy density, the maximum temperature rise also depends on the frequency and the mounting geometry as these two factors govern the rates of heat generation and heat dissipation, respectively.

Based on the experimental design technique, a mathematical relationship between the maximum temperature rise and the two test variables (strain amplitude ( $\epsilon$ ) and frequency ( $f$ )) for each mounting can be obtained as given in Table 5.6. This relationship is generally known as the “Quadratic response model” which can be represented mathematically by the following form:

$$T_{max} = a_0 + a_1.\epsilon + a_2.f + a_3.\epsilon.f + a_4.\epsilon^2 + a_5.f^2 \quad \text{----- (5.1)}$$

where  $T_{max}$  = maximum temperature rise

$\epsilon$  = strain amplitude

$f$  = frequency

and  $a_0, a_1, a_2, a_3, a_4$  and  $a_5$  are equation coefficients.

However, it can be observed that the response equations shown in Table 5.6 do not include the frequency squared term. This is because the equation coefficient  $a_5$  is very small, compared to the other coefficients, and is proved by the “STATGRAPHICS”

**Table 5.5** The maximum temperature rise and the maximum element strain energy density for mountings subjected to dynamic axial deformation.

Deformation mode	Test conditions	$E_{\max.} (x10^{-2} \text{ mJ/mm}^3)$			$T_{\max.} (^\circ\text{C})$		
		Small	Medium	Large	Small	Medium	Large
Dynamic axial without precompression	2.93%strain, 25 Hz	1.43	0.43	0.51	0.8	1.6	4.2
	5%strain, 10 Hz	4.17	1.26	1.50	0.9	1.9	4.9
	5%strain, 40 Hz	4.17	1.26	1.50	3.8	7.6	19.4
	10%strain, 3.79 Hz	16.97	5.06	6.06	1.5	2.9	7.4
	10%strain, 25 Hz	16.97	5.06	6.06	9.6	19.2	48.9
	10%strain, 46.21 Hz	16.97	5.06	6.06	17.8	35.5	90.3
	15%strain, 10 Hz	39.38	11.39	13.87	8.9	17.5	44.6
	15%strain, 40 Hz	39.38	11.39	13.87	35.4	70.1	178.3
	17.07%strain, 25 Hz	51.87	14.76	18.13	29.0	57.2	145.3
Dynamic axial with 10% precompression	1.465%strain, 25 Hz	0.58	0.18	0.18	0.3	0.6	1.4
	2.5%strain, 10 Hz	1.68	0.53	0.53	0.3	0.6	1.6
	2.5%strain, 40 Hz	1.68	0.53	0.53	1.4	2.6	6.5
	5%strain, 3.79 Hz	6.78	2.13	2.14	0.5	1.0	2.5
	5%strain, 25 Hz	6.78	2.13	2.14	3.5	6.4	16.3
	5%strain, 46.21 Hz	6.78	2.13	2.14	6.4	11.8	30.1
	7.5%strain, 10 Hz	15.43	4.82	4.84	3.2	5.8	14.7
	7.5%strain, 40 Hz	15.43	4.82	4.84	12.6	23.1	58.9
	8.535%strain, 25 Hz	20.12	6.25	6.28	10.3	18.8	47.8

programme to be statistically insignificant. Consequently, the term  $a_5.f^2$  was eliminated and the other equation coefficients ( $a_0$ ,  $a_1$ ,  $a_2$ ,  $a_3$  and  $a_4$ ) were then re-determined.

*Table 5.6* The estimated response equations for the mountings subjected to dynamic axial deformation

Deformation mode	Size	The response equations	R-squared
Without precompression	Small	$T_{\max} = 9.61 + 9.92\varepsilon + 6.56f + 5.93\varepsilon f + 2.65\varepsilon^2$	0.996
	Medium	$T_{\max} = 19.22 + 19.58\varepsilon + 13.06f + 11.72\varepsilon f + 5.08\varepsilon^2$	0.996
	Large	$T_{\max} = 48.85 + 49.78\varepsilon + 33.19f + 29.80\varepsilon f + 12.94\varepsilon^2$	0.996
With 10% precompression	Small	$T_{\max} = 3.48 + 3.52\varepsilon + 2.36f + 2.11\varepsilon f + 0.90\varepsilon^2$	0.996
	Medium	$T_{\max} = 6.40 + 6.43\varepsilon + 4.33f + 3.86\varepsilon f + 1.63\varepsilon^2$	0.997
	Large	$T_{\max} = 16.29 + 16.39\varepsilon + 11.02f + 9.82\varepsilon f + 4.15\varepsilon^2$	0.997

As can be seen, all of the coefficients of correlation (R-squared value) are very high (>0.99 with 8 degree of freedom). This indicates that it is acceptable to use these response equations to estimate the maximum temperature rise for any combination of the test variables. Also, it can be observed that, even though these three mountings are different in size, their response equations are very similar in terms of the relative values of their coefficients.

Equation (5.1) reveals that the relationship between maximum temperature rise and strain amplitude is nonlinear. This nonlinearity arises from the fact that the maximum

temperature rise is directly proportional to the heat generation rates, that is the product of loss energy (strain energy x hysteresis factor) and frequency. Basically, it is accepted that the strain energy is proportional to the product of stress and strain. For a given “modulus” or stiffness, where stress can be represented mathematically in terms of strain, the strain energy is therefore proportional to the square of the strain. According to this relationship, the maximum temperature rise is found to be related nonlinearly to the strain amplitude as stated clearly by the squared term of the equation. As previously mentioned, the maximum temperature rise is directly proportional to the product of energy loss and frequency, thus, a linear relationship between the maximum temperature rise and frequency is obtained, even though there is an interaction effect of strain amplitude and frequency on the maximum temperature rise. The interaction term indicates that the effect of varying frequency on the maximum temperature rise differs according to the level of strain amplitude and vice versa. Moreover, it can be observed that the equation coefficients ( $a_0$ ,  $a_1$ ,  $a_2$ ,  $a_3$  and  $a_4$ ) are all positive for each individual equation. This means the maximum temperature rise will increase continuously with increasing strain amplitude and/or frequency.

In addition to the qualitative similarities, there is also a quantitative correlation between the response equations obtained from the same deformation mode. As can be observed, regardless of the test conditions, the maximum temperature rise of the small, medium and large mountings can be related mathematically, as expressed below.

$$T_{max. (L)} = K_{LM} \cdot T_{max. (M)} = K_{LS} \cdot T_{max. (S)} \quad \text{----- (5.2)}$$

and, therefore,

$$T_{max. (M)} = K_{MS} \cdot T_{max. (S)} \quad \text{----- (5.3)}$$

where  $T_{max. (L)}$ ,  $T_{max. (M)}$  and  $T_{max. (S)}$  are respectively the maximum temperature rise of the large, medium and small mountings. Since the constants  $K_{LM}$ ,  $K_{LS}$  and  $K_{MS}$  depend on the size differences between the mountings, they will be called the “geometric difference constants”. Table 5.7 lists the approximate values of these geometric difference constants.

It should be noted at this point that the mountings selected in this study are different not only in size but also in configuration, therefore it is impossible to determine precisely the effect of geometric factor on the maximum temperature rise. However, it is expected

*Table 5.7* Approximate values of the geometric difference constant.

	Dynamic axial without precompression	Dynamic axial with 10% precompression
$K_{LM}$	2.54	2.54
$K_{LS}$	5.07	4.67
$K_{MS}$	2.00	1.83

that the maximum temperature rise should depend on both surface area and volume of the mountings as these two parameters are known to have a great influence on heat transfer process. It is understandable that an increase in surface area will promote the convective heat dissipation process by which heat can be transferred out of the rubber matrix. Thus, more heat can be dissipated away as the surface area of the mountings is increased. Consequently, an increase in surface area generally causes a reduction in the maximum temperature rise. On the contrary, an increase in volume of the mounting generally results in an increase in distance between the centre and the surface and, therefore, causes a reduction in heat conduction rate at the centre of the mounting. Unquestionably, the maximum temperature rise should increase with increasing volume of the mountings. For this reason, attempts have been made to study the qualitative relationship between the maximum temperature rise and the ratio of volume to surface area of the mounting. Table 5.8 lists the volume (V) and surface area (A) for each mounting. The plots of the maximum temperature rise against the ratio of volume to surface area under various test conditions are then established as shown in Figure 5.10.

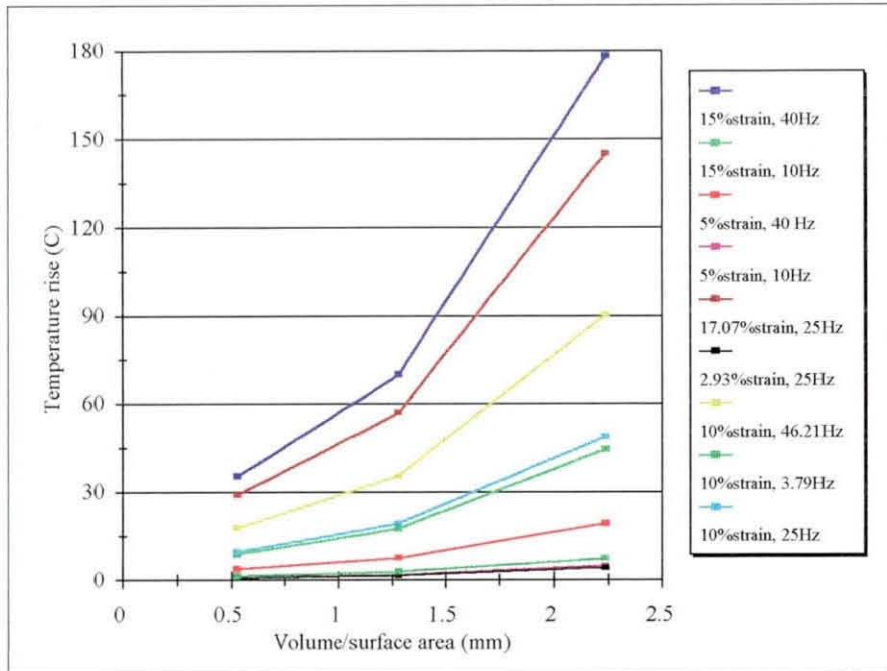
*Table 5.8* Volume and surface area of the mountings

Size	Volume (mm <sup>3</sup> )	Total surface area (mm <sup>2</sup> )	Volume/total surface area (mm)
Small	284.6	537.9	0.53
Medium	2212.7	1729.4	1.28
Large	10290.4	4598.2	2.24

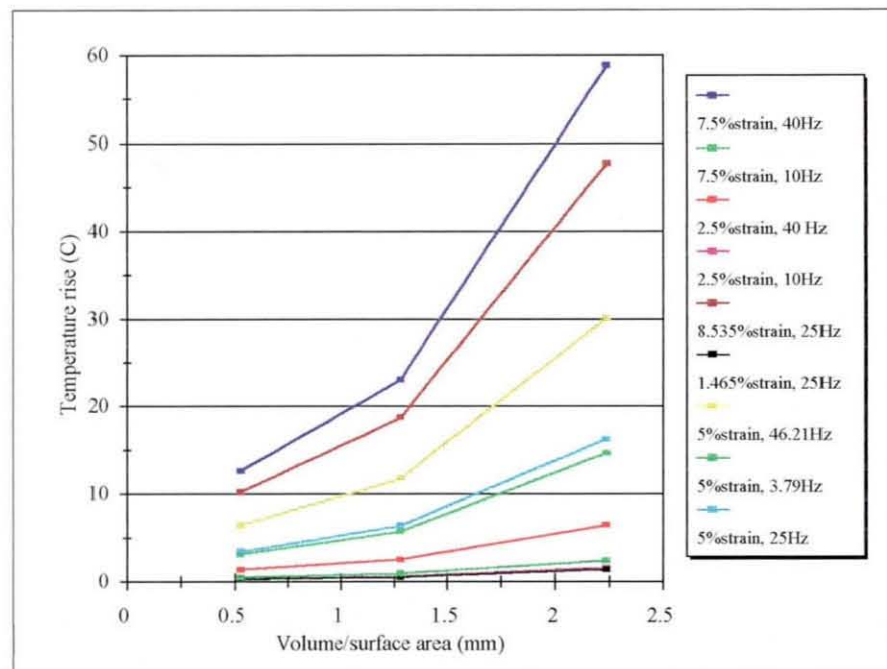
The results show that, for the same test conditions, the maximum temperature rise increases with the ratio of volume to surface area of the mounting. This is the reason why the maximum temperature rise of the large mounting is much higher than those of the medium and small mountings. Unfortunately, due to the configuration difference of the selected mountings, the results shown in Figure 5.10 cannot be interpreted quantitatively, for instance, to estimate the maximum temperature rise of other mountings with different ratios of volume to surface area.

**- Contour plots of the maximum temperature rise**

With reference to the response equations shown in Table 5.6, the contour plots of the maximum temperature rise as a function of strain amplitude and frequency can be generated, as shown in Figures 5.11 and 5.12 for the dynamic axial deformation without and with 10% precompression, respectively. Practically, these contour plots can be used as guidance for rubber engineers to determine suitable regions of service conditions for these particular mountings if the temperature tolerance of the rubber compound is known.



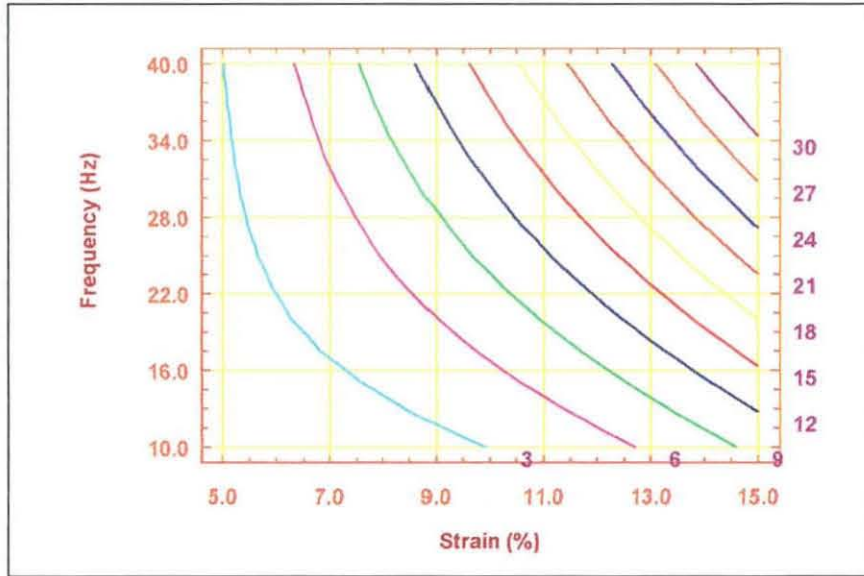
(a) For dynamic axial deformation without precompression



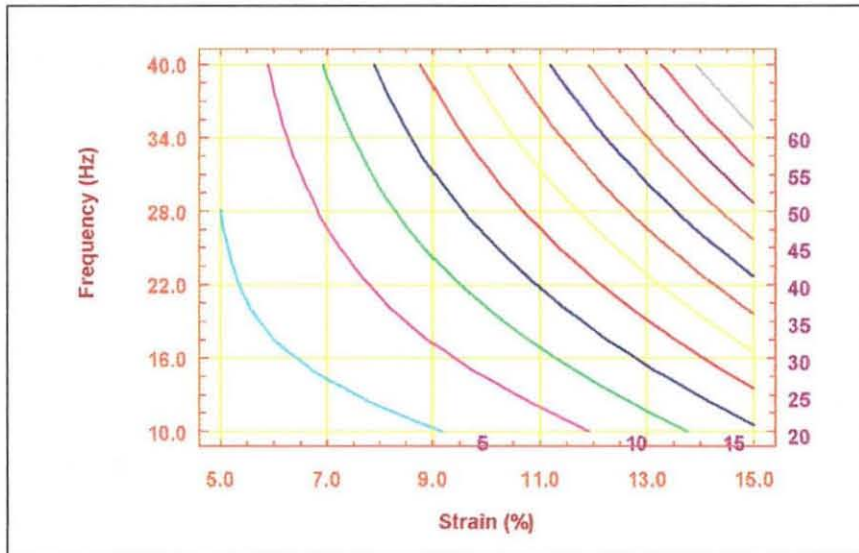
(b) For dynamic axial deformation with 10% precompression

Figure 5.10 The plots of the maximum temperature rise against the ratio of volume to total surface area





*Figure 5.11(a)* The effects of strain amplitude and frequency on the maximum temperature rise ( $^{\circ}\text{C}$ ) for the small mounting subjected to dynamic axial deformation without precompression



*Figure 5.11 (b)* The effects of strain amplitude and frequency on the maximum temperature rise ( $^{\circ}\text{C}$ ) for the medium mounting subjected to dynamic axial deformation without precompression

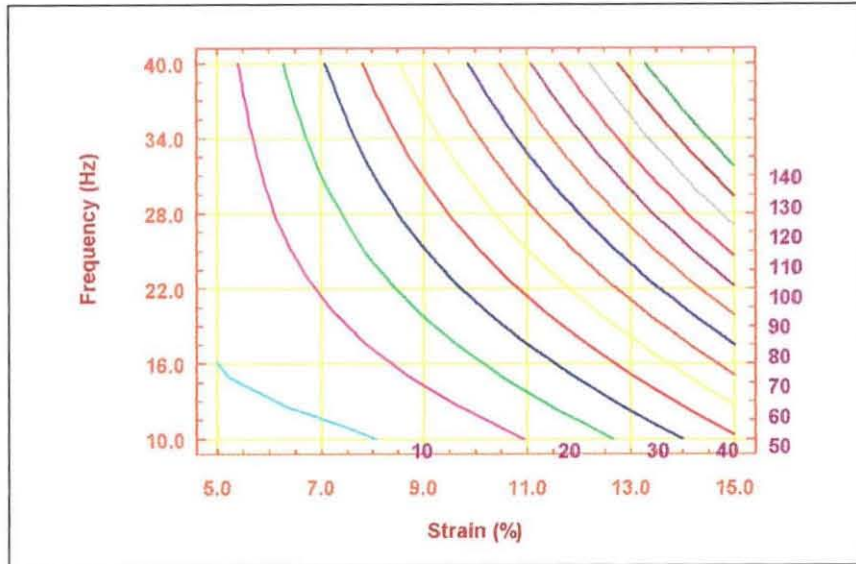


Figure 5.11 (c) The effects of strain amplitude and frequency on the maximum temperature rise ( $^{\circ}\text{C}$ ) for the large mounting subjected to dynamic axial deformation without precompression

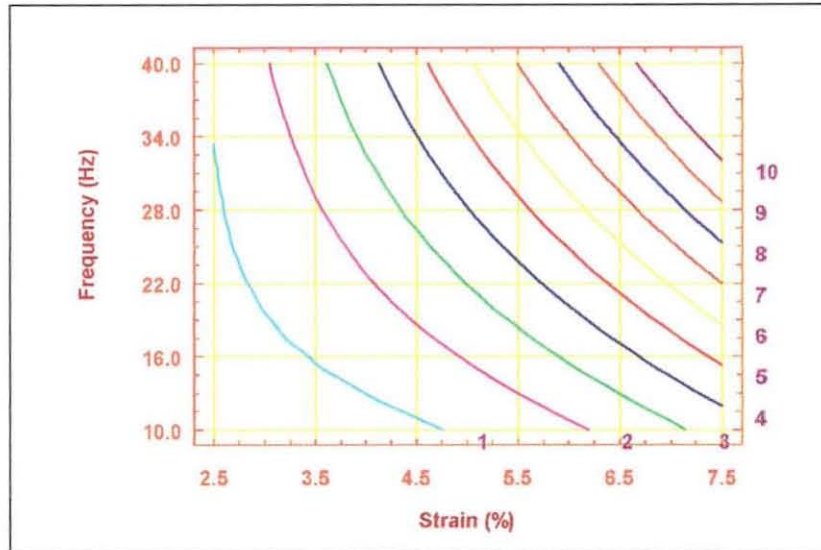


Figure 5.12 (a) The effects of strain amplitude and frequency on the maximum temperature rise ( $^{\circ}\text{C}$ ) for the small mounting subjected to dynamic axial deformation with 10% precompression

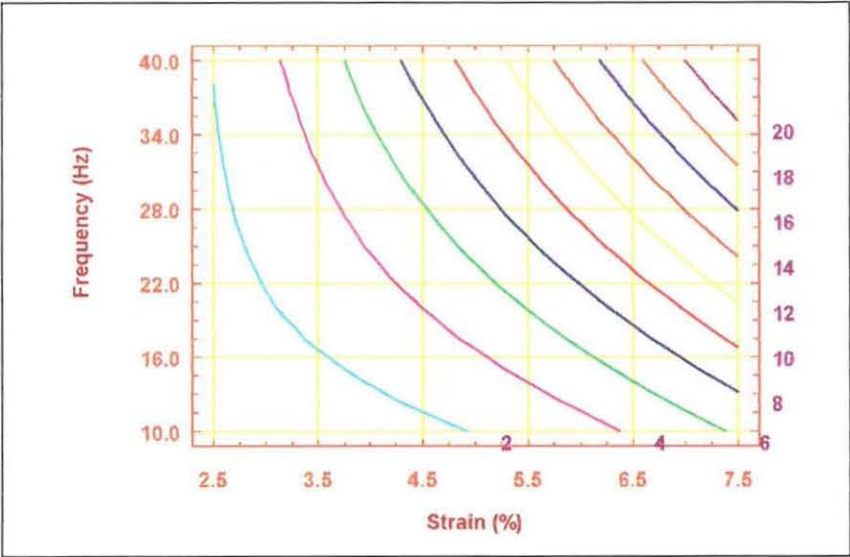


Figure 5.12 (b) The effects of strain amplitude and frequency on the maximum temperature rise ( $^{\circ}\text{C}$ ) for the medium mounting subjected to dynamic axial deformation with 10% precompression

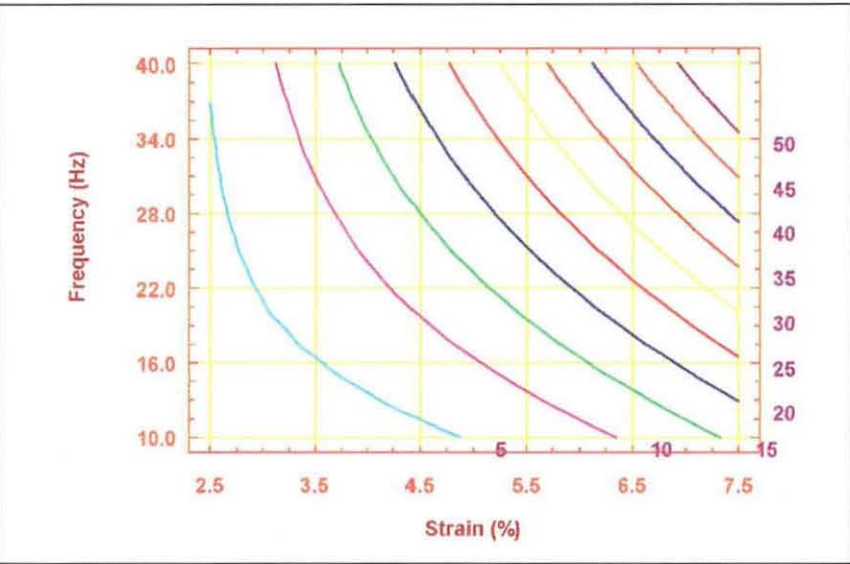


Figure 5.12 (c) The effects of strain amplitude and frequency on the maximum temperature rise ( $^{\circ}\text{C}$ ) for the large mounting subjected to dynamic axial deformation with 10% precompression



### 5.2.5.2 Dynamic shear deformation with/without precompression

#### - Contour characteristic of equilibrium temperature distribution

As in the case of dynamic axial deformation, the contour pattern of equilibrium temperature distribution is found to be independent of the test conditions. For this reason, only the contour plots for the mountings subjected to chosen test conditions are given. Given as examples are the contour plots for the mountings subjected to dynamic shear deformation without precompression at 20% strain and 25 Hz (Figure 5.13) and those for the mountings subjected to dynamic shear deformation with 10% precompression at 10% strain and 25 Hz (Figure 5.14). It can be observed that, regardless of the difference in deformation mode, the main characteristic of the temperature distribution pattern remains unchanged. The maximum equilibrium running temperature is still found at the centre of the mountings, while the minimum equilibrium running temperature is found at the rubber-metal interface area. This characteristic is governed mainly by the heat transfer process as explained fully in the previous section. However, it is obvious that the temperature gradation pattern obtained from dynamic shear deformation is not axisymmetrical, unlike the pattern obtained from dynamic axial deformation. This is attributed to the fact that the temperature rise at any point in the rubber matrix is proportional to both heat dissipation rate and heat generation rate. Due to an axisymmetry of the mounting configuration, the distribution pattern of heat dissipation rate should be axisymmetrical, regardless of the deformation mode. Generally, it is understandable that the heat generation rate is directly proportional to the strain energy in which its distribution pattern depends remarkably on the deformation mode (the applied loads or displacement). Thus, the distribution pattern of heat generation rate should also depend on the deformation mode. In the case of dynamic axial deformation, the applied displacement is axisymmetrical, therefore, an axisymmetrical distribution pattern of heat generation rate can be expected. As the distribution patterns of both heat dissipation rate and heat generation rate are axisymmetrical, the temperature gradation pattern should also be axisymmetrical (See

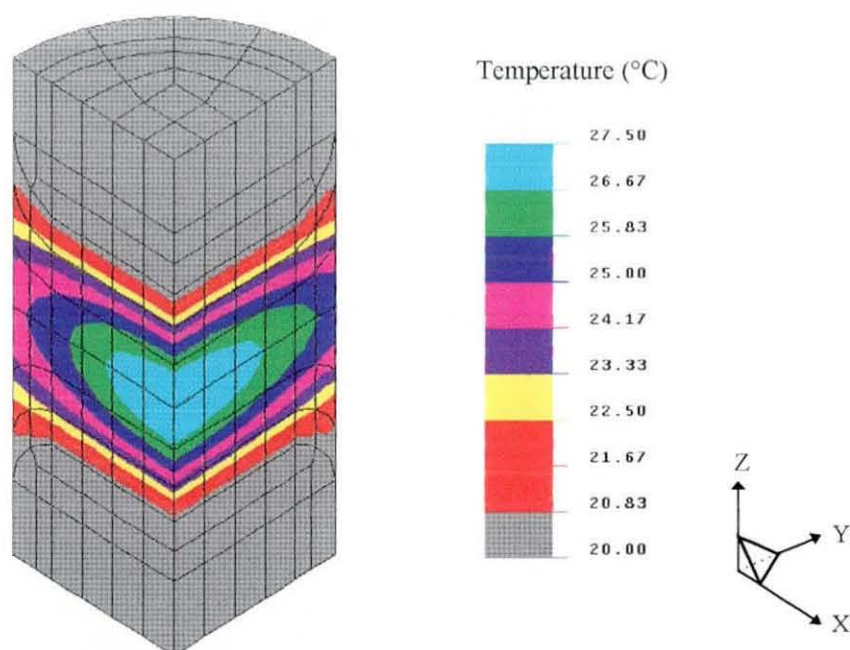


*Figure 5.13(a)* Equilibrium temperature distribution for the small mounting subjected to dynamic shear deformation (in X-axis direction) without precompression (a quarter of mounting is shown)

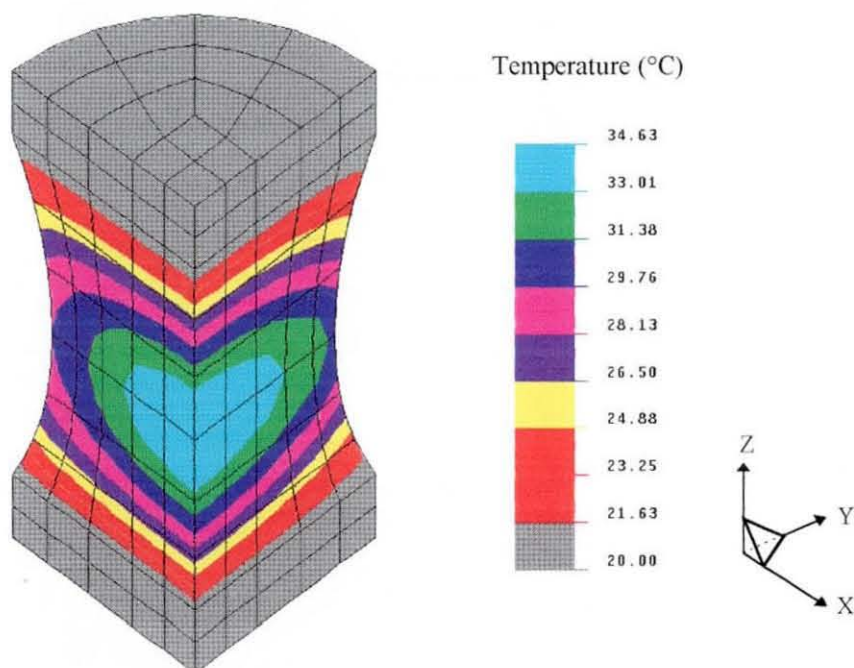


*Figure 5.13(b)* Equilibrium temperature distribution for the medium mounting subjected to dynamic shear deformation (in X-axis direction) without precompression (a quarter of mounting is shown)

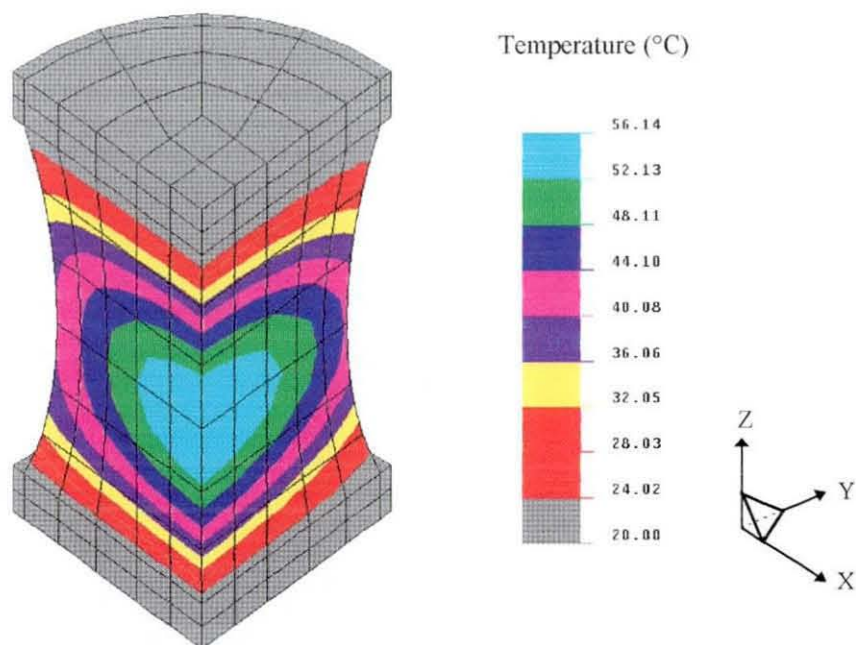


*Figure 5.13(c)* Equilibrium temperature distribution for the large mounting subjected to dynamic shear deformation (in X-axis direction) without precompression (a quarter of mounting is shown)

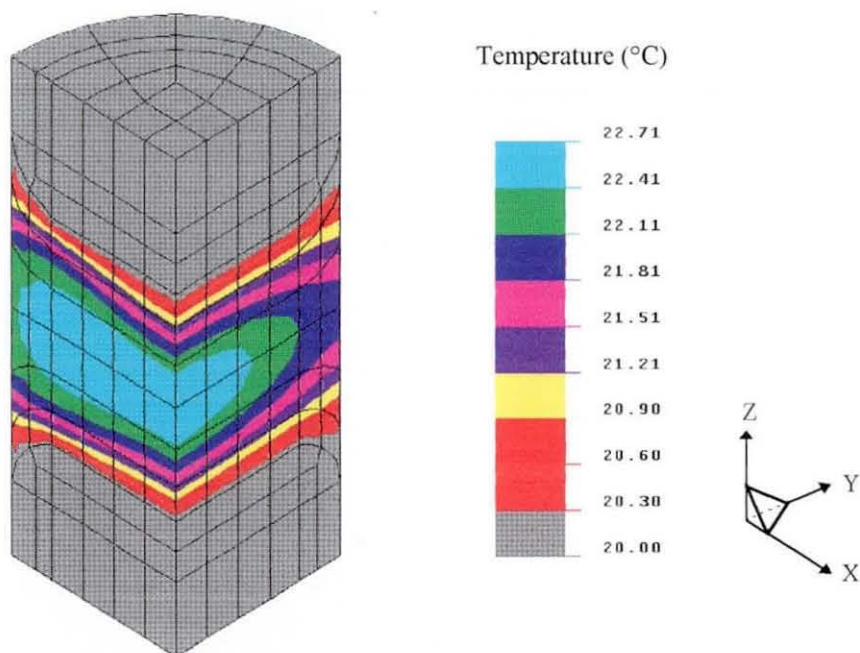


*Figure 5.14(a)* Equilibrium temperature distribution for the small mounting subjected to dynamic shear deformation (in X-axis direction) with 10% precompression (a quarter of mounting is shown)



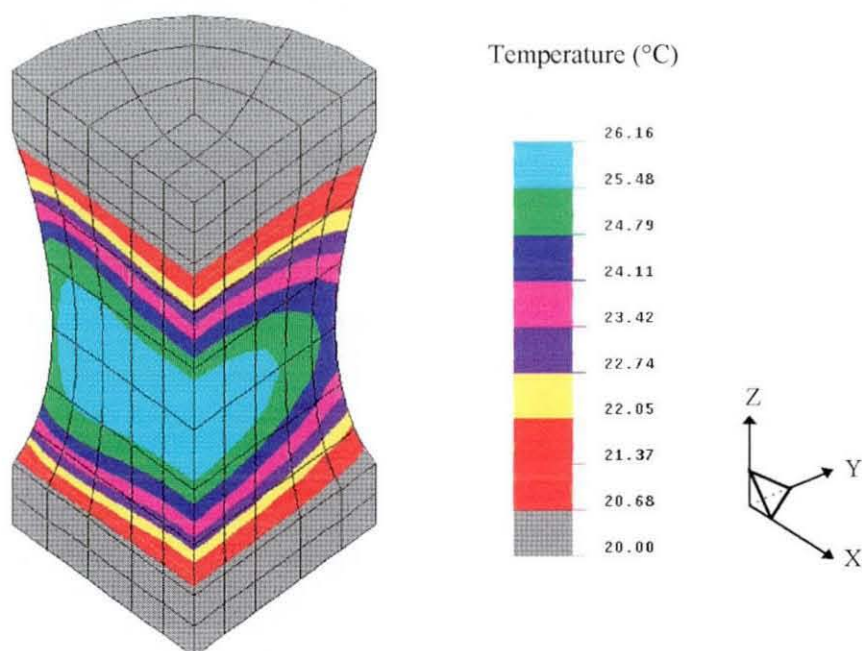


*Figure 5.14(b)* Equilibrium temperature distribution for the medium mounting subjected to dynamic shear deformation (in X-axis direction) with 10% precompression (a quarter of mounting is shown)

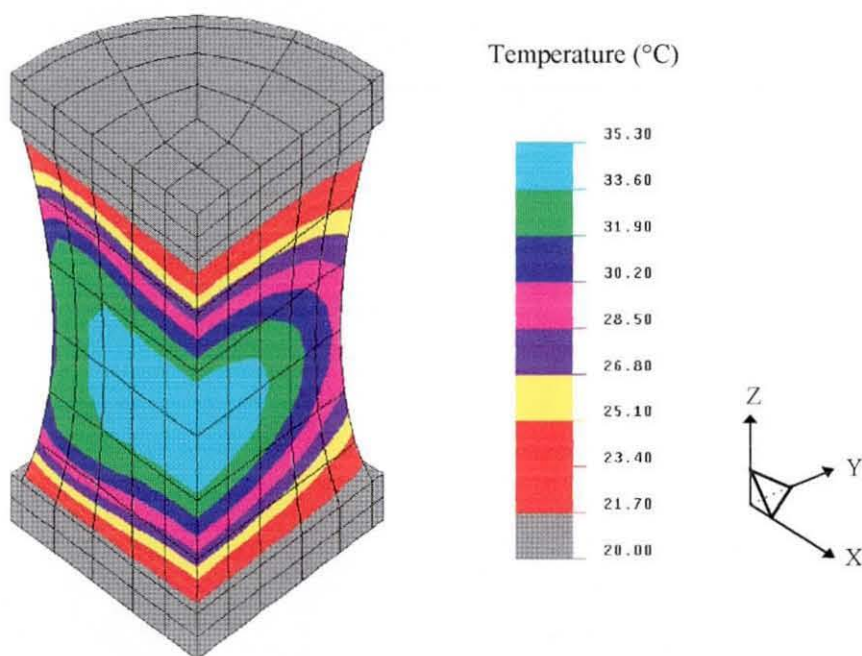


*Figure 5.14(c)* Equilibrium temperature distribution for the large mounting subjected to dynamic shear deformation (in X-axis direction) with 10% precompression (a quarter of mounting is shown)

also Figures 5.8 and 5.9). On the contrary, in the case of dynamic shear deformation, the applied displacement is not axisymmetrical, giving rise to a non-axisymmetrical distribution pattern of heat generation rate within the rubber matrix. The temperature gradation pattern is, therefore, found to be non-axisymmetrical as obviously seen in Figures 5.13 and 5.14. In addition, for the dynamic shear deformation, precompression appears to have a great influence on the temperature gradation pattern. Again, this indicates that the temperature gradation pattern depends greatly on the deformation mode.

#### **- The effects of test conditions and geometric factor on the maximum temperature rise**

Table 5.9 shows the maximum temperature rise ( $T_{max}$ ) and the maximum element strain energy density ( $E_{max}$ ) for the mountings subjected to dynamic shear deformation under various test conditions. Again, based on the experimental design technique, the response equations relating the maximum temperature rise to the two test variables are obtained as represented in Table 5.10.

It is clearly seen that the coefficients of correlation for all response equations are very high ( $> 0.99$ ). This assures us that these response equations fit very well to the computed data and, therefore, can be used to estimate the relationship between the maximum temperature rise and the test variables with high accuracy. It is also evident that the "Quadratic response model" (Equation (5.1)) is perfectly applicable to represent the response equations shown in Table 5.10. This means that the qualitative relationship between the maximum temperature rise and the test variables for the mountings subjected to dynamic shear deformation is the same as that for the mountings subjected to dynamic axial deformation.



**Table 5.9** The maximum temperature rise and the maximum element strain energy density for mountings subjected to dynamic shear deformation.

Deformation mode	Test conditions	E <sub>max.</sub> (x10 <sup>-2</sup> mJ/mm <sup>3</sup> )			T <sub>max.</sub> (°C)		
		Small	Medium	Large	Small	Medium	Large
Dynamic shear without precompression	5.86%strain, 25 Hz	1.17	0.47	0.47	0.6	1.3	3.1
	10%strain, 10 Hz	3.40	1.37	1.36	0.8	1.5	3.6
	10%strain, 40 Hz	3.40	1.37	1.36	3.0	5.9	14.5
	20%strain, 3.79 Hz	13.36	5.43	5.38	1.1	2.2	5.5
	20%strain, 25 Hz	13.36	5.43	5.38	7.5	14.6	36.1
	20%strain, 46.21 Hz	13.36	5.43	5.38	13.9	27.1	66.8
	30%strain, 10 Hz	29.20	12.01	11.88	6.7	13.1	32.3
	30%strain, 40 Hz	29.20	12.01	11.88	26.9	52.4	129.3
	34.14%strain, 25 Hz	37.21	15.42	15.24	21.7	42.3	104.3
Dynamic shear with 10% precompression	2.93%strain, 25 Hz	3.00	1.52	1.56	0.7	1.5	3.5
	5%strain, 10 Hz	5.07	2.58	2.65	0.5	1.0	2.5
	5%strain, 40 Hz	5.07	2.58	2.65	2.0	4.2	9.9
	10%strain, 3.79 Hz	9.71	5.07	5.21	0.4	0.9	2.3
	10%strain, 25 Hz	9.71	5.07	5.21	2.7	6.2	15.3
	10%strain, 46.21 Hz	9.71	5.07	5.21	5.0	11.4	28.3
	15%strain, 10 Hz	11.32	7.40	7.57	2.0	4.5	11.1
	15%strain, 40 Hz	11.32	7.40	7.57	8.2	18.0	44.5
	17.07%strain, 25 Hz	15.68	8.29	8.46	5.9	13.7	34.0

*Table 5.10* The estimated response equations for the mountings subjected to dynamic shear deformation

Deformation mode	Size	The response equations	R-squared
Without precompression	Small	$T_{\max} = 7.50 + 7.47\epsilon + 5.05f + 4.48\epsilon f + 1.84\epsilon^2$	0.997
	Medium	$T_{\max} = 14.64 + 14.52\epsilon + 9.85f + 8.72\epsilon f + 3.57\epsilon^2$	0.997
	Large	$T_{\max} = 36.15 + 35.82\epsilon + 24.33f + 21.52\epsilon f + 8.79\epsilon^2$	0.997
With 10% precompression	Small	$T_{\max} = 2.77 + 1.89\epsilon + 1.77f + 1.18\epsilon f + 0.31\epsilon^2$	0.996
	Medium	$T_{\max} = 6.17 + 4.33\epsilon + 3.92f + 2.59\epsilon f + 0.72\epsilon^2$	0.999
	Large	$T_{\max} = 15.29 + 10.79\epsilon + 9.69f + 6.48\epsilon f + 1.74\epsilon^2$	0.999

Moreover, quantitative interpretation of these response equations reveals that Equations (5.2) and (5.3) are also applicable to represent the relationship between the temperature rises obtained from different sizes of mounting. Table 5.11 shows the approximate values of geometric difference constant for the dynamic shear deformation. It can be observed that the geometric difference constants obtained from dynamic shear deformation are slightly different from those obtained from dynamic axial deformation. The results indicate that there is a small dependence of the geometric difference constant on the deformation mode.

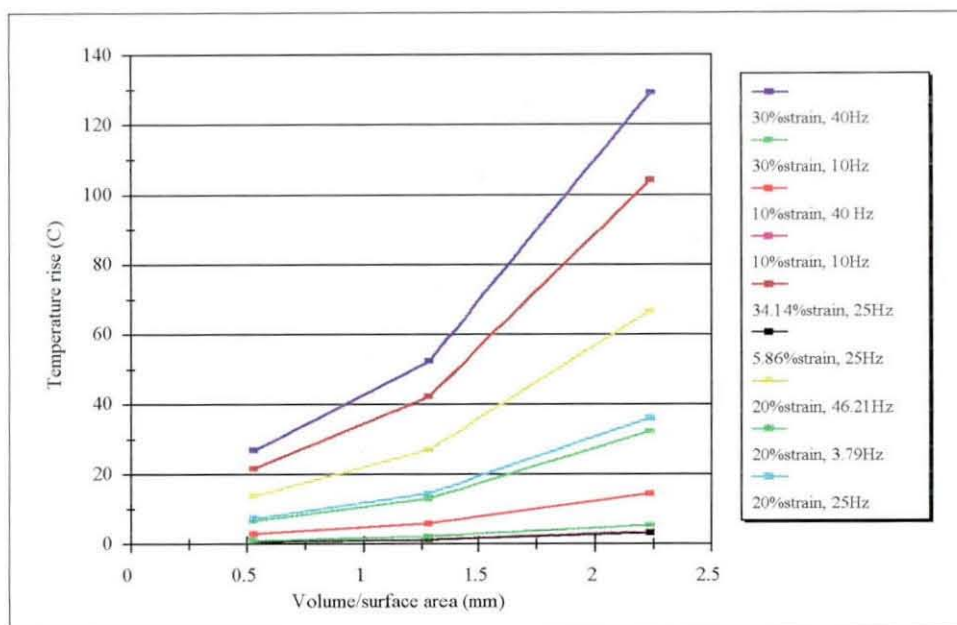
*Table 5.11* Approximate values of the geometric difference constant.

	Dynamic shear without precompression	Dynamic shear with 10% precompression
$K_{LM}$	2.47	2.46
$K_{LS}$	4.82	5.42
$K_{MS}$	1.95	2.21

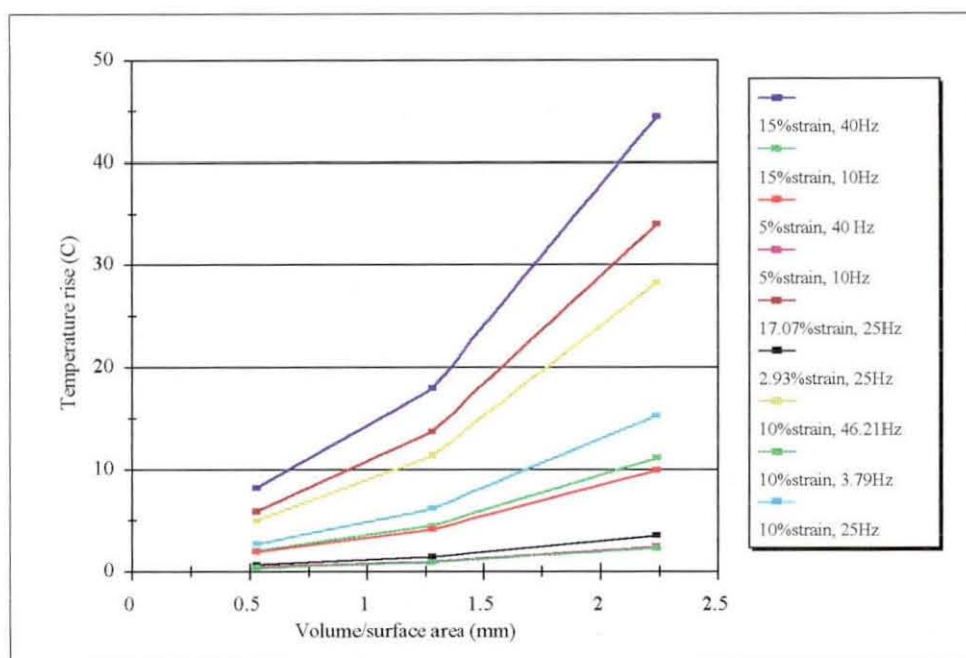
The effect of the ratio of volume to surface area on the maximum temperature rise is illustrated in Figure 5.15. Again, the results indicate that the maximum temperature rise increases continuously with increasing the ratio of volume to surface area. This confirms that the ratio of volume to surface area is one of the main factors governing the maximum temperature rise of the mountings.

**- Contour plots of the maximum temperature rise**

According to the response equations shown in Table 5.10, the influences of strain amplitude and frequency on the maximum temperature rise can be represented in the form of a contour plot as given in Figures 5.16 and 5.17 for the dynamic shear deformation without and with 10% precompression, respectively.



(a) For dynamic shear deformation without precompression



(b) For dynamic shear deformation with 10% precompression

Figure 5.15 The plots of the maximum temperature rise against the ratio of volume to surface area

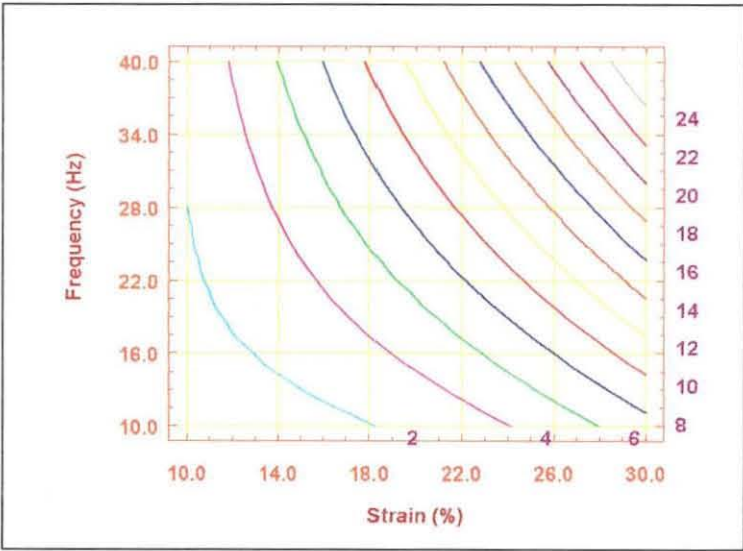


Figure 5.16 (a) The effects of strain amplitude and frequency on the maximum temperature rise ( $^{\circ}\text{C}$ ) for the small mounting subjected to dynamic shear deformation without precompression

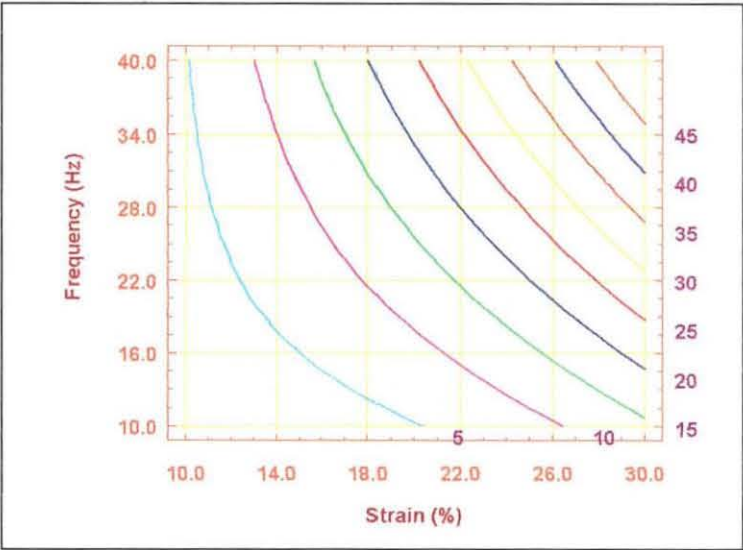


Figure 5.16 (b) The effects of strain amplitude and frequency on the maximum temperature rise ( $^{\circ}\text{C}$ ) for the medium mounting subjected to dynamic shear deformation without precompression

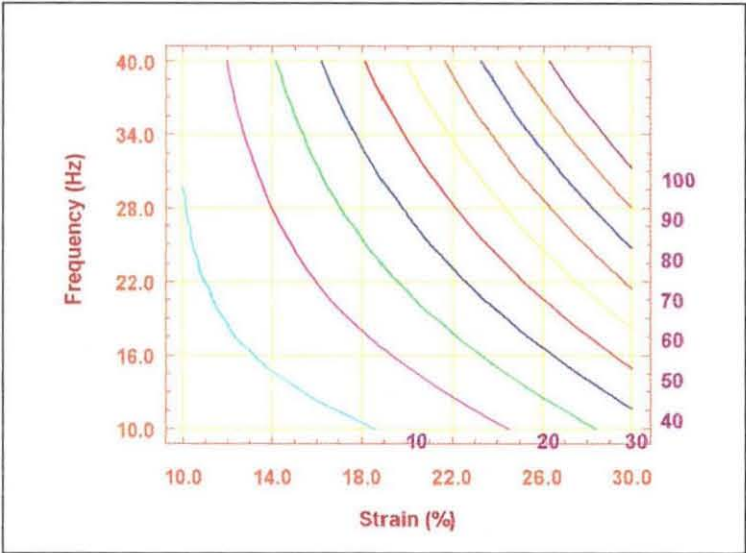


Figure 5.16 (c) The effects of strain amplitude and frequency on the maximum temperature rise ( $^{\circ}\text{C}$ ) for the large mounting subjected to dynamic shear deformation without precompression

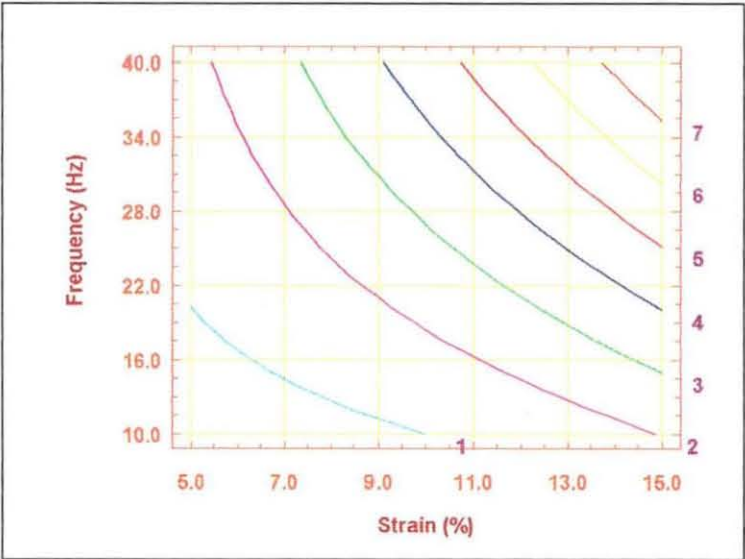


Figure 5.17 (a) The effects of strain amplitude and frequency on the maximum temperature rise ( $^{\circ}\text{C}$ ) for the small mounting subjected to dynamic shear deformation with 10% precompression

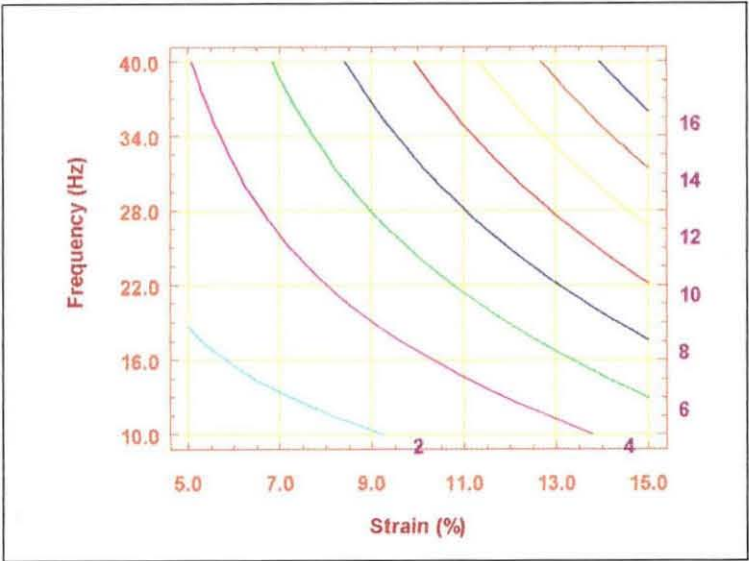


Figure 5.17 (b) The effects of strain amplitude and frequency on the maximum temperature rise ( $^{\circ}\text{C}$ ) for the medium mounting subjected to dynamic shear deformation with 10% precompression

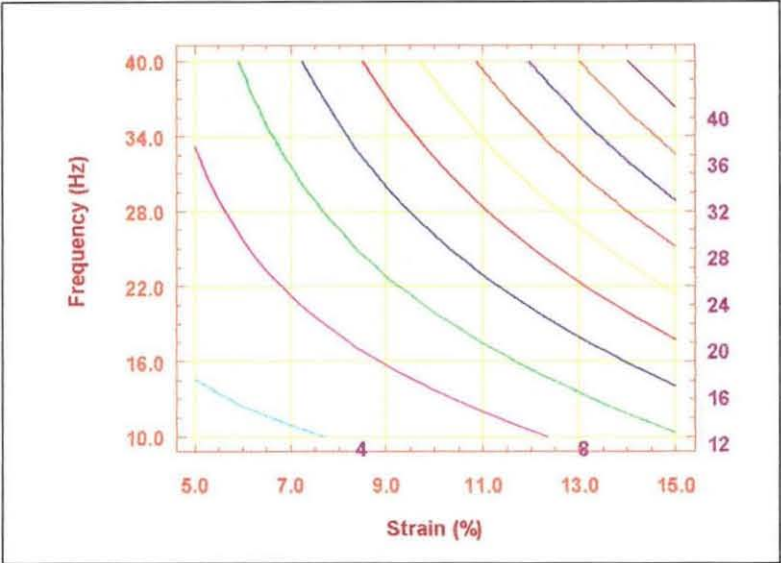


Figure 5.17 (c) The effects of strain amplitude and frequency on the maximum temperature rise ( $^{\circ}\text{C}$ ) for the large mounting subjected to dynamic shear deformation with 10% precompression

### 5.2.6 Conclusions

Taken as a whole, the results reveal that

- 1) The temperature distribution pattern is dependent on the deformation mode but independent of the test conditions.
- 2) Regardless of the effects of deformation mode, size and test condition:
  - 2.1 The maximum temperature rise is found at the centre of the mounting;
  - 2.2 Due to the “heat sink” effect, the minimum temperature rise is found at the rubber-metal interface area;
  - 2.3 The relationship between the maximum temperature rise and strain amplitude is found to be nonlinear due to the nonlinear relationship between the strain energy and the strain amplitude.
  - 2.4 The maximum temperature rise is found to be linearly related to the frequency.
- 3) The relationship between the maximum temperature rise and the test variables of the mountings subjected to dynamic axial deformation and dynamic shear deformation can be represented mathematically by the response equations, as given respectively in Tables 5.6 and 5.10.
- 4) The maximum temperature rise depends on both volume and surface area of the mounting. It is obvious that the maximum temperature rise increases as the ratio of volume to surface area is increased.



### **5.3 FEA of the Chevron spring**

#### **5.3.1 Chevron geometry**

A Chevron spring is a “V”-shaped laminated rubber mounting which is constructed by alternately stacking rubber layers and metal plates and bonding them together to form an integrated construction. Even though a wide variety of Chevron springs have been developed with different designs to suit particular service applications, only one Chevron spring, also supplied by Metalastik Ltd., was chosen for the study and its geometry is shown in Figure 5.18.

#### **5.3.2 Rubber compound**

The rubber compound used in FEA of Chevron spring was coded as “Metalastik 32053”. The physical characteristics of this compound were represented by the Mooney-Rivlin hyperelastic material model. Its material constants, hysteresis factor and heat transfer coefficient were determined by the methods described in Chapter 4.

#### **5.3.3 Problem description and experimental design**

In general, Chevron springs are used extensively in the axle-box suspension system of rail vehicles. A pair of springs are normally fitted in a vee shape (See Figure 5.19) to provide flexibility in three directions; longitudinal, lateral and vertical. An outline of deformation characteristic of the Chevron spring is shown schematically in Figure 5.20. As the Chevron springs lie at an angle  $11^\circ$  to the vertical axis, the deformation of rubber layers takes place simultaneously in shear and compression when loaded vertically.

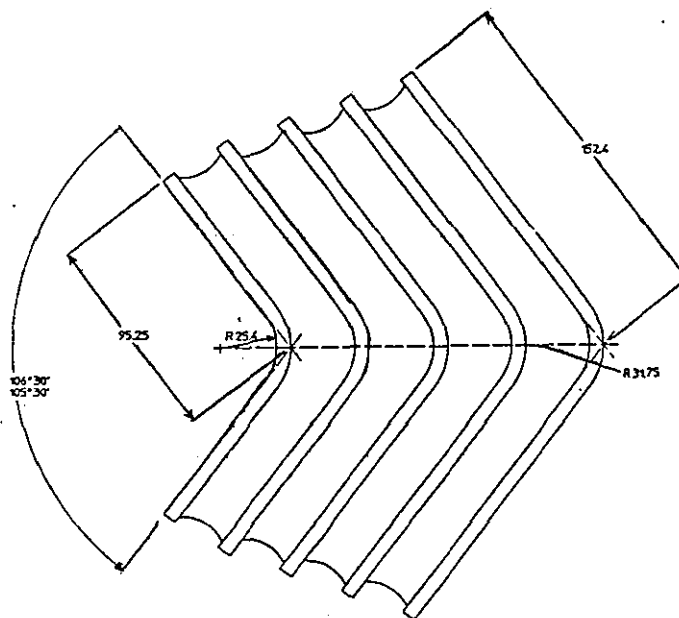
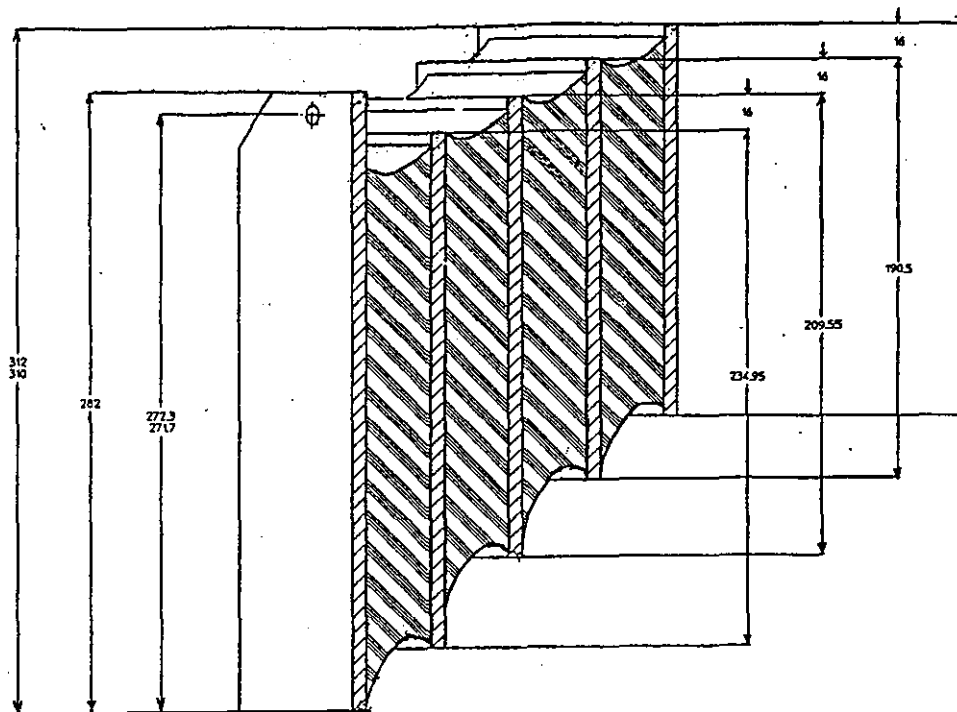


*Figure 5.18* Chevron spring geometry

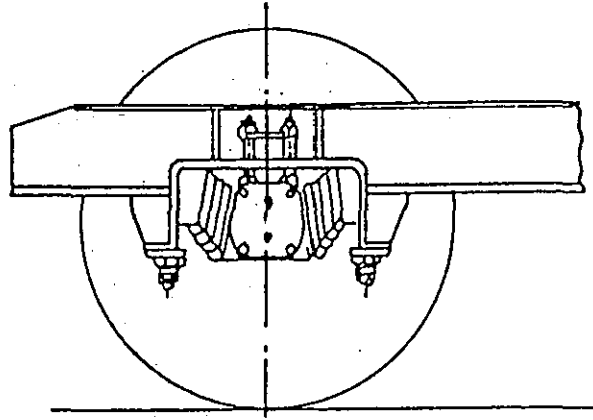


*Figure 5.19* Vee shaped fitting of Chevron springs in axle-box

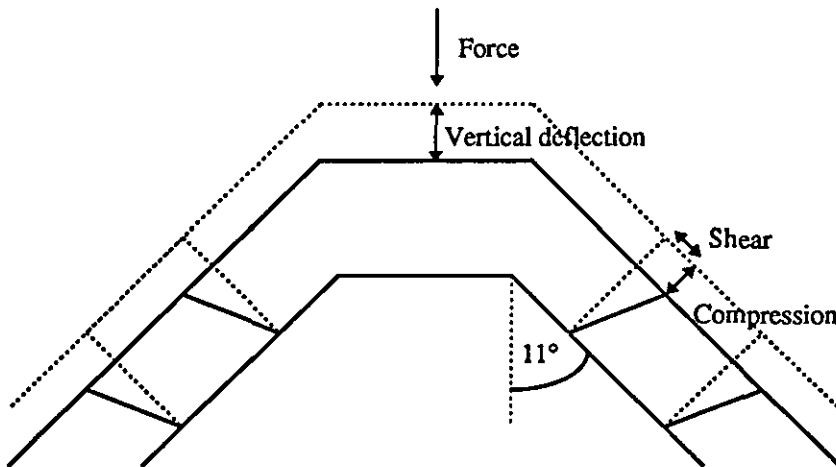


*Figure 5.20* Deformation characteristic of Chevron springs under vertical load  
(deformed shape of rubber not shown)

In the present project, the simulations were carried out based on the assumption that the spring is compressed vertically to 35 mm on which the dynamic vertical deformation is superimposed. Two deformation modes that actually take place in the rubber spring can be calculated by using basic trigonometry. According to Figure 5.20, if the vertical deflection  $A$  mm is applied, then

$$\text{shear deflection} = A \cdot \cos(11^\circ) \text{ mm}$$

$$\text{compression deflection} = A \cdot \sin(11^\circ) \text{ mm}$$

Again, the relationship between temperature rise and the two important variables (vertical deflection and frequency) was established by means of the experimental design technique. Table 5.12 represents the simulated test conditions for the Chevron spring.

*Table 5.12 Test conditions for the Chevron spring*

Problem No.	A	B	Vertical deflection (mm)	Frequency (Hz)	Note
1	+1	+1	21	2.4	Factorial point
2	+1	-1	21	0.8	Factorial point
3	-1	+1	5	2.4	Factorial point
4	-1	-1	5	0.8	Factorial point
5	+1.414	0	24.312	1.6	Star point
6	-1.414	0	1.688	1.6	Star point
7	0	+1.414	13	2.731	Star point
8	0	-1.414	13	0.469	Star point
9	0	0	13	1.6	Central point

#### 5.3.4 The FEA procedures

For the chosen Chevron spring, symmetry considerations made it possible to model and analyse only half of the spring body (See Figure 5.21).

As an example, the analysis procedures for the Chevron spring subject to 35 mm vertical pre-deflection and 21 mm dynamic vertical deflection applied on top at 2.4 Hz are listed below.

**Step (1)** An FE mesh of the spring for stress analysis was created. As the main purpose was concerned with the bulk behaviour leading to heat generation instead of the localised stress distributions, the actual contour of the fillet

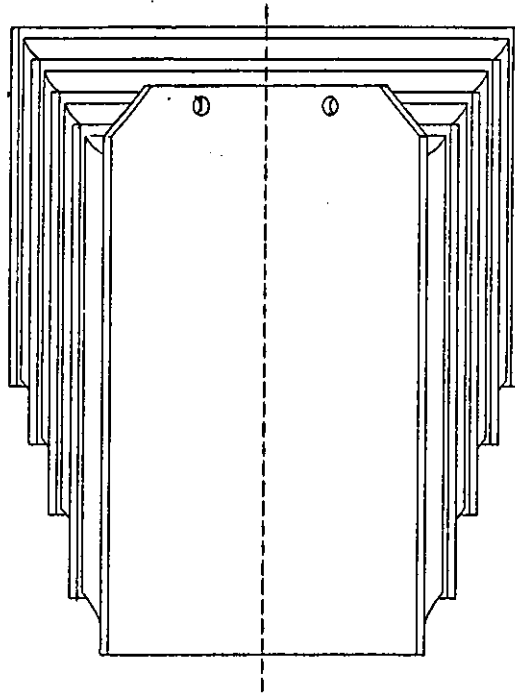


*Figure 5.21* Bottom view of Chevron spring with symmetry plane (dotted line)

edges was not important for the analysis. To simplify the modelling, the fillet edges were assumed to be flat instead of concave. Since the thickness of the metal plates was relatively thin compared with that of rubber layers, a combination of two element types was selected to represent this model; 20- node hexahedron 3D-solid elements for rubber layers and 20-node shell elements for the metal plates. Figure 5.22 shows the Chevron mesh which consists of 6 divisions along the Y-axis, 8 divisions along the Z-axis and 1 division for each layer (totally 4 layers of rubber and 5 layers of metal plates) along the X-axis. It should be noted that shell elements are not displayed in Figure 5.22 because they are represented by the defined surfaces between rubber layers; whilst the metal parts that protrude from the rubber matrix were not modelled as they have no effect on stress behaviour of rubber layers.

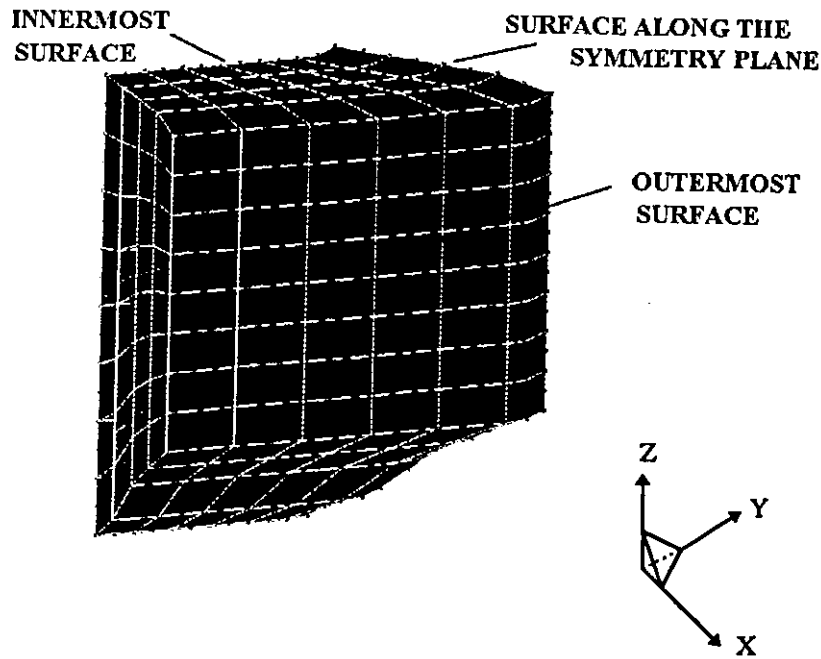


*Figure 5.22* FE mesh of Chevron spring for stress analysis

**Step (2)** Since there were three different vertical deflection levels being considered (14mm, 35mm and 56mm), three models were then created from the mesh shown above. For all models, the boundary conditions were specified in such the way that all nodes along the innermost surface were fixed not to move in any direction while those located on the symmetry plane were fixed not to move in Y-direction. However, for nodes along the outermost surface, the boundary conditions were applied differently in each model. In the first model, to simulate the 14mm vertical deflection, all nodes along this surface were set to move simultaneously in -X (compression) and -Z (shear) directions for  $14.\sin(11^\circ)$  mm and  $14.\cos(11^\circ)$  mm, respectively. Similarly, the displacement boundary condition set of  $35.\sin(11^\circ)$  mm and

35.cos(11°) mm and another set of 56.sin(11°) mm and 56.cos(11°) mm were applied respectively to the second and the third models.

Step (3) The material data (See Chapter 4) were defined as;

For rubber :  $C_{10} = 0.33 \text{ MPa}$

$C_{01} = 0.08 \text{ MPa}$

Poisson's ratio = 0.499

For metal plates : Young's modulus = 2.12E+05 MPa\*

Poisson's ratio = 0.291\*

\* Typical values for mild steel obtained from "Introduction to Engineering Materials"<sup>(118)</sup>

Step (4) Nonlinear stress analysis was then performed and the element strain energies for each model were subsequently extracted from the output file.

Step (5) The linear stress analysis was performed on these models to obtain the element volume data required for the conversion of element strain energies into element heat generation rates per unit volume. The conversion was then carried out based on the method illustrated in Appendix I.

Step (6) In this step, the FE mesh for thermal analysis was created. Unlike the mesh for stress analysis, this mesh contained only one element type (20-node hexahedron 3-D solid elements) and the metal plates were represented by two different materials: aluminium for the innermost plate and mild steel for the interleaves and the outermost plate, as shown in Figure 5.23.

Step (7) After the mesh creation was complete, the thermal boundary conditions were defined as follows.

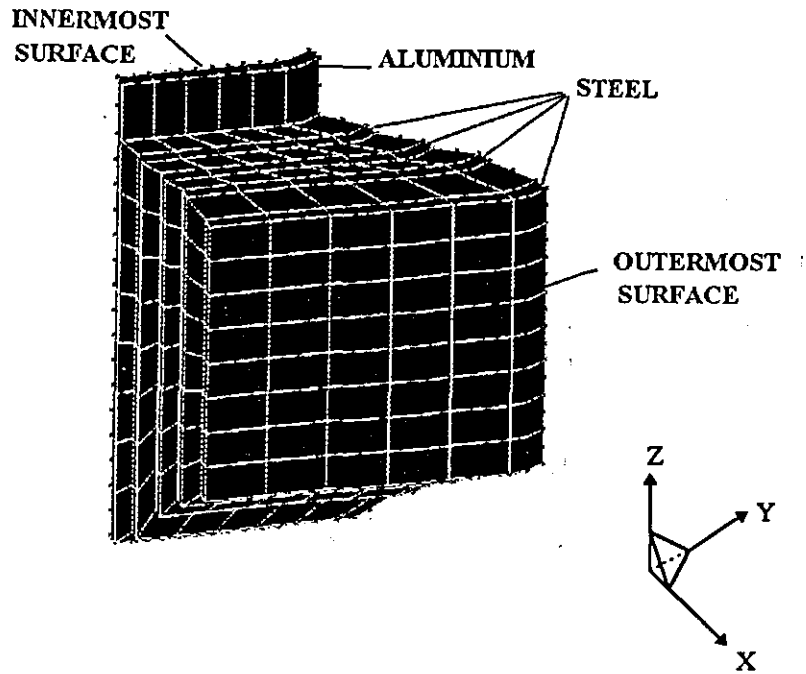


*Figure 5.23* FE mesh of Chevron spring for thermal analysis

- ◆ All nodes located on both innermost and outermost surfaces were set to remain constant at ambient temperature (20°C) throughout the analysis.
- ◆ The heat transfer coefficients of rubber “Metalastik 32053” ( $0.175\text{E-}04 \text{ W/mm}^2\text{.K}$ ), steel ( $0.097\text{E-}04 \text{ W/mm}^2\text{.K}$ ) and aluminium ( $0.095\text{E-}04 \text{ W/mm}^2\text{.K}$ ) were applied to the element faces along the outer surfaces of rubber, steel and aluminium, respectively. One thing to remember is that no heat should be allowed to transfer through the symmetry plane. As a consequence, the element faces along the symmetry plane were insulated (zero heat flux) in this case.
- ◆ Finally, the element heat generation rates obtained from step (5) were applied to the rubber elements.



Step (8) The thermal material data were defined as

For rubber : Thermal conductivity = 0.000219 W/mm.K\*

For aluminium : Thermal conductivity = 0.203 W/mm.K\*\*

For steel : Thermal conductivity = 0.05 W/mm.K\*

\* Data supplied by Metalastik Ltd.

\*\* Data obtained from "Metallic Materials"<sup>(113)</sup>

Step (9) The steady state thermal analysis was then performed in order to estimate the equilibrium running temperature of this model. Thereafter, the ambient temperature (20°C) was subtracted from the maximum equilibrium temperature to yield the maximum temperature rise.

Step (10) The above procedures were repeated with different variable sets, as previously shown in Table 5.12. Finally, the maximum temperature rise results were analysed by the "STATGRAPHICS" programme.

### 5.3.5 Results and discussion

#### - Contour characteristic of equilibrium temperature distribution

The contour plot of equilibrium temperature distribution for the Chevron spring, which is subjected to 13 mm dynamic vertical deflection at 1.6 Hz (central point), is given as an example in Figure 5.24. Similar patterns of temperature contours were also obtained for the Chevron spring subjected to different test conditions. As can be seen from Figure 5.24 (a), the maximum equilibrium temperature is found at the centre of the second rubber layer. Again, due to the presence of "heat sink" at the innermost and outermost metal plates, the minimum equilibrium temperature is found at the areas adjacent to these metal plates. It is also obvious that the temperature gradation pattern of the Chevron spring is very complicated, compared to that of the mountings. This is attributed to the

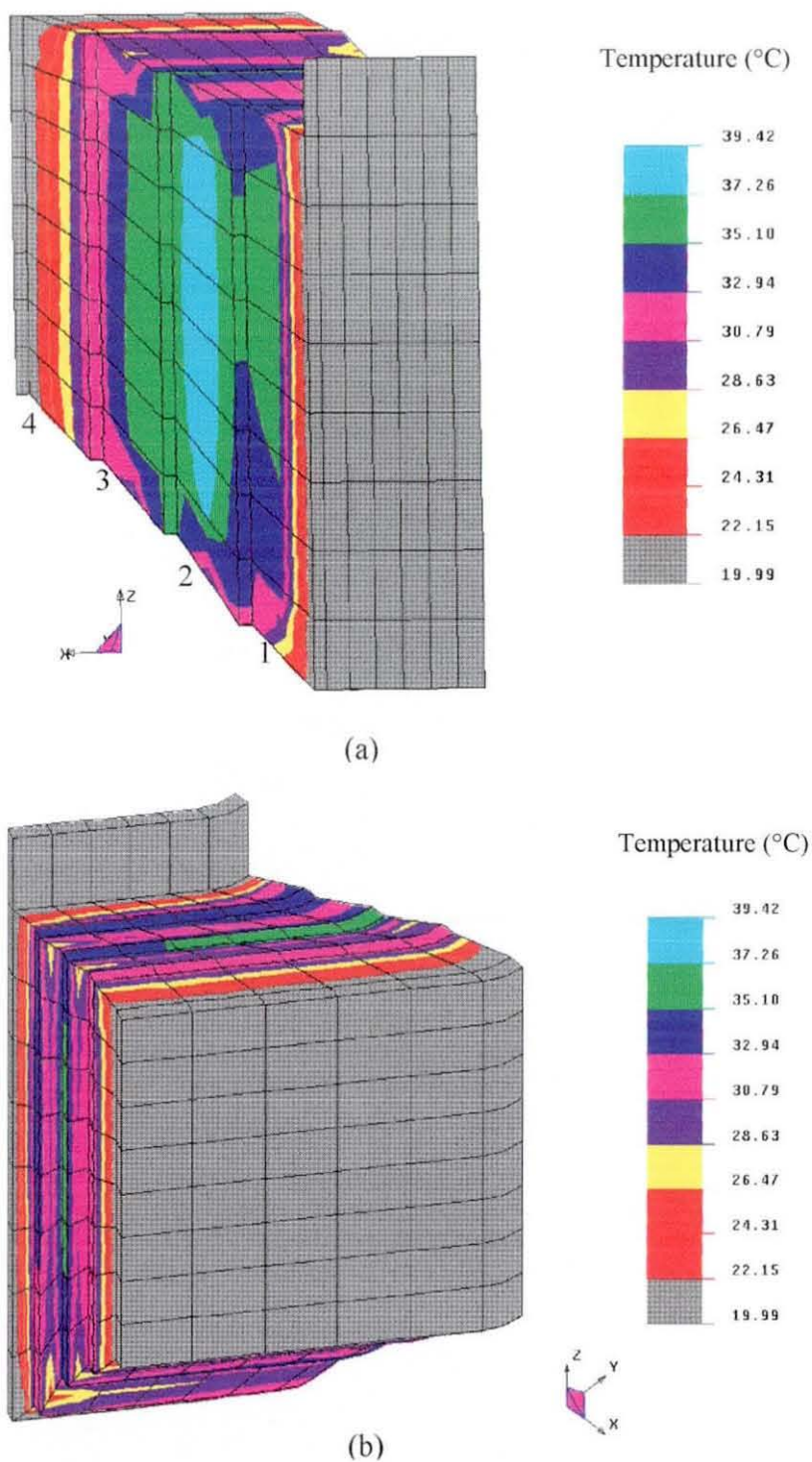


*Figure 5.24* Contour plots of equilibrium temperature distribution for the Chevron spring subjected to 35 mm pre-vertical compression and 13 mm dynamic vertical deflection applied on top at 1.6 Hz (viewed from different angles)

complexities of (i) the Chevron spring configuration, (ii) the deformation mode which is a combination of both compression and shear and (iii) the heat transfer processes taking place in the rubber component due to the metal insertions.

**- The effect of test condition on the maximum temperature rise**

Table 5.13 summarises the maximum temperature rise of the Chevron spring under various test conditions. Based on the experimental design technique, a mathematical relationship between the maximum temperature rise and the test variables (vertical deflection (d) and frequency (f)) can be established as shown below.

$$T_{\text{max.}} = 19.41 + 23.76 d + 11.52 f + 11.88 d.f + 7.26 d^2 \text{ ----- (5.4)}$$

*Table 5.13* The maximum temperature rise of the Chevron spring subjected to 35 mm pre-vertical deflection

Test condition	Maximum temperature rise (°C)
1.688mm dynamic vertical deflection at 1.6 Hz	0.3
5mm dynamic vertical deflection at 0.8 Hz	1.4
5mm dynamic vertical deflection at 2.4 Hz	4.3
13mm dynamic vertical deflection at 0.469 Hz	5.7
13mm dynamic vertical deflection at 1.6 Hz	19.4
13mm dynamic vertical deflection at 2.731 Hz	33.2
21mm dynamic vertical deflection at 0.8 Hz	25.2
21mm dynamic vertical deflection at 2.4 Hz	75.6
24.312mm dynamic vertical deflection at 1.6 Hz	67.6

The coefficient of correlation (R-squared) is found to be very high (0.996). This indicates that Equation (5.4) can be used to represent the relationship between the computed maximum temperature rise and the test variables with high accuracy. It is observable that Equation (5.4) fits very well to the “Quadratic response model”. This suggests strongly that the relationship between the maximum temperature rise and the vertical deflection is nonlinear. On the contrary, a linear relationship between the maximum temperature rise

and the test frequency is found. The interaction term indicates that the effect of varying frequency on the maximum temperature rise depends on the level of vertical deflection and vice versa. A full explanation of this behaviour was given previously in Section 5.2.5.1. Since the equation coefficients of the equation are all positive, the maximum temperature rise will increase continuously with increasing vertical deflection and/or frequency.

**- Contour plot of the maximum temperature rise**

Even though the maximum temperature rise of the Chevron spring under various test conditions can be estimated by Equation (5.4), for ease, it is common to represent the relationship between the maximum temperature rise and the test variables in terms of the contour plot, as shown in Figure 5.25.

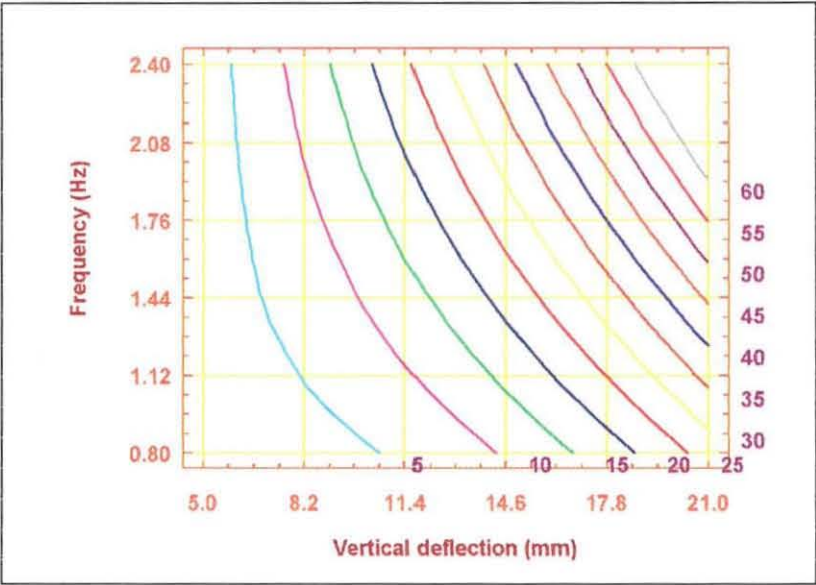


*Figure 5.25* The effects of vertical deflection and frequency on the maximum temperature rise (°C) for the Chevron spring subjected to 35 mm pre-vertical deflection

### 5.3.6 Conclusions

From the results, several conclusions can be drawn as given below.

- 1) Regardless of the test condition, the maximum temperature rise of the Chevron spring is found at the centre of the second rubber layer.
- 2) The relationship between the maximum temperature rise and the vertical deflection is found to be nonlinear whereas that between the maximum temperature rise and the frequency is found to be linear. There is also an interaction effect between the vertical deflection and frequency on the maximum temperature rise.
- 3) The mathematical relationship between the maximum temperature rise and the test variables for the Chevron spring subjected to 35mm pre-vertical deflection can be established as shown in Equation (5.4).
- 4) The maximum temperature rise increases linearly with frequency and at increasing rate with the vertical deflection.

## **CHAPTER 6**

### **EVALUATION OF FEA RESULTS**

#### **6.1 Introduction**

In general, the accuracy of any FE prediction is dependent upon how accurate the material data and environmental boundary conditions are defined. In many applications, precise material data are difficult to determine experimentally. Inaccurate data can cause significant errors. In addition, sensible assumptions are always introduced in order to simplify FE problems, provided that the accuracy of a prediction is not compromised. Whenever possible, an experimental evaluation of FE results should be made to check their accuracy.

#### **6.2 Methodology**

Measurements of the temperature rise of anti-vibration mountings and a Chevron spring were made with the co-operation of Metalastik Ltd.. All specimens were taken randomly from Metalastik production lots.

For anti-vibration mountings, the specimens were pierced centrally to make a hole through the rubber matrix. Insertion of a calibrated thermocouple wire into this hole was carried out with special care to ensure that

- i) a very good surface contact between thermocouple wire and rubber matrix was achieved and
- ii) the extreme of thermocouple wire was located at the precisely known position (See Figure 6.1), so that comparisons between experimental data and FE results could be made.

Thereafter, the prepared specimens were tested by means of a Keelavite dynamic testing machine. Figure 6.2 shows how the specimens were set into the machine. Due to some



limitations of the machine, only medium and large mountings were tested in the dynamic axial deformation mode.

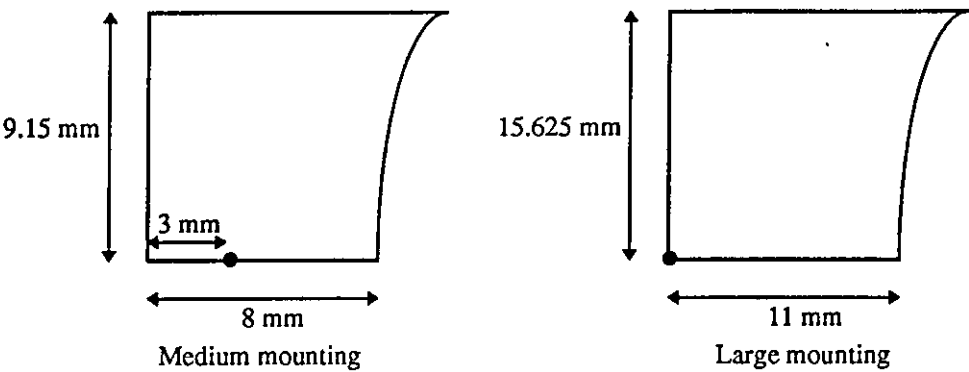


Figure 6.1 Cross-section (a quarter) of mountings representing the exact locations of thermocouple wire (• )

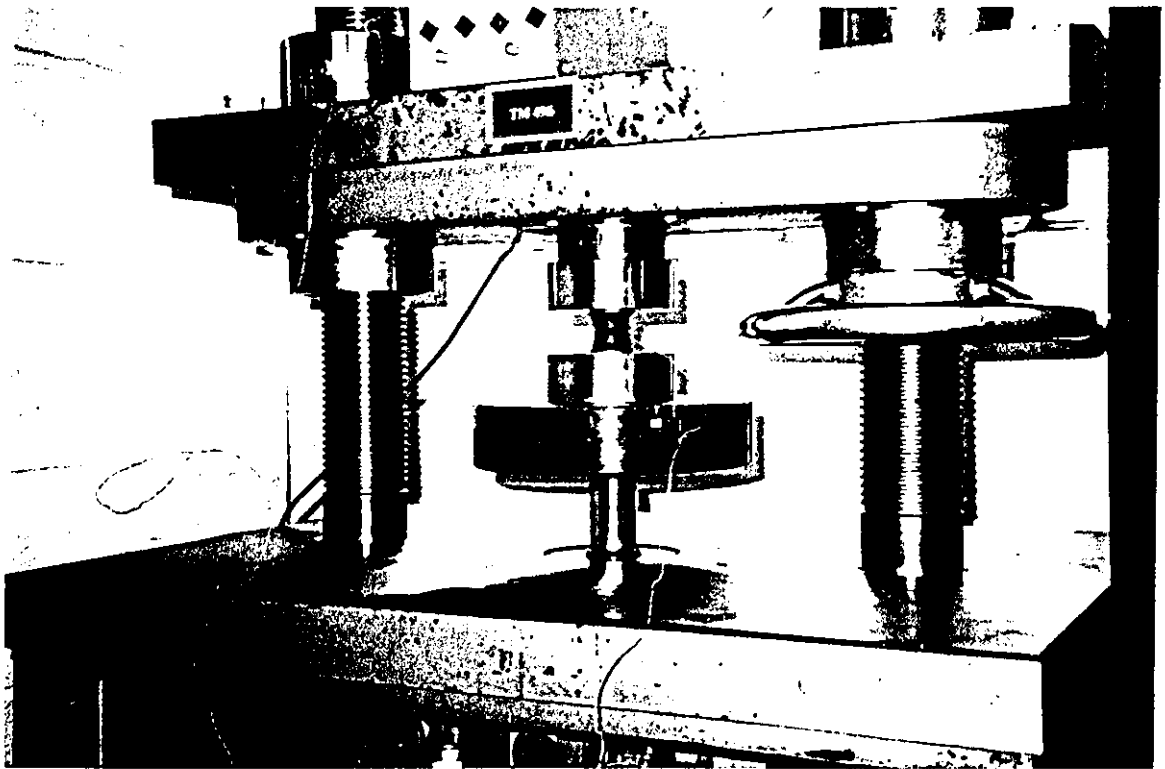
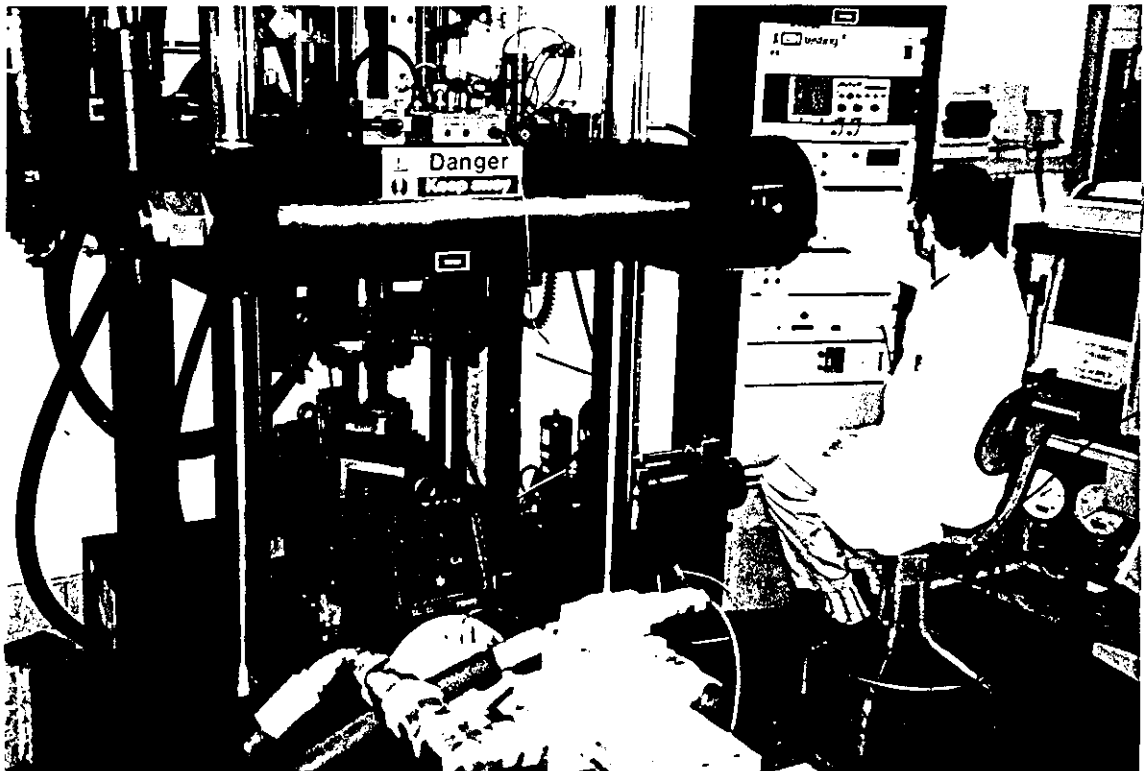


Figure 6.2 Testing machine for anti-vibration mountings

In the case of Chevron spring, a tiny hole was made through the centre of the middle steel interleaf and the testing was carried out by using a specially designed machine developed by Metalastik Ltd., and calibrated regularly by the National Measurement Accreditation Service (See Figure 6.3).

The test conditions, including the rubber compounds used for each test component, are given in Table 6.1. It should be noted that measurement of temperature rise for the Chevron spring was carried out at only one test condition due to the high cost of both the Chevron spring and the testing procedure.



*Figure 6.3* Testing machine for the Chevron spring

During each test, the running temperature was recorded continuously as a function of time (1 hour for anti-vibration mountings and 2 hours for the Chevron spring), making sure that the equilibrium temperature was reached. Subsequently, the room temperature



was subtracted from the equilibrium running temperature to yield the temperature rise at that position.

**Table 6.1** Test conditions and rubber compounds of anti-vibration mountings and the Chevron spring

Test Specimens	Compound	Deformation Modes	Test Conditions	
			Deflection levels**	Frequency
Anti-vibration Mounting (Medium)	Metalastik 19053*	Axial deformation without precompression	8 % strain	15 Hz
			10 % strain	25 Hz
			12 % strain	35 Hz
		Axial deformation with 10% precompression	3 % strain	10 Hz
			5 % strain	25 Hz
			6 % strain	30 Hz
Anti-vibration Mounting (Large)	Metalastik 19059*	Axial deformation without precompression	8 % strain	15 Hz
			10 % strain	25 Hz
			12 % strain	35 Hz
		Axial deformation with 10% precompression	3 % strain	10 Hz
			5 % strain	25 Hz
			6 % strain	30 Hz
Chevron Spring	Metalastik 32053	Vertical deformation with 35 mm pre-vertical deflection	21 mm	0.8 Hz

\* These compounds are similar to "Metalastik 19055" but differ slightly in hardness degree which are denoted by the last two figures.

\*\* Deflection levels shown are single deflection amplitudes and the strain levels given are calculated with respect to the original shapes.

Based on the test conditions shown above, FE meshes were created and analysed by the procedures described fully in Section 5.2.4 and 5.3.4 for anti-vibration mountings and a Chevron spring, respectively. Finally, comparisons of FE predictions and experimental results were made.

### 6.3 Results and Discussion

#### 6.3.1 Anti-vibration mountings

Comparisons of temperature rise obtained from FEA and experiment, for anti-vibration mountings subjected to dynamic axial deformation with 10% pre-compression, are given in Table 6.2. Results clearly show that, in all cases, good agreement between computed and experimental data is obtained, even though the computed values tend to be slightly higher than the experimental ones. This is possibly due to the fact that, in FEA, the simulations were carried out under a natural convection assumption where the air surrounding the component, which is considered as a convective medium, is stationary. However, in practice, this assumption is not held as, during dynamic deformation, the motion of the top metal bar (See also Figure 6.2) induces air flow with a certain velocity.

*Table 6.2* Temperature results for anti-vibration mountings subjected to dynamic axial deformation with 10% pre-compression

Size	Test No.	Test conditions	Temperature rise (°C)		
			Experimental	Computed	%Difference
Medium	1	3%strain, 10 Hz	0.9	0.9	0
	2	5%strain, 25 Hz	5.6	6.0	7.1
	3	6%strain, 30 Hz	9.5	10.5	10.5
Large	4	3%strain, 10 Hz	2.6	2.7	2.7
	5	5%strain, 25 Hz	15.7	16.3	3.8
	6	6%strain, 30 Hz	24.4	28.5	16.7

This motion-induced air flow promotes convective heat dissipation and, therefore, can cause an increase in the values of heat transfer coefficient ( $h$ ) of both rubber and metal plates. A reduction in the temperature rise of the rubber components will result from this effect. This mode of convection is generally known as “forced convection” because the

air motion is caused by external mechanical means.<sup>(119-121)</sup> The effect of motion-induced air flow (or forced convection) is, of course, dependent strongly on deflection amplitude of the deformation. Frequency, on the other hand, is expected to play an important role only at high deflection amplitudes.

Since the effect of forced convection was overlooked in the present project, FEA is likely to give higher values of temperature rise, compared to the experimental ones. As can be observed from Table 6.2, the % difference between experimental and computed data increases as the tests are carried out at more severe test conditions (higher strain amplitude and frequency). This is attributed to the effect of forced convection which becomes more important as the deflection amplitude and frequency of the tests are increased. However, since all tests shown in Table 6.2 were carried out at relatively low strain amplitudes in which the effect of forced convection is not very pronounced, FEA provides good predictions of temperature rise in the components.

**Table 6.3** Temperature results for anti-vibration mountings subjected to dynamic axial deformation without pre-compression

Size	Test No.	Test conditions	Temperature rise (°C)		
			Experimental	Computed	%Difference
Medium	1	8%strain, 15 Hz	6.5	7.0	7.7
	2	10%strain, 25 Hz	14.5	18.3	26.2
	3	12%strain, 35 Hz	25.5	37.1	45.5
Large	4	8%strain, 15 Hz	19.0	18.7	1.5
	5	10%strain, 25 Hz	36.2	48.9	35.1
	6	12%strain, 35 Hz	54.8	98.8	80.3

As the strain amplitude is increased, the motion-induced air flow becomes an important factor governing heat dissipation rate of the components and cannot be simply ignored in the modelling. This can be seen from the temperature results for anti-vibration mountings

subjected to dynamic axial deformation without precompression but higher strains (See Table 6.3). Although FE results agree quite well with the experimental results for tests carried out at 8% strain and 15 Hz (test No. 1 and 4), FEA fails to provide a good prediction of temperature rise at more severe test conditions (test No. 2,3,5 and 6). In this case, the computed temperature rise is found to be considerably higher than the experimental one, with a % difference of up to 80.3%. This failure is believed to occur because the effect of forced convection is not taken into account in the modelling.

To show the significance of the effect of forced convection on temperature rise, FE problems for test No. 2,3,5 and 6 (in Table 6.3) were reanalysed by using the modified values of convective heat transfer coefficient to override the effect of forced convection. Modification of heat transfer coefficient is done by the following procedure. Based on data published by Gehman<sup>(85)</sup>, heat transfer coefficient for air flow parallel to flat surface has been found to be linearly related to the air speed, and the correlation can be expressed mathematically by

$$h_v = (1 + \frac{V}{1.5}) h_0 \quad \text{----- (6.1)}$$

where  $h_0$  = natural convective heat transfer coefficient (air speed = 0 m/s)

$h_v$  = forced convective heat transfer coefficient (air speed = V m/s)

According to Equation (6.1), measurement of air speed (V) flowing parallel to component surface must be undertaken to calculate the accurate value of heat transfer coefficient. This is practically impossible in this case because the direction of air flow caused by metal bar motion is not uniform. However, since the aim of this section is to give a general idea of how much the forced convection can affect the temperature rise, for simplicity, the air surrounding the mounting is assumed to flow uniformly with the same speed as the metal bar. The speed of metal bar can be calculated by the following equation;

$$V = 4 Af \quad \text{----- (6.2)}$$

where  $A$  = deflection amplitude (m)

$f$  = frequency ( $s^{-1}$ )

The calculated air speeds as well as the approximate values of heat transfer coefficient obtained from Equation (6.1) under particular test conditions are shown in Table 6.4. Also given in the table are values of experimental temperature rise and the computed temperature rise obtained by using the modified heat transfer coefficients. As can be seen, the values of computed temperature rise are reduced markedly to approach those of the experimental temperature rise, as the values of heat transfer coefficient are modified. The results suggest strongly that the effect of forced convection is important in these particular cases and must be taken into considerations in the modelling.

*Table 6.4* Temperature results for anti-vibration mountings analysed with the modified values of heat transfer coefficient ( $h_v$ )

Size	Test conditions	Air speed (m/s)	$h_v$	Temperature rise ( $^{\circ}C$ )		
				Experimental	Computed	%Difference
Medium	10%strain, 25 Hz	1.83	$2.22h_0$	14.5	15.1	4.1
	12%strain, 35 Hz	3.07	$3.05h_0$	25.5	28.5	11.8
Large	10%strain, 25 Hz	3.13	$3.09h_0$	36.2	37.9	4.7
	12%strain, 35 Hz	5.25	$4.50h_0$	54.8	71.5	30.5

In addition to the effect of forced convection, a small error can be introduced as a result of the following assumptions which have been made previously to simplify the modelling.

- i) In Section 4.4, the true Young's modulus of the compound is assumed to be independent of temperature, despite the fact that it decreases gradually with increasing temperature (See also Figure 4.6).
- ii) In Section 4.5, the hysteresis factor is assumed to be constant, regardless of the strain amplitude effect. A single mid-range value of hysteresis factor is, therefore, selected and used in FEA (See also Figures 4.8 and 4.9).

According to these assumptions, an error can take place as explained below. At low strain amplitudes, the value of hysteresis factor used in the modelling is slightly less than the actual value. It is therefore expected that the computed temperature rise should be slightly lower than the experimental one. In the meantime, increasing of temperature during the test results in a gradual reduction in the true Young's modulus and, hence, the heat generation rate. This gives rise to a small reduction of the experimental temperature rise. Since the consequences obtained from these two assumptions are counterbalanced, the degree of error introduced is thought to be very small. At higher strain amplitudes, the effect of the latter assumption is less pronounced, as the actual value of hysteresis factor approaches the value used in the modelling. On the contrary, a dramatic increase in temperature during the test makes the effect of the former assumption become more pronounced. As a consequence, the experimental temperature rise is expected to be slightly lower than the computed one. However, since the true Young's modulus of the compound is found to decrease only about 10% over the tested temperature range (20°C -100°C), the error caused by these two assumptions is considered to be small in comparison with that caused by the forced convection.

Another source of heat dissipation that was not taken into account in the modelling is heat radiation. Although, in actual problems, heat can be dissipated from rubber surface to the surroundings by radiation, the heat dissipation rate by this process is considerably less than that by conduction or convection. Let us consider a rubber body at

temperature  $T$  placed firmly in between two huge metal bars the temperatures of which remain constant at ambient temperature ( $23^{\circ}\text{C}$ ) as shown in Figure 6.4. Approximate values of heat transfer rate per unit area by conduction (rubber-metal interface), convection (rubber-air interface) and radiation can then be calculated by Equations (2.74), (2.76) and (2.77), respectively.

The ratios of the calculated heat transfer rate per unit area by conduction ( $Q_{cd}$ ), natural convection ( $Q_{cv}$ ) and radiation ( $Q_{rd}$ ) as a function of temperature difference, for rubber compound “Metalastik 19055” (approximate value of emissivity ( $\epsilon$ ) =  $0.9^{(85)}$ ), are given in Table 6.5. Apparently, heat conduction between rubber-metal interface is the main

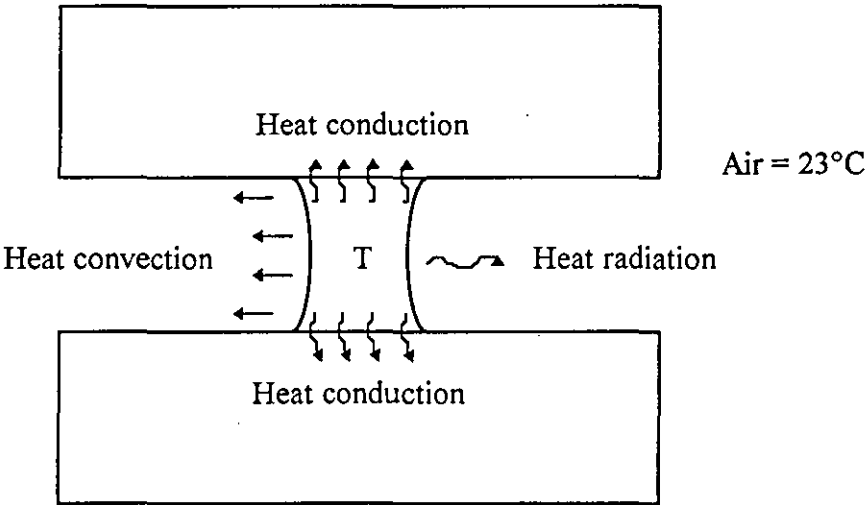


*Figure 6.4* Heat dissipation processes of rubber body placed firmly between two huge metal bars

source of heat dissipation process in this case. In comparison with heat radiation, heat convection also plays an important role on heat dissipation process. The effect of heat convection will become even more important when forced convection takes place, because it increases markedly the value of heat transfer coefficient and, hence, the heat convection rate.

Even though heat radiation is more pronounced as the temperature difference is increased, its effect on temperature change is considered insignificant in many engineering applications where heat dissipation is primarily based on heat conduction and convection. Consequently, the effect of heat radiation can be ignored without any serious error in this case.

*Table 6.5* The ratios of heat transfer rate per unit area (*Q*) by three different processes: conduction (*Q<sub>cd</sub>*), natural convection (*Q<sub>cv</sub>*) and radiation (*Q<sub>rd</sub>*)

Temperature difference ( $\Delta T$ )	$Q_{cd} / Q_{cv} / Q_{rd}$
5	41.4 / 3.2 / 1
10	40.4 / 3.1 / 1
20	38.4 / 3.0 / 1
30	36.6 / 2.8 / 1
50	33.1 / 2.6 / 1
80	28.7 / 2.2 / 1

One other source of error is concerned with frictional heat. Since the thermocouple wire was inserted into the rubber matrix prior to the dynamic deformation, the friction between rubber matrix and thermocouple wire is likely to cause localised temperature rise in the components. However, as the thermocouple wire is very small (0.5 mm diameter), the amount of heat generation caused by friction is thought to be insignificant, compared to that caused by hysteresis. As a consequence, the effect of frictional heat was not considered during the temperature measurements. Nevertheless, if a very precise value of temperature rise caused solely by hysteresis is required, an amendment in experimental procedures must be made to eliminate the effect of frictional heat.

It is also of importance to point out another reason why the measured temperature rise is generally less than that predicted. Since the thermal conductivity of the thermocouple



wire is high compared to that of the rubber, heat conduction along the thermocouple wire will distort the temperature contours, giving rise to a reduced temperature at the thermocouple tip. However, as thermocouple wire used in this project is very fine, this source of error is not pronounced and can be considered insignificant.

Finally, since the accuracy of the FEA solution depends strongly on the accuracy of the input data, it is interesting to determine the effect of variation in the value of thermal conductivity on the maximum temperature rise. Attempts, therefore, have been made to reanalyse the finite element problem for the large mounting subjected to 12% strain at 35 Hz. The modified value of heat transfer coefficient (see Table 6.4) was employed. The value of thermal conductivity was varied from 1.80E-04 to 2.70E-04 W/mm.K ( $\pm 20\%$  from original value). Table 6.6 illustrates the influence of changing the value of thermal conductivity on the maximum temperature rise. Apparently, the maximum temperature rise is fairly sensitive to the variation in the value of thermal conductivity as it is found that the maximum temperature rise decreases with increasing thermal conductivity. Consequently, it can be said that an error in the prediction of the maximum temperature rise might arise due to inaccurate input data, particularly the value of thermal conductivity. However, examination of value of thermal conductivity in the literature and comparison of experiments with prediction in the work reported here suggest that the value of 2.25E-04 W/mm.K is appropriate for the rubber compound investigated.

*Table 6.6*    The effect of variation in the thermal conductivity on the maximum temperature rise

Thermal conductivity (x10 <sup>-4</sup> W/mm.K)	Maximum temperature rise (°C)
1.80	86.2
2.02	78.2
2.25	71.5
2.48	66.0
2.70	61.6

### **6.3.2 Chevron spring**

The temperature rise of the Chevron spring obtained from measurement and computation is found to be 17.0°C and 20.1°C, respectively. Again, the computed temperature rise is higher than the measured one (with 18.8% difference in this case). As in the case of the anti-vibration mountings, the main source of error in the modelling is attributed to the effect of forced convection. In addition, in the modelling, parts of steel interleaves that protrude from rubber matrix were ignored. Since these parts are likely to promote somewhat the heat dissipation process, particularly heat convection, due to an increase in surface area, it can be expected that the temperature rise obtained from FEA should be slightly higher than that from the measurement. Despite these two sources of error, FEA still provides an acceptable prediction of temperature rise for Chevron spring. However, it should be borne in mind that, to use FEA for temperature rise prediction at higher strain amplitude or frequency, the effect of forced convection must be taken into account.

Another important point, which can be drawn from the results, is concerned with the assumption made earlier in Section 4.6.3. In this assumption, the effect of geometric factor on heat transfer coefficient is disregarded in order to simplify the modelling work. Since good agreement between experimental and computed data is obtained while certain error is brought about mainly by the two factors mentioned above, this is an indication that the error introduced by this assumption is very small and can be ignored.

## **6.4 Conclusions**

In summary, the results show that:

1. FEA gives a good prediction of temperature rise for both anti-vibration mountings and Chevron spring, provided that the effect of forced convection is not very pronounced. On the contrary, when the effect of forced convection comes into play,

FEA based on natural convection fails to provide a sensible prediction. This is the case in which modification of natural convective heat transfer coefficients ( $h_0$ ) is needed.

2. Other possible sources of error in the modelling, for instance, heat radiation, frictional heat, etc., are insignificant and negligible, compared to the effect of forced convection.

## **CHAPTER 7**

### **OVERALL CONCLUSION AND RECOMMENDATIONS**

#### **7.1 Overall Conclusion**

Taken as a whole, the present work has shown that FEA can be used, in association with some additional calculation procedure, to predict the internal temperature rise of rubber components. The additional calculation was needed to estimate the energy dissipation due to hysteresis, since FEA is capable only of analysing hyperelastic problems. To use FEA for this purpose, some essential parameters such as the Mooney-Rivlin material constants, hysteresis factor, thermal conductivity and heat transfer coefficient are required. Experimental determinations of such parameters have given some important conclusions as listed below.

1. The elastic behaviour of the rubber compounds is perfectly linear throughout the measured range and, therefore, it can be represented by a single parameter, the true Young's modulus. The Mooney-Rivlin material constants can then be characterised by using the theory "constant true Young's modulus with varying Poisson's ratio".
2. Determination of hysteresis factor reveals that, within the tested ranges of strain amplitude (0.04-0.4), frequency (0.1-10 Hz) and temperature (21°-100°C), their influences on the hysteresis factors of both NR and IR compounds can be disregarded for practical design purpose.
3. The heat transfer coefficients for natural convection can be determined by using FEA based on the results obtained experimentally from the measurement of temperature changes at any point in the specimen as a function of time.

The application of FEA in predicting the internal temperature rise of the rubber components has shown that, for both anti-vibration mountings of approximately

cylindrical geometry and a Chevron spring, the relationship between the maximum temperature rise and the two test variables (strain amplitude and frequency) can be expressed mathematically by a “quadratic response model” in which the frequency squared term is statistically insignificant. This means that the maximum temperature rise is nonlinearly related to the strain amplitude but linearly related to the frequency. There is also an interaction between the effects of strain amplitude and frequency on the maximum temperature rise. For instance, it is found that the maximum temperature rise increases linearly with frequency but at increasing rate as the strain amplitude is increased. It is also evident that, for anti-vibration mountings, the maximum temperature rise is dependent on both volume and surface area of the mounting. Obviously, the maximum temperature rise is found to increase with the ratio of volume to surface area.

Comparisons of the maximum temperature rises obtained from the measurements and FEA reveal that FEA is capable of predicting the internal temperature rise of rubber components with high accuracy, provided that both material data and environmental boundary conditions are accurately defined. The major source of error found in this work is attributed to the effect of forced convection, due to local air disturbance by the test machine motion, which becomes more pronounced at high amplitudes and frequencies

## **7.2 Recommendations for Further Work**

1. In the modelling work (Chapter 5), all FE models were analysed with the values of heat transfer coefficient corresponding to the natural convection assumption. It was observed that the computed temperature rise is higher than the experimental one, particularly at severe test conditions. To reduce the error introduced by this assumption, it is recommended that the FE models should be reanalysed with the modified values of heat transfer coefficient in which the effect of forced convection is taken into consideration.

2. It would also be interesting to study the effect of varying the precompression on the internal temperature rise of rubber mountings.
3. The main scope for further work is in mapping the changes in critical tearing energy ( $T_c$ ) due to the temperature distribution and in predicting the fatigue resistance or service life based on the critical tearing energy distribution.

## APPENDIX I

### CONVERSION OF STRAIN ENERGY INTO HEAT GENERATION RATE

As previously mentioned in Section 2.3, when a stress is applied to rubber, the strain does not take place correspondingly to this stress. In fact, the strain always lags behind the stress, resulting in the phase difference ( $\delta$ ) which is of practical importance in a rapid dynamic deformation. When force and deflection or stress and strain are plotted against each other, they produce a “hysteresis loop”. If the stress and strain cycles are sinusoidal and the rubber characteristics are linear, this loop is fully elliptic as shown in Figure A.1.1.

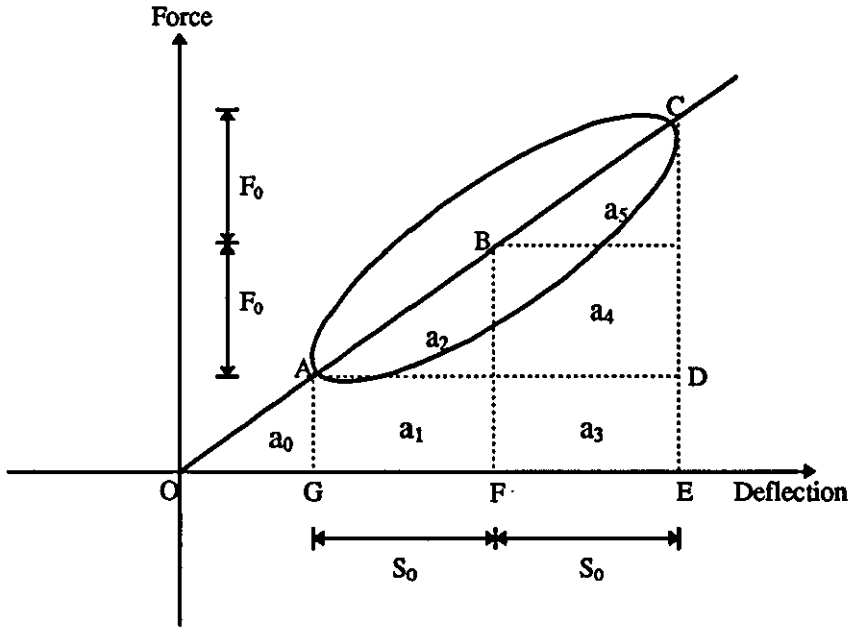


*Figure A.1.1* Hysteresis loop in dynamic stress/strain cycles

The amount of energy loss per cycle is represented by the area of the ellipse which is;

$$E_{\text{loss}} = \pi F_0 S_0 \sin(\delta) \quad \text{----- (A.1.1)}$$

$$\text{or} \quad E_{\text{loss}} = \pi \sigma_0 \epsilon_0 \sin(\delta) \quad \text{----- (A.1.2)}$$

where  $F_0$  and  $\sigma_0$  are force amplitude and stress amplitude, and

$S_0$  and  $\epsilon_0$  are deflection amplitude and strain amplitude.

Obviously, Equation (A.1.1) gives the total energy loss in the piece of rubber whereas Equation (A.1.2) gives the energy loss per unit volume of rubber. Alternatively, the energy loss can be represented as;

$$E_{\text{loss}} = 1/2 \pi \sin(\delta) (\text{area ACD}) \quad \text{----- (A.1.3)}$$

Equation (A.1.3) is identical to Equation (A.1.1) as area ACD can be expressed as;

$$\text{area ACD} = 1/2 (2F_0) (2S_0) = 2 F_0 S_0$$

Based on Equation (A.1.3), to obtain the energy loss, the area ACD must be pre-determined. This can be done if the elastic strain energies (E) of the rubber at points A, B and C are known as it is evident that

$$\text{area ACD} = 2 [(E_C - E_B) - (E_B - E_A)] \quad \text{----- (A.1.4)}$$

A validation of Equation (A.1.4) is given below. As can be seen from Figure A.1.1, the elastic strain energies at points A, B and C can be represented by

$$E_A = \text{area OAG} = a_0 \quad \text{----- (A.1.5)}$$

$$E_B = \text{area OBF} = a_0 + a_1 + a_2 \quad \text{----- (A.1.6)}$$

$$E_C = \text{area OCE} = a_0 + a_1 + a_2 + a_3 + a_4 + a_5 \quad \text{----- (A.1.7)}$$

Substitution of Equations (A.1.5), (A.1.6) and (A.1.7) into Equation (A.1.4) yields

$$\begin{aligned} 2 [(E_C - E_B) - (E_B - E_A)] &= 2 [(a_3 + a_4 + a_5) - (a_1 + a_2)] \\ &= 2 a_4 \quad (\text{as } a_1 = a_3 \text{ and } a_2 = a_5) \\ &= a_4 + a_2 + a_5 \quad (\text{as } a_2 = a_5 = \frac{1}{2} a_4) \\ &= \text{area ACD} \end{aligned}$$

Therefore, Equation (A.1.4) is proved to be valid. By substituting Equation (A.1.4) into Equation (A.1.3), the energy loss then becomes;

$$E_{\text{loss}} = \pi \sin(\delta) [(E_C - E_B) - (E_B - E_A)] \quad \text{----- (A.1.8)}$$



As heat generation rate (H) required in thermal analysis must be in terms of energy loss rate per unit volume of rubber, the energy loss obtained must be converted further by the following equations;

$$H = \frac{E_{\text{loss}} \times f}{V} \quad \text{----- (A.1.9)}$$

or 
$$H = \frac{\pi \sin(\delta) [(E_C - E_B) - (E_B - E_A)] \times f}{V} \quad \text{----- (A.1.10)}$$

where  $f$  = frequency

$V$  = volume of rubber

According to equation (A.1.10), the heat generation rate can be easily calculated if the strain energies at points A, B and C are obtained.

In this study, the element strain energies at points A, B and C were obtained from the FE nonlinear stress analysis, while the element volume data were extracted from the FE linear stress analysis results. Frequency was the known parameter and the lag angle ( $\delta$ ) for each compound was pre-determined by the procedure previously described in Chapter 4.

### Units used in this project

Throughout this work, the elastic constants or stresses were in MPa and the dimensions of the components denoted were in mm. Therefore the elastic strain energy per element was in MPa.mm<sup>3</sup> = N.mm = mJ (as 1 Pa = 1 N/m<sup>2</sup> and 1 N.m = 1 J). The energy loss obtained would also be in units of mJ. As the frequency of deformation was in Hz, the heat generation rate per unit volume of rubber obtained from equation (A.1.10) will be in mJ/sec.mm<sup>3</sup> = mW/mm<sup>3</sup> (as J/sec = W).

In steady state thermal analysis, the units of thermal conductivity were in W/mm.K, the required heat generation rate per unit volume, therefore, must be in W/mm<sup>3</sup>. This means that the equation actually employed in this project is as given below.

$$* * * \quad H = \frac{\pi \sin(\delta) [(E_C - E_B) - (E_B - E_A)] \times f \times 10^{-3}}{V} \quad * * *$$

## REFERENCES

- (1) A.S.E. Ahmed, "Finite Element Software and Applications", Ph.D Thesis, Loughborough University of Technology, 1987.
- (2) D.W. Nicholson and N.W. Nelson, *Rubber Chem. Technol.* **63**, 368 (1990).
- (3) C.S. Desai and J.F. Abel, "Introduction to the Finite Element Method", Van Nostrand Reinhold, 1972.
- (4) O.C. Zienkiewicz and R.L. Taylor, "The Finite Element Method", Fourth Edition, McGraw-Hill, 1975.
- (5) R.H. Gallagher, "Finite Element Analysis Fundamentals", Plentice-Hall, 1975.
- (6) H.C. Martin and G.F. Carey, "Introduction to Finite Element Analysis", McGraw-Hill, 1973.
- (7) K.C. Rockey, H.R. Evans, D.W. Griffiths and D.A. Nethercot, "The Finite Element Method", Granada Publishing, 1975.
- (8) J.N. Reddy, "An Introduction to the Finite Element Method", Second Edition, McGraw-Hill, 1993.
- (9) K.N. Morman and T.Y. Pan, *Machine Design* **60**, October 20, 107 (1988).
- (10) K.N. Morman and T.Y. Pan, *Rubber Chem. Technol.* **61**, 503 (1988).
- (11) R.H. Finney and A. Kumar, *Rubber. Chem. Technol.* **61**, 879 (1988).
- (12) R.W. Ogden, *Proc. R. Soc. London, Series A-328*, 567 (1972).
- (13) T.J. Peng and R.F. Landel, *J. Appl. Phys.* **46**, 2599 (1975).
- (14) T.J. Peng and R.F. Landel, *J. Appl. Phys.* **43**, 3064 (1972).
- (15) D.J. Charlton, J. Yang and K.K. The, *Rubber Chem. Technol.* **67**, 481 (1994).
- (16) R.S. Rivlin, *Philos. Trans. R. Soc. London A* **241**, 379 (1948).
- (17) M. Mooney, *J. Appl. Phys.* **11**, 582 (1940).
- (18) G. Medri, *Plastics and Rubber Processing and Applications* **9**, 47 (1988).
- (19) N.W. Tschogel, *Rubber Chem. Technol.* **45**, 60 (1972).
- (20) J.L. Sullivan, K.N. Morman and R.A. Pett, *Rubber Chem. Technol.* **53**, 805 (1980).

- (21) A.N. Gent and A.G. Thomas, *J. Polym. Sci.* **28**, 625 (1958).
- (22) O.H. Yeoh, *Rubber Chem. Technol.* **63**, 792 (1990).
- (23) O.H. Yeoh, *Rubber Chem. Technol.* **66**, 754 (1993).
- (24) R.W. Ogden, *Rubber Chem. Technol.* **59**, 361 (1986).
- (25) K.C. Valanis and R.F. Landel, *J. Appl. Phys.* **38**, 2997 (1967).
- (26) J.T. Oden, "Finite Elements of Nonlinear Continua", McGraw-Hill, 1972.
- (27) I. Fried and A.R. Johnson, *Comput. Methods Appl. Mech. Eng.* **87**, 241 (1988).
- (28) E.D. George, C.A. Haduch and S. Jordan, *Finite Element Anal. Des.* **4**, 19 (1988).
- (29) R.H. Finney, *Machine Design* **58**, May 22, 87 (1986).
- (30) L. Mullins, *J. Appl. Polym. Sci.* **6**, 257 (1959).
- (31) R.S. Rivlin and D.W. Saunders, *Phil. Trans. R. Soc. London*, **A243**, 251 (1951).
- (32) Y. Obata, S. Kawabata and H. Kawai, *J. Polym. Sci.* **8**, Part A2, 903 (1970).
- (33) W. Seki, Y. Fukahori, Y. Iseda and T. Matsunaga, *Rubber Chem. Technol.* **60**, 856 (1987).
- (34) M.J. Gregory, *Plast. Rubber. Mater. Appl.* **4**, Nov., 184 (1979).
- (35) C.K.L. Davies, Dilip K. De and A.G. Thomas, *Rubber Chem. Technol.* **67**, 716 (1994).
- (36) Y. Fukahori and W. Seki, *Journal of Material Science* **28**, 4143 (1993).
- (37) Y. Fukahori and W. Seki, *Journal of Material Science* **28**, 4471 (1993).
- (38) W.V. Chang and S.C. Sun, *Rubber Chem. Technol.* **64**, 202 (1991).
- (39) K.W. Dalgarno, A.J. Day and T.H.C. Childs, *Proc Instn. Mech. Engrs.* **207**, Part D : *Journal of Automobile Engineering*, 145 (1993).
- (40) M. Takayama, H. Tada and R. Tanaka, *Rubber Chem. Technol.* **65**, 46 (1992).
- (41) P.B. Lindley, *J Strain Analysis* **6**, 45 (1971).
- (42) P.B. Lindley, *J Strain Analysis* **10**, 25 (1975).
- (43) F. Tabaddor, *Computers & Structures* **26**, 33 (1987).
- (44) G. Medri, A. Strozzi, J.C.M. Bras and A. Gabelli, *Plastics and Rubber Processing and Applications* **5**, 133 (1985).

- (45) K. Cho, A.N. Gent and P.S. Lam, *Journal of Material Science* **22**, 2899 (1987).
- (46) F.R. Eirich, "Science and Technology of Rubber", Academic press, 1978.
- (47) A.I. Medalia, *Rubber Chem. Technol.* **51**, 437, (1978).
- (48) A.B. Davey and A.R. Payne, "Rubber in Engineering Practice", Maclaren & Sons Ltd., 1965.
- (49) A.I. Medalia, *Rubber Chem. Technol.* **64**, 481, (1991).
- (50) A.R. Payne, *Rubber and Plastics age*, 963, August, (1961).
- (51) A.R. Payne and R.E. Whitetaker, *J. Appl. Polym. Sci.* **16**, 1191, (1972).
- (52) A.R. Payne, *J. Appl. Polym. Sci.* **7**, 873, (1963).
- (53) A.I. Medalia, *Rubber world* **168** (5), 49, (1973).
- (54) J.D. Ulmer, V.E. Chirico and C.E. Scott, *Rubber Chem. Technol.* **46**, 897, (1973).
- (55) A.I. Medalia, *Rubber Chem. Technol.* **46**, 877, (1973).
- (56) A.R. Payne, *J. Appl. Polym. Sci.* **6**, 57, (1962).
- (57) A.R. Payne, *Rubber Chem. Technol.* **36**, 432, (1963).
- (58) A. Einstein, *Ann. Physik* **19**, 289 (1906); *ibid.* **34**, 591 (1911).
- (59) H.M. Smallwood, *J. Appl. Phys.* **15**, 758, (1944).
- (60) E. Guth, *Rubber Chem. Technol.* **18**, 596, (1945).
- (61) A.I. Medalia, *Rubber Chem. Technol.* **45**, 1171, (1972).
- (62) J.M. Caruthers, R.E. Cohen and A.I. Medalia, *Rubber Chem. Technol.* **49**, 1076 (1976).
- (63) E.M. Dannenberg, *Ind. Eng. Chem.* **44**, 813, (1952).
- (64) B.B. Boonstra and A.I. Medalia, *Rubber age* **46**, 892, (1963).
- (65) B.B. Boonstra and A.I. Medalia, *Rubber Chem. Technol.* **36**, 115, (1963).
- (66) E.M. Dannenberg, *Rubber Chem. Technol.* **48**, 410, (1975).
- (67) D.A. Meyer and J.G. Sommer, *Rubber Chem. Technol.* **44**, 258, (1971).
- (68) M.J. Wang, S. Wolff and E.H. Tan, *Rubber Chem. Technol.* **66**, 178, (1993).
- (69) A.R. Payne, *Rubber J.* **146**, 36, (1964).

- (70) A.R. Payne and J.R. Scott, "Engineering Design with Rubber", Maclaren & Sons Ltd., 1960.
- (71) BS 903 : Part A 24 : "Method of testing vulcanised rubber" (1976).
- (72) E.A. Meinecke and M.I. Taftaf, Rubber Chem. Technol. **61**, 534, (1988).
- (73) E. Guth, J. Appl. Phys. **16**, 20 (1945).
- (74) L. Mullins and N.R. Tobin, Trans. Inst. Rubber Ind. **33**, 2 (1956)
- (75) E.A. Meinecke, Rubber Chem. Technol. **64**, 269, (1991).
- (76) G.R. Hamed, Rubber Chem. Technol. **67**, 529, (1994).
- (77) R. Selden, Prog. in Rubber and Plastics Technol. **11**, 56, (1995).
- (78) D.G. Young, Rubber Chem. Technol. **59**, 809, (1986)
- (79) D.G. Young, Rubber Chem. Technol. **63**, 567, (1990).
- (80) G.J. Lake and P.B. Lindley, J. Appl. Polym. Sci. **8**, 707, (1964).
- (81) H.W. Greensmith and A.G. Thomas, J. Appl. Polym. Sci. **18**, 189, (1955).
- (82) A.N. Gent, G.L. Liu and T. Sueyasu, Rubber Chem. Technol. **64**, 96, (1991).
- (83) A.N. Gent and M. Hindi, Rubber Chem. Technol. **61**, 892, (1988).
- (84) J.P. Holman, "Heat transfer", McGraw-Hill Book Co., Seventh Edition, 1992.
- (85) S.D. Gehman, Rubber Chem. Technol. **40**, 36, (1967).
- (86) K. Eiermann and K.H. Hellwege, Rubber Chem. Technol. **36**, 75, (1963).
- (87) I. William, Ind. Eng. Chem. **15**, 154, (1923).
- (88) C.E. Barnett, Ind. Eng. Chem. **26**, 303, (1934).
- (89) V.O. Fogel, V.A. Lepetov, and I.M. Agayants, Soviet Rubber Technol. **21** (5), 24, (1962).
- (90) L.C.K. Carwile and H.J. Hoge, Rubber Chem. Technol. **39**, 126, (1966).
- (91) L.R. Sperberg, L. Harrison and J.F. Svetlik, India Rubber World **122** (5), 536, (1950).
- (92) P. Kainradl, Gummi Asbest **5**, 44, (1952).
- (93) D. Kong, J.L. White, F.C. Weissert and N. Nakajima, Rubber Chem. Technol. **40**, 140, (1967).
- (94) A.K. Sircar and J.L. Wells, Rubber Chem. Technol. **55**, 191, (1982).

- (95) D.R. Macrac and R.I. Zapp, Rubber Age **82**, 831, (1958).
- (96) N. Bekkedahl and H. Matheson, Rubber Chem. Technol. **9**, 264, (1936).
- (97) H.K. Frensdorff, Rubber Chem. Technol. **47**, 849, (1974).
- (98) Beatty, Armstrong and Schoenborn, Ind. Eng. Chem. **42**, 1527, (1950).
- (99) S.H. Hahn, J. Appl. Phys. **12**, 12, (1941).
- (100) C. Cuthbert, Rubber Chem. Technol. **27**, 590, (1954).
- (101) A.G. Worthing, "Temperature ; Its Measurement and Control in Service and Industry", Reinhold Publishing Co., New York, 1941.
- (102) D.M. Turner and M. Brennen, Plas. and Rubb. Proc. and Appl., **14**, 183 (1990).
- (103) DISPLAY III User's manual, "Pre- & Post Processing Programme", EMRC, Michigan, USA.
- (104) NISA II User's manual, EMRC, Michigan, USA.
- (105) C.S. Desai and J.F. Abel, "Introduction to the Finite Element Method", Van Nostrand Reinhold Comp., 1972.
- (106) R.S. Rivlin, Tran. Roy. Soc. Lon., A **242**, No. 845, 173 (1949).
- (107) L.L. Erickson, Rubb. & Plas. News, 15 March 1993.
- (108) P.S. Oubridge, RuPEC Internal Report, "Determination of Rivlin Elastic Constants", IPTME, Loughborough University, 1996.
- (109) P. S. Oubridge, Visiting Senior Research Fellow, IPTME, Loughborough University.
- (110) K. Tsuge, R.J. Arenz, S.J. Landel and R.F. Landel, Rubber Chem. Technol. **51**, 948, (1978).
- (111) A.G. James and A. Green, J. Appl. Polym. Sci. **19**, 2319, (1975).
- (112) J.A. Harris, Rubber Chem. Technol. **60**, 870 (1987).
- (113) R.B. Ross, "Metallic Materials", Chapman and Hall Ltd., London, 1968.
- (114) EMRC (Engineering Mechanics Research Corporation), P.O. Box 696, Troy, Michigan, 48099, USA.
- (115) Metalastik Vibration Control System, Dunlop Ltd., Leicester, U.K.
- (116) R.H. Myers, "Response Surface Methodology", Wiley, New York, 1995.

- (117) "STATGRAPHICS", Manugistics Inc., 2115 East Jefferson Street, Rockville, Maryland 20852, USA.
- (118) V. John, "Introduction to Engineering Materials", Third Edition, Macmillan, Hong Kong, 1992.
- (119) W.M. Kays and M.E. Crawford, "Convection Heat and Mass Transfer", McGraw-Hill, New York, 1963.
- (120) A.I. Brown and S.M. Marco, "Introduction to Heat Transfer", Third Edition, McGraw-Hill, 1958.
- (121) M. Fishenden and O.A. Saunders, "An Introduction to Heat Transfer", Oxford University Press, London, 1950.





